

Adjusting design models for pile caps and wall girders by using non-linear Finite Element Analysis

Master Thesis

Thesis Committee:

Dr.ir. M.A.N. Hendriks
Prof.dr.ir. J.G. Rots
Mrs. dr.ir. E.O.L. Lantsoght
Paul van Noppen

TU Delft
TU Delft
TU Delft
IOB

Daan Bourgonje
TU Delft & ingenieursbureau IOB

Date: October 21st, 2020

Preface

This report is the result of the research that is performed from February 10th to October 21st in order to obtain my master's degree in Structural Engineering at Delft University of Technology. This report covers my interest regarding the design of reinforced concrete structures. The main focus of this research lies upon optimizing the reinforcement design of pile caps and wall girders by adopting strut-and-tie method verifications and models by making use of numerical analyses performed in DIANA. This research has been carried out in collaboration with Ingenieursbureau IOB.

I would like to thank the members of my committee Dr.ir. Hendriks, Prof.dr.ir. J.G. Rots, Mrs. dr.ir. E.O.L. Lantsoght and Paul van Noppen for guiding me through this research and for always standing by if I had questions. I would also like to thank Ingenieursbureau IOB for helping me in my research and providing me resources.

Daan Bourgonje
October, 2020

Abstract

The strut-and-tie method is a reliable tool for designing the reinforcement in discontinuity regions in reinforced concrete structures. It provides safe designs, but it is on the other hand also acknowledged to provide conservative designs. As the strut-and-tie model is widely used in the design of structural elements as wall girders and pile caps, it would be very beneficial if its verifications or the strut-and-tie model itself can be optimized.

The Eurocode provides verifications for the concrete nodes and struts and the reinforcement ties in a strut-and-tie model. The Eurocode also provides minimum amounts of web reinforcement for 'deep beams', that might overrule the design verification based on the actual stresses in a structural element. No restrictions regarding the dimensioning of the nodes are given and two methods for calculating the steel stress in a crack width calculation are given in the Eurocode. In this research it is aimed at to gain more clarity in the application of the strut-and-tie method and to optimize the verifications.

The strut-and-tie model and its Eurocode verifications are introduced as well as the choices for modelling the reinforced concrete in DIANA. A verification of the constitutive models that are used in the analyses of this research is made by making use of experiments found in literature.

To check the verifications and see if any optimizations are possible, six pile cap models, four simply supported and two 2-span wall girders are analyzed numerically in DIANA and compared to an analytical calculation with the strut-and-tie model (by making use of Eurocode verifications). Variation studies are made with the purpose to study the influence of the web reinforcement in the pile caps, the span to depth ratio and the application of additional reinforcement above the supports of a wall girder.

For the pile caps a few clarifications are concluded, of which one also contributes in reducing the reinforcement. It becomes clear that the steel stress that is needed for the crack width verification should be calculated using the strut-and-tie model, instead of using an elastic approach with a lever arm that is provided in the Eurocode. This will reduce the steel stress up to 30 % for the models that are analyzed in this report, depending on the span to depth ratio.

Research is done on the influence of web reinforcement. Applying web reinforcement that is based on the force in the strut, neglecting the minimum amount that is applicable for deep beams, decreases the capacity only up to 2.6 % for the models in this research that fail due to diagonal splitting. However, the diagonal cracks that need to be prevented by this web reinforcement are large and therefore further experimental research should reveal if this minimum amount is actually necessary.

The CCC- nodes in the pile cap should not be dimensioned by assuming a hydrostatic node (node with equal stresses on each surface), instead a node dimension that is based on the effective depth should be used (resulting in non-hydrostatic nodes).

For the continuous wall girder, a suitable strut-and-tie model is found that reduces the amount of longitudinal reinforcement (from 0.52 % to 0.115%) and increases the ductility compared to a strut-and-tie model that was found in literature and used initially.

In this research more insight is gained in the design procedure when using the strut-and-tie method. All verifications from the Eurocode for the strut-and-tie method are considered and compared to optimize the design in the considered structural elements.

Table of Contents

Preface	iii
Abstract	v
List of Figures	ix
List of Tables	xii
List of Symbols	xiii
1 Introduction	1
1.1 General overview	1
1.2 Scope of the research	2
1.3 Aim of the research	3
1.4 Research questions	3
1.5 Strategy	3
1.6 Outline of the report	4
2 Literature review	5
2.1 Strut and tie model	5
2.1.1 Principle of the strut-and-tie method	5
2.1.2 Setting up a strut-and-tie model	6
2.1.3 Strut-and-tie elements	8
2.1.4 Remaining challenges for strut and tie models	11
2.1.5 Remaining design verifications by the Eurocode	12
2.2 Finite element method	17
2.2.1 Principle of the finite element method	17
2.2.2 Non-Linear FEA of Reinforced Concrete structures	18
2.2.3 Safety formats	24
2.3 Previous Research	27
2.3.1 Previous experiments on pile caps	27
2.3.2 Previous experiments on wall girders	29
2.3.3 Application of 2D NLFEA in previous studies	33
2.3.4 Previous researches on strut-and-tie modelling of continuous wall girders	34
2.4 Conclusion	35
3 Specifications and verification of the FE model	37
3.1 Specifications of the FE model	37
3.2 Experimental research performed by Subedi et al.	39
3.2.1 Description of the experiment	39
3.2.2 Nonlinear finite element model	42
3.3 Experimental research performed by Zhang et al.	44
3.3.1 Description of the experiment	44

3.3.2	Nonlinear finite element model	46
3.4	<i>Comparison of results</i>	48
3.4.1	Failure mode comparison	48
3.4.2	Comparison of failure- and cracking loads	55
3.4.3	Load-deflection curve and Load-strain curve comparison	56
3.5	<i>Conclusion</i>	58
4	Pile cap analyses	59
4.1	<i>General overview</i>	59
4.2	<i>Strut-and-tie model</i>	61
4.2.1	Model A (strut angle of 45°)	61
4.2.2	Model B (strut angle of 60°)	63
4.2.3	Model C (strut angle of 65°)	64
4.3	<i>Finite element models and results</i>	66
4.4	<i>Conclusion</i>	72
5	Wall girder analyses	73
5.1	<i>General overview</i>	73
5.2	<i>Strut-and-tie-model wall girder</i>	74
5.2.1	Simply supported	74
5.2.2	Continuous wall girder on three supports	76
5.3	<i>Finite element models and results</i>	78
5.4	<i>Conclusion</i>	82
6	Discussion of results	83
6.1	<i>Dimensions of the nodes</i>	83
6.1.1	CCT nodes	83
6.1.2	CCC node pile cap	86
6.2	<i>Web reinforcement of the pile caps</i>	88
6.3	<i>Crack width control</i>	90
6.4	<i>Reinforcement above the supports of a wall girder</i>	93
6.5	<i>Strut-and-tie model continuous wall girder</i>	95
7	Conclusions and recommendations	99
7.1	<i>Conclusions</i>	99
7.2	<i>Recommendations</i>	101
7.2.1	Adding an experimental research to the numerical research on the diagonal cracking behaviour of reinforced concrete pile caps.	101
7.2.2	Further research on the behaviour of reinforced concrete wall girders or deep beams on three supports	101
	References	102
	Appendix A1: Excel sheet of Eurocode calculation pile cap model A	104
	Appendix A2: Excel sheet of Eurocode calculation pile cap model B	105

Appendix A3: Excel sheet of Eurocode calculation pile cap model C	106
Appendix A4: Excel sheet of Eurocode calculation wall girder model D	107
Appendix A5: Excel sheet of Eurocode calculation wall girder model E.....	108
Appendix A6: Excel sheet of Eurocode calculation model F	109
Appendix B: DIANA plots pile cap models	110
Appendix C: DIANA plots wall girder models.....	113
Appendix D: Continuous wall girder calculation using new strut-and-tie model	116

List of Figures

Figure 1.2.1: Pile cap with two piles	2
Figure 1.2.2: wall girder [11]	2
Figure 2.1.1: D-regions in a beam.....	5
Figure 2.1.2: Load path method [18]	7
Figure 2.1.3: Elastic stress trajectories [18].....	7
Figure 2.1.4: diagonal compressive struts.....	8
Figure 2.1.5: Tensile stresses perpendicular to the struts	8
Figure 2.1.6: Partially- and fully disturbed strut [13]	8
Figure 2.1.7: transverse compressive stress [13]	9
Figure 2.1.8: transverse tensile stress [13].....	9
Figure 2.1.9: C-C-C node.....	10
Figure 2.1.10: C-C-T node	10
Figure 2.1.11: CCT node [13]	13
Figure 2.1.12: effective tension area in a beam cross section [13]	14
Figure 2.2.1: solution scheme of the finite element method.....	17
Figure 2.2.2: equilibrium equations	18
Figure 2.2.3: Concrete loaded in compression and tension	19
Figure 2.2.4: Cracking models with linear softening	20
Figure 2.2.5: Exponential softening [10]	20
Figure 2.2.6: Hordijk softening [10].....	20
Figure 2.2.7: Tension stiffening effect.....	21
Figure 2.2.8: Bonding of ribbed reinforcing bars in concrete.....	22
Figure 2.2.9: Concrete loaded in compression	23
Figure 2.2.10: elasto-plastic approach [10]	23
Figure 2.2.11: Nonlinear bf of the reinforcing bars [10].....	24
Figure 2.2.12: Calculated capacity vs experimentally obtained capacity [10].....	26
Figure 2.3.1: Reinforcement design in two-pile cap for proposed design procedure [2].....	28
Figure 2.3.2: Reinforcement design in two-pile cap based on ACI Building Code [2]	28
Figure 2.3.3: strut in a wall girder [11]	30
Figure 2.3.4: Failure modes of a wall girder [20].....	31
Figure 2.3.5: Strut and tie model of a continuous deep beam [24]	32
Figure 2.3.6: Strut-and-tie model of continuous wall girder [19].....	34
Figure 3.2.1: Beam 1B1 [20]	40
Figure 3.2.2: Beam 1B2 [20]	40
Figure 3.2.3: Beam 1A1 [20]	41
Figure 3.2.4: Load-strain curve for beam 1B2 [20].....	41
Figure 3.2.5: Constitutive model for 6 mm diameter reinforcement bars.....	42
Figure 3.2.6: Geometry of beam 1B1	43
Figure 3.2.7: Geometry of beam 1B2	43
Figure 3.2.8: Geometry of beam 1A1	43
Figure 3.3.1: Beam MDB-2 [24]	45
Figure 3.3.2: Beam MDB-3 [24]	45
Figure 3.3.3: Beam MDB-4 [24]	45
Figure 3.3.4: Geometry of beams MDB-2 and MDB-3.....	47
Figure 3.3.5: Geometry of beam MDB-4	47
Figure 3.4.1: Numerical results (a, b) and experimental results (c) of the failure mode for beam 1B1 (rupture strain = 2.77×10^{-2}).....	49
Figure 3.4.2: Numerical results (a, b) and experimental results (c) of the failure mode for beam 1B2	50
Figure 3.4.3: Numerical results (a, b) and experimental results (c) of the failure mode for beam 1A1 (rupture strain = 2.77×10^{-2}).....	51
Figure 3.4.4: Numerical results (a, b) and experimental results (c) of the failure mode for beam MDB-2	52

Figure 3.4.5: Numerical results (a, b) and experimental results (c) of the failure mode for beam MDB-3	53
Figure 3.4.6: Numerical results (a, b) and experimental results (c) of the failure mode for beam MDB-4	54
Figure 3.4.7: L-S curve (a) and L-D curve (b) of beam MDB-2	57
Figure 3.4.8: L-S curve (a) and L-D curve (b) of beam MDB-3	57
Figure 3.4.9: L-S curve (a) and L-D curve (b) of beam MDB-4	57
Figure 3.4.10: L-S curve of beam 1B2	58
Figure 4.2.1: Strut-and-tie model of pile cap model A	62
Figure 4.2.2: Reinforcement layout model A	62
Figure 4.2.3: Strut-and-tie model of pile cap model B	63
Figure 4.2.4: Reinforcement layout model B	64
Figure 4.2.5: Strut-and-tie model of pile cap model C	65
Figure 4.2.6: Reinforcement layout model C	65
Figure 4.3.1: constitutive relation of the reinforcement bars	66
Figure 4.3.2: Finite element model for Pile cap model A1	68
Figure 4.3.3: Finite element model for Pile cap model A2	68
Figure 4.3.4: Finite element model for Pile cap model B1	68
Figure 4.3.5: Finite element model for Pile cap model B2	68
Figure 4.3.6: Finite element model for Pile cap model C1	68
Figure 4.3.7: Finite element model for Pile cap model C2	68
Figure 4.3.8: Load deflection curve of model A1 an A2	69
Figure 4.3.9: Load deflection curve of model B1 and B2	69
Figure 4.3.10: Load deflection curve of model C1 and C2	69
Figure 4.3.11: Crack pattern at failure load for pile cap model A1 (a), A2 (b), B1 (c) and C1 (d)	71
Figure 4.3.12: Concrete compressive stresses at final load step before failure for pile cap model A1 (a), B1 (b) and C1 (c)	71
Figure 5.2.1: General strut and tie model for the simply supported wall girder	75
Figure 5.2.2: Reinforcement design of wall girder D	76
Figure 5.2.3: Reinforcement design of wall girder E	76
Figure 5.2.4: Strut-and-tie model for continuous wall girders	76
Figure 5.2.5: Reinforcement design of wall girder F1	77
Figure 5.2.6: Reinforcement design of wall girder F1	77
Figure 5.3.1: Reinforcement detail model D2	78
Figure 5.3.2: Reinforcement detail model E2	78
Figure 5.3.3: Finite element model for wall girder model D1	79
Figure 5.3.4: Finite element model for wall girder model D2	79
Figure 5.3.5: Finite element model for wall girder model E1	79
Figure 5.3.6: Finite element model for wall girder model E2	79
Figure 5.3.7: Finite element model for wall girder model F1	79
Figure 5.3.8: Finite element model for wall girder model F2	79
Figure 5.3.9: Load deflection curve of model D1 and D2	80
Figure 5.3.10: Load deflection curve of model E1 and E2	80
Figure 5.3.11: Load deflection curve of model F1 an F2	80
Figure 5.3.12: Crack pattern at final load step before failure for wall girder model D1 (a), E1 (b) and F1 (c)	82
Figure 5.3.13: Concrete compressive stresses at final load step before failure for wall girder model D1 (a), E1 (b) and F1 (c)	82
Figure 6.1.1: CCT node [13]	83
Figure 6.1.2: Numerical and Analytical (strut-and-tie model) compressive stresses along node (in between point A and B) in pile cap model A1	84
Figure 6.1.3: Numerical and Analytical (strut-and-tie model) compressive stresses along node (in between point A and B) in pile cap model C2	84
Figure 6.1.4: Numerical and Analytical (strut-and-tie model) compressive stresses along node (in between point A and B) in wall girder model D1	85

Figure 6.1.5: Numerical and Analytical (strut-and-tie model) compressive stresses along node (in between point A and B) in wall girder model E1	85
Figure 6.1.6: Compressive stresses at main reinforcement level for pile cap model A1.....	85
Figure 6.1.7: Compressive stresses at main reinforcement level for pile cap model C2.....	85
Figure 6.1.8: Compressive stresses along vertical node surface (x') in pile cap model A1.....	87
Figure 6.1.9: Compressive stresses along vertical node surface (x') in pile cap model B1.....	87
Figure 6.1.10: Compressive stresses along vertical node surface (x') in pile cap model C2.....	87
Figure 6.2.1: Largest web reinforcement strain vs Load for pile cap models A.....	89
Figure 6.2.2: Largest web reinforcement strain vs Load for pile cap models B.....	89
Figure 6.2.3: Largest web reinforcement strain vs Load for pile cap models C.....	89
Figure 6.2.4: Flexural shear crack of model A1 (a) and Diagonal splitting crack of model B1 (b)	89
Figure 6.3.1: Longitudinal reinforcement strain at midspan for pile cap models B1 and B2 (ultimate strain = 2750×10^{-6})	91
Figure 6.3.2: Longitudinal reinforcement strain at midspan for pile cap models C1 and C2 (ultimate strain = 2750×10^{-6})	91
Figure 6.3.3: Load-strain curve of test specimen MDB-3 (chapter 3.4).....	92
Figure 6.3.4: Horizontal Stresses over the height at midspan for model A1.....	92
Figure 6.3.5: Horizontal Stresses over the height at midspan for model B1.....	92
Figure 6.3.6: Horizontal Stresses over the height at midspan for model C1.....	92
Figure 6.4.1: Crack pattern at final load step before failure for model D1	93
Figure 6.4.2: Crack pattern at final load step before failure for model E1.....	93
Figure 6.4.3: Reinforcement stresses above the support of model D1.....	94
Figure 6.4.4: Reinforcement stresses above the support of model D2.....	94
Figure 6.4.5: Reinforcement stresses above the support of model E1	94
Figure 6.4.6: Reinforcement stresses above the support of model E2	94
Figure 6.5.1: Distribution of the support reactions	95
Figure 6.5.2: Longitudinal reinforcement strain of model F1 and F2 (yield strain = 2392.5×10^{-6}).....	96
Figure 6.5.3: Concrete compressive stresses (S2) at last load step before failure for wall model F1	96
Figure 6.5.4: Alternative strut-and-tie model continuous wall	97
Figure 6.5.5: Ratio between intermediate and outer support reaction.....	97
Figure 6.5.6: Load-Deflection curve of the new model and model F1	98
Figure 6.5.7: Load-Strain curve of the new model and model F1	98
Figure 7.1.1: Geometry of pile cap model A1 (Model A2 contains less web reinforcement)	99
Figure 7.1.2: Geometry and reinforcement of half of wall girder model D1 (For model D2 additional reinforcement is applied above the supports)	99
Figure 7.1.3: Geometry and reinforcement of half of wall girder model F1 (Model F2 contains no upper tensile tie, this reinforcement is spread out over the web reinforcement)	99

List of Tables

Table 3.1.1: Finite elements and constitutive relations of concrete	37
Table 3.1.2: Finite element and constitutive relations of reinforcement.....	38
Table 3.1.3: material properties of concrete [10]	38
Table 3.2.1: concrete properties of beam 1B1, 1B2 and 1A1	40
Table 3.2.2: Reinforcement properties [20]	40
Table 3.2.3: Input parameters for the constitutive model of concrete for all three beams tested by Subedi et al.	42
Table 3.3.1: concrete properties [24]	44
Table 3.3.2: Reinforcing steel properties [24]	44
Table 3.3.3: Input parameters for the constitutive model of concrete of the beams tested by Zhang et al.	46
Table 3.4.1: Comparison of the failure loads.....	55
Table 3.4.2: Comparison of cracking loads	55
Table 4.1.1: specifications of the pile caps used for the strut-and-tie model analyses.....	60
Table 4.1.2: Specifications of the pile caps used for the NLFEA	60
Table 4.3.1: concrete properties for the Global Resistance Factor	66
Table 4.3.2: Reinforcement properties for the Global Resistance Factor ($A = f_{tm}/f_{ym}$).....	66
Table 4.3.3: Reinforcement properties.....	67
Table 4.3.4: input variables for the constitutive model of concrete in DIANA.....	67
Table 4.3.5: Numerical results of pile cap models.....	70
Table 5.1.1: specifications of the wall girders used for the strut-and-tie model analyses	73
Table 5.1.2: specifications of the wall girders used for the numerical analyses	73
Table 5.2.1: Reinforcement design of model D	75
Table 5.2.2: Reinforcement design of model E.....	75
Table 5.2.3: Reinforcement design of model F1.....	77
Table 5.2.4: Reinforcement design of model F2.....	78
Table 5.3.1: Numerical Failure Loads of wall girder models.....	81
Table 6.1.1: Node heights for CCC nodes of pile caps	86
Table 6.2.1: Diagonal cracking loads for pile cap models (*Flexural shear cracks, see Figure 6.2.4)	88
Table 6.3.1: Reinforcement strains and stresses at midspan for pile cap models B and C (at SLS Load)	91
Table 6.3.2: SLS Steel stress using strut-and-tie model	91
Table 6.4.1: Difference in support capacity between model E1 and E2 and between model D1 and D2	94
Table 6.5.1: Ratio between intermediate and outer support reaction	97

List of Symbols

$A_{c,eff}$	Effective area of concrete in tension
A_s	Amount of reinforcement steel
b	Width
c	Cover on reinforcement
d	effective depth
E_c	Young's Modulus concrete
E_s	Young's Modulus steel
f_{cd}	Design cube concrete compressive strength
f_{ck}	Characteristic cube concrete compressive strength
f_{cm}	Mean concrete compressive strength
f_{ctd}	Design concrete tensile strength
f_{ctm}	Mean concrete tensile strength
f_u	Ultimate strength of the reinforcement
f_{yd}	Yield strength of the reinforcement
G_F	Concrete fracture energy
h	Depth
$h_{c,eff}$	Effective height of concrete in tension
l	span
n	number of reinforcement bars
R_d	Design capacity
s	spacing between the reinforcement bars
$s_{r,max}$	maximum value of the crack spacing
w	crack width
z	Internal lever arm
α_E	$\frac{E_s}{E_c}$
ε_{cm}	mean concrete strain in between cracks
ε_{sm}	mean reinforcement strain
ε_u	Ultimate reinforcement strain
ρ	Reinforcement ratio
$\rho_{p,eff}$	Effective reinforcement ratio
σ	stress
\emptyset	Reinforcement bar diameter

1 Introduction

1.1 General overview

One of the most reliable methods to design discontinuity regions (D-regions) in reinforced concrete is the strut-and-tie model. These discontinuity regions can be caused by discontinuity in geometry (changing dimensions of the cross section) or discontinuity in loading (concentrated loads or supports). The flow of internal forces in a structure is modelled as a truss, consisting of members in tension (ties) and members in compression (struts) to transfer the imposed loads to the supports. Based on this truss a design for the reinforcement can be made. As concrete has a low resistance in tension, reinforcement is necessary at the positions in the structure where the ties are modelled.

The method is based on the lower-bound theorem of plasticity. Different studies indicated that the truss model can be quite conservative, this is stated in a master thesis performed by Alfrink in 2015 [5]. The actual stress distribution in a wall girder can deviate significantly from the model that is assumed in the calculations as it is just a simplification of reality. The strut-and-tie model uses 2D elements that are used on 3D structures, some capacity may be neglected due to this. As the strut-and-tie method is a widely used calculation method, it is important to check the process and the verifications for this calculation method. It would therefore also be very beneficial if these verifications or the model itself can be optimized.

This research focusses on the reinforcement design of pile caps and wall girders. The strut and tie model can be quite time-consuming for structures with complex geometry. However, pile caps and wall girders are simple structural elements to model using the strut and tie method. No discontinuity in geometry is observed but the D-region is present due to the applied load and the supports. Pile caps and wall girders are structural elements with a large depth over width ratio (h/b). Following Saint Venant principle, the extent of the D-region is equal to the depth of the beam. In the case of a wall girder or pile cap this means that the whole wall girder or pile cap can be seen as a D-region and no linear stress state will be observed in these structures. The strut-and-tie model becomes however more complex for continuous wall girders.

The Eurocode states that the reinforcement of the pile caps should be designed using the strut and tie method. The Eurocode provides the verifications for the struts, ties and nodes that will follow from using the strut and tie model.

Another option for verifying a design of the reinforcement in the considered structural elements, is by using the finite element method. By making a finite element analysis, the stress distribution in the structural element can be obtained. Based on these obtained stresses in the structure, the reinforcement can be verified/designed. As reinforced concrete shows non-linear behaviour, it is most convenient to perform a nonlinear finite element analysis. Finite element analysis refers to a nonlinear finite element analysis in this report, as the analyses performed in this report are all nonlinear.

Drawback to performing a nonlinear finite element analysis for designing the reinforcement is that it requires a lot of detailed knowledge about how to model the reinforced concrete and that it can be hard to interpret the results. The strut and tie model is, in contrary to the finite element analysis, a straight-forward method to design the pile-cap or wall girder and provides safe solutions.

This report provides the research on optimizing the mentioned structures following the strut and tie model and verifications of the Eurocode by comparing this to a nonlinear finite element model.

1.2 Scope of the research

The principle of this research is a comparison between the finite element model and the Eurocode verifications using a strut and tie model. The finite element analysis will be done using DIANA. Two structural elements will be analysed:

1. Pile caps with two piles
2. Wall girder (Simply supported and wall girder on three supports)

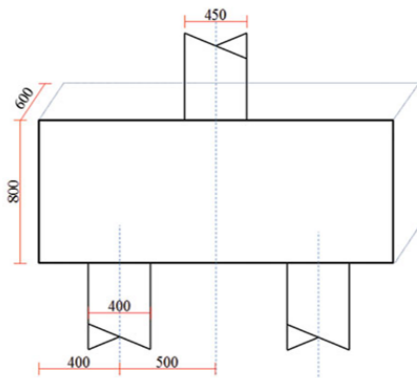


Figure 1.2.1: Pile cap with two piles

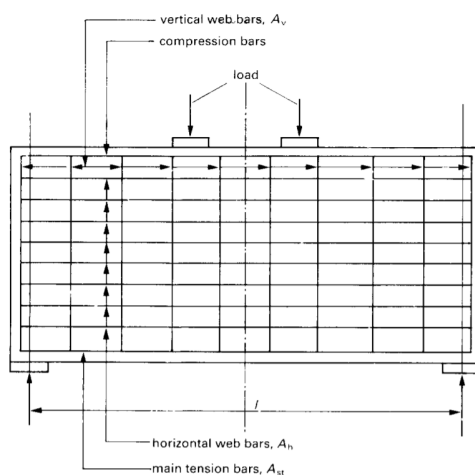


Figure 1.2.2: wall girder [11]

Figures of the structural elements are just for illustration. The dimensions of the structural elements that are specified in the Figures are not in accordance with the dimensions that will be used in this report.

1.3 Aim of the research

The main goal of this research is to optimize the required reinforcement in a pile cap and wall girder. The required reinforcement is currently designed by using a strut and tie model and by verifying this using Eurocode verifications. By using a nonlinear finite element analysis, it will be attempted to optimize these design verifications, e.g. reduce the amount of reinforcement that is needed.

Secondary goal in this research is to gain insight in how nonlinear finite element analyses can be used for the dimensioning of reinforcement in concrete structural elements. Distinction should be made between which results can and which results cannot be used in optimizing the reinforcement in a structural element.

Another goal is to create a calculation sheet for the structural elements that can be used in practice to design the reinforcement. This calculation sheet will obviously be based on the optimizations that may be found by reaching the main goal of this research.

1.4 Research questions

In order to achieve the goals of 1.3, the following research questions are formulated.

Main research question:

- How can the design of reinforcement in wall girders and pile caps following the ST model be optimized by making use of the insight gained through a NLFEA?

Supporting research questions:

- Which assumptions are made in the design process following the Eurocode and using the strut and tie method?
- How can reinforced concrete be modelled accurately in a nonlinear finite element program for these particular structures?
- What are the differences between the results of the nonlinear finite element analysis and the ST calculation?
- How can these differences between the results be explained and used to optimize the design verifications of the considered structures?

1.5 Strategy

To be able to answer the research questions, the following strategy is used:

- First a literature study is carried out to be able to make both analyses, be able to compare them and to be able to interpret and verify the results.
- Secondly, the nonlinear finite element model is verified. This done by modelling experiments found in literature and comparing the results.
- After this, the analyses are carried out for all structural elements, using both the strut and tie model and a non-linear finite element analysis. A variation in parameters is used to study their influence.
- The results are discussed, explanations are given for the obtained differences in results. Based on the results conclusions will be made and adjustments in the verification process will be recommended and implemented in calculation sheets.

1.6 Outline of the report

In chapter 2 a literature study is performed. The literature review is divided in 5 parts. A study on how the strut-and-tie-model works, which assumptions are made in the process and the Eurocode verifications that are used for it is performed in chapter 2.1.

A study on the finite element method and how reinforced concrete can be modelled is performed in chapter 2.2. The principle of the method is analysed, and the use of safety formats is discussed in this chapter. The nonlinear properties of concrete and the reinforcement are analysed.

A study on experimental researches on the regarding structural elements is performed in chapter 2.3. By studying these experimental researches found in literature, insight on the failure modes and the influence of certain parameters is gained. In this chapter also previous researches that made use of nonlinear finite element analyses are analysed.

In chapter 3 the finite element model specifications that will be used for the analyses are specified. To verify the constitutive model, analyses will be made on structural elements that were found in literature (and were discussed in chapter 2.5).

Chapter 4 and 5 contain the calculations for the pile caps and wall girders respectively, both the finite element calculation and the strut-and-tie model calculation will be presented in these chapters. Specifications and differences between the multiple models are indicated in this chapter. The results of the calculations are also discussed here.

The results of the analyses (both strut-and-tie model and NLFEA) are compared to each other in chapter 6. It is therefore important to have a good understanding of the results from the finite element software. By comparing these results, the differences are analysed and the source of these differences are analysed to justify if the differences can be used in adjusting the current verifications.

After the results of the analyses are analysed, there is concluded if adjustments can be made in the design verifications. These conclusions and recommendations can be found in chapter 7.

Calculation sheets of the analysed structural elements can be found in the appendices. In Appendix A1 up to and including Appendix A6, the calculation sheets for all models are presented. These sheets are used in the analyses in this report.

In Appendix B, DIANA results are presented for all pile cap models. This contains the principal compressive stresses, crack width and reinforcement strain plots at the last load step before failure. The same is presented for the wall girder models in Appendix C.

In Appendix D, the calculation sheet for the continuous model using an alternative strut-and-tie model is presented. The reinforcement design that follows from this calculation is also presented here.

2 Literature review

2.1 Strut and tie model

The strut and tie method originated from the truss analogy for shear design in B-regions. This was presented by Ritter in 1899 [16] and Mörsch in 1908 [12]. At a B-region, linear strain distribution is assumed. The truss analogy was using a parallel chords truss to idealize the flow of forces in a cracked concrete beam.

Later, a generalization of the truss analogy was proposed for application on any structural concrete part in the form of strut and tie models. This was proposed by Schlaich, Schläfer and Jennewein in 1987 [18]. Before this generalization, discontinuity regions in concrete were designed based on test results, past experience or rules of thumb.

The strut and tie model is widely used for designing reinforcement near concentrated loads or supports, near corners, near bends and for structures with openings.

2.1.1 Principle of the strut-and-tie method

When designing the required reinforcement in a simple beam subjected to a distributed load, the beam theory is used. This beam theory assumes a linear strain distribution over the cross-section. Regions with linear strain distribution over the cross-section are called B-regions (Bernoulli-region). This assumption is however not valid for a D-region, this is a discontinuity region. No linear strain distribution is observed in cross-sections in a D-region. A D-region can be present in a structure due to changes in the cross-section or openings in the cross-section. Another possible cause of a D-region is the presence of a concentrated load or a support reaction. The extent of the D-region is, following Saint Venant principle, equal to the width of the column (or depth in case of a beam) from the point of the discontinuity. This is shown in Figure 2.1.1.

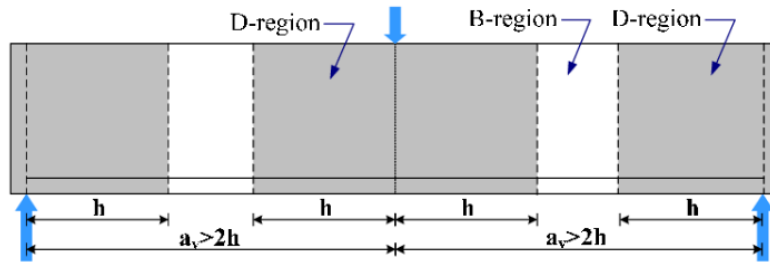


Figure 2.1.1: D-regions in a beam

This research focusses on the reinforcement design of pile caps and wall girders near the supports. No discontinuity in geometry is observed in this research (no discontinuities in the cross sections), but the D-region is present due to the applied load and the supports. Pile caps and wall girders are structural elements with a large depth over length ratio (h/l). Following Saint Venant principle, the extent of the D-region is equal to the depth of the beam. In the case of a wall girder or pile cap this means that the entire wall girder or pile cap can be seen as a D-region and no linear stress state will be observed in these structures.

The Eurocode states that for designing pile caps, the strut and tie model should be used. The strut-and-tie model is an effective method to model the stress flow in D-regions using a (imaginary) truss to distribute the load(s) to the support(s). The truss consists of members loaded in compression and members loaded in tension. The members loaded in compression represent the concrete compression struts, the members in tension represent the tensile ties (which represent one or multiple layers of reinforcement). The members intersect at nodal joints of which the resistance needs to be checked.

As stated earlier in this report, the strut-and-tie model is based on the lower bound theorem of plasticity. Concrete permits limited plastic deformations, the internal truss needs to be chosen such that the deformation capacity at any point is not exceeded before reaching the assumed state of stress in the rest of the structure. This ductility requirement is satisfied by adapting the struts and ties to the direction and size of internal forces as they would appear from the theory of elasticity. By using the theory of elasticity, some ultimate load is neglected which could be utilised by applying theory of plasticity.

Because it is a lower bound solution, it meets both the yield condition of the plastic theorem and the equilibrium condition, it does however not consider mechanism conditions (plastic hinges). From this it follows that the strut-and-tie model gives a solution that is lower or equal than the failure load and that the following conditions should be satisfied when setting up a strut and tie model:

- All nodes are in equilibrium, also the support reactions are in equilibrium with the applied load.
- The design forces that are present in the members and the nodes are lower than the design strength of the considered member.
- Only uniaxial forces in the struts and ties
- Struts cannot overlap
- No tensile strength in the concrete is assumed
- External forces are applied at nodes

Yielding of the tie should occur before failure of a strut or nodal zone. This is because the failure should be ductile.

2.1.2 Setting up a strut-and-tie model

First step in the verification of a structure using the strut-and-tie method, is obviously to set up the truss for the strut-and-tie model. An internal truss needs to be selected that can distribute the applied loads to the supports. This truss needs to satisfy the conditions mentioned before.

Numerous truss variations are possible to distribute the load to the supports. The loads in a structure try to use a path that has the least forces and deformations. It should be considered that the reinforcement bars are more deformable than the concrete struts. It can therefore be concluded that the model with the least number of ties is the best (as long as all conditions are satisfied). In designing a strut-and-tie model, minimizing the number of ties also delivers the most cost optimized solution as this results in the least amount of reinforcement.

Choosing the best suitable truss for using the strut-and-tie method on a structure can be quite hard and requires some understanding. For the structures considered in this report however, the best suitable model is quite straight-forward.

There are three methods available for setting up the truss:

1. Load path method
2. Elastic stress trajectories
3. Standard models

Load path method

For setting up a new strut-and-tie model, the load path method can be used. For the load path method, the flow of forces through which the applied load distributes to the supports is simulated. This load path is then sketched smoothly over the structure, this is shown in Figure 2.1.2(b). The corresponding strut and tie model can be constructed by replacing the curved load paths by polygons and adding further struts and/or ties to satisfy equilibrium in all nodes. This is shown in Figure 2.1.2(c). This technique is suggested by Schlaich and Schäfer in 1991 [17].

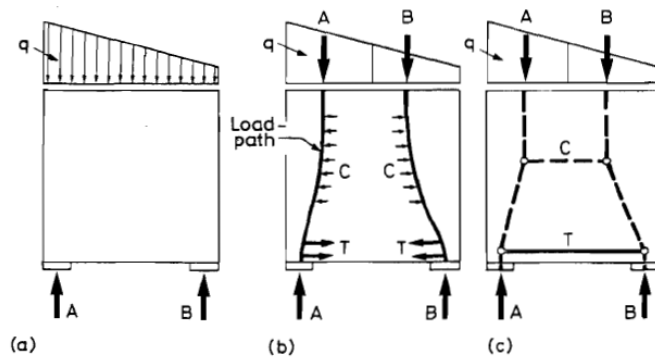


Figure 2.1.2: Load path method [18]

Elastic stress trajectories

This method is actually a version of the load path method. In this case the elastic stresses and principal stress trajectories within the D-region are analysed by an elastic finite element analysis. By using the principal stress trajectories, the process of setting up the truss gets simplified, as now the location and direction of the struts and ties can be determined immediately. This method is shown in Figure 2.1.3. The struts and ties are located in accordance with the main direction of the principle stresses.

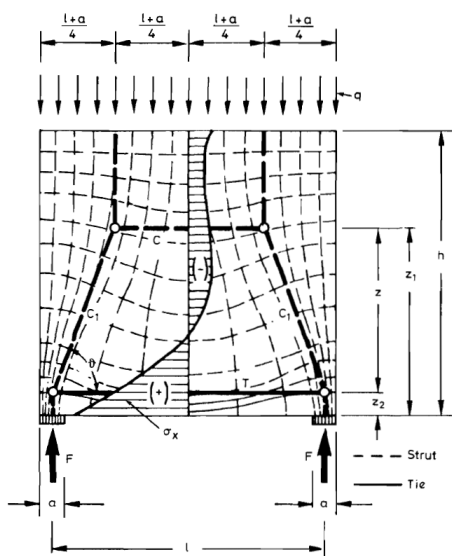


Figure 2.1.3: Elastic stress trajectories [18]

Standard models

Instead of fully composing a new strut and tie model, strut and tie models that appear more often can be used. These standard models can easily be adjusted, or models can be combined to create a model that is suitable for a particular structure. There are limited numbers of D-regions of which the stress patterns significantly differ, this makes it possible to design a structure using standard models.

2.1.3 Strut-and-tie elements

Struts

Struts represent the compressive stress fields within the structure. For a simply supported beam loaded by a concentrated load at midspan, the struts are located at the diagonals between the load and the supports, this is shown in Figure 2.1.4. The centreline of a strut is oriented along the principal compressive stress trajectory in the uncracked stage. The shape around this centreline can be prismatic or bottle-shaped, as shown in the Figure. The bearing area does not change for the prismatic shape, the strut remains parallel over its full length between two nodes. The bottle-shaped strut has a varying thickness along its length, the stresses are allowed to spread in the section. A consequence of the spreading of compression stresses is that tensile stresses will be generated perpendicular to the strut. This is shown in Figure 2.1.5. This effect can result in splitting cracks and if transverse reinforcement is not provided sufficiently, the strut may fail due to this splitting effect.

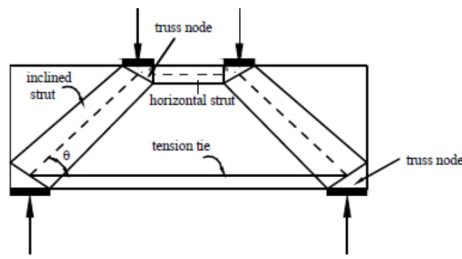


Figure 2.1.4: diagonal compressive struts.

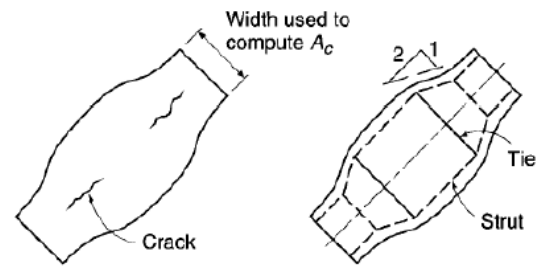


Figure 2.1.5: Tensile stresses perpendicular to the struts

The Eurocode provides a formula that can be used to estimate the transverse tensile stresses in a bottle-shaped strut. The Eurocode provides two expressions for the transverse tensile stress, one for a partially disturbed strut and one for a fully disturbed strut. When the width of the strut is equal to or less than half of its height ($b \leq \frac{H}{2}$), the strut can be considered as partially disturbed and a B-region can occur in the strut. For a fully disturbed strut ($b > \frac{H}{2}$) the entire section in the strut is a D-region. This is shown in Figure 2.1.6. The partially disturbed strut is shown left and the fully disturbed strut is shown at the right side in the Figure.

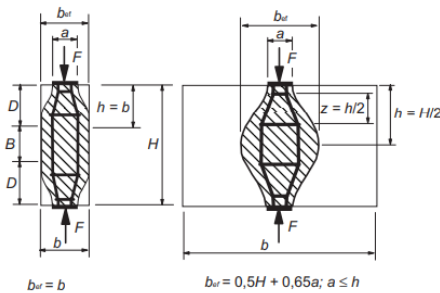


Figure 2.1.6: Partially- and fully disturbed strut [13]

The transverse tensile force can now be calculated following NEN-EN 1992-1-1:2005 [13] formula 6.58 and 6.59 as:

$$T = \frac{1}{4} \frac{b-a}{b} F \quad \text{For partially disturbed struts} \quad (2.1)$$

$$T = \frac{1}{4} \left(1 - 0.7 \frac{a}{h}\right) F \quad \text{For fully disturbed struts} \quad (2.2)$$

Based on these transverse tensile forces, the required orthogonal reinforcement can be determined. The Eurocode states that deep beams should be provided with an orthogonal reinforcement mesh near each face. There are minimum values given in NEN-EN 1992-1-1:2005 [13]:

$$A_{s,dbmin} = 0.1\% \geq \frac{150mm^2}{m} \quad \text{per face per direction}$$

It needs to be checked if this minimum value suffices by calculating the transverse tensile forces that result from the strut (equations above).

Obviously, the strut also needs to be checked for the compression stress that is present in it. The design value of the compressive strength of the struts is depending on what the stress condition in transverse direction is. When no transverse stresses or compressive stresses in transverse directions are present (see Figure 2.1.7), the design value of the concrete compressive strength can be used. The Eurocode states that 'It may be appropriate to assume a higher design strength in regions where multi-axial compression exists'. However, no value for this increase in strength is specified in the Eurocode.

When transverse tensile stresses are present (see Figure 2.1.8), the compressive strength of the concrete strut should be reduced following formula 2.3 that is found in NEN-EN 1992-1-1:2005 [13] formula 6.56.

$$\sigma_{Rd,max} = 0.6 v' f_{cd} \quad (2.3)$$

$$\text{With: } v' = 1 - \frac{f_{ck}}{250}$$

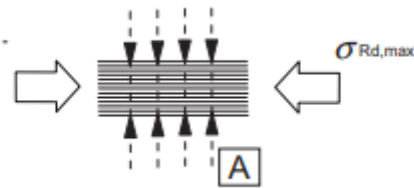


Figure 2.1.7: transverse compressive stress [13]

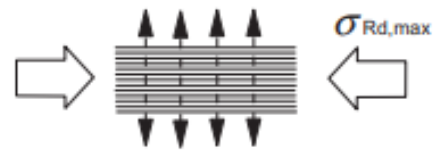


Figure 2.1.8: transverse tensile stress [13]

Ties

The ties represent the reinforcement in the concrete. The tie can be composed of one or multiple layers of reinforcement. The centre of gravity of the total applied reinforcement represents the position of the tie. The capacity of a tie is determined straight forward as $F_{tu} = f_{yd} A_s$, if no prestressing is present. The actual stress in the tie depends on the applied (vertical) load and on the internal lever arm in the section.

Nodes

The struts and the ties intersect with each other at the nodes. A node represents a volume of concrete. The forces from the struts and the ties that act on the node should be in equilibrium. Both horizontal, vertical and moment equilibrium should be satisfied. From the last one it follows that the line of action of all forces that act on the node should intersect each other at the same point.

2 types of nodes can be distinguished: concentrated nodes and smeared nodes. The smeared nodes are nodes where wide stress fields join each other or with closely distributed reinforcing bars. These nodes are according to Schlaich and Schläfer [17] not critical. The concentrated nodes are critical according to Schlaich and Schläfer. The concentrated nodes are present due to supports or concentrated loads and the deviation of forces is locally concentrated. Dimensions of the nodes are sometimes quite difficult to assume. An assumption to calculate the node dimensions can for example be that the stresses at each surface of the node should be equal. Nodes with equal stresses at each surface are called hydrostatic nodes.

4 types of concentrated nodes can be distinguished:

- C-C-C node (Figure 2.1.9)
- C-C-T node (Figure 2.1.10)
- C-T-T node
- T-T-T node

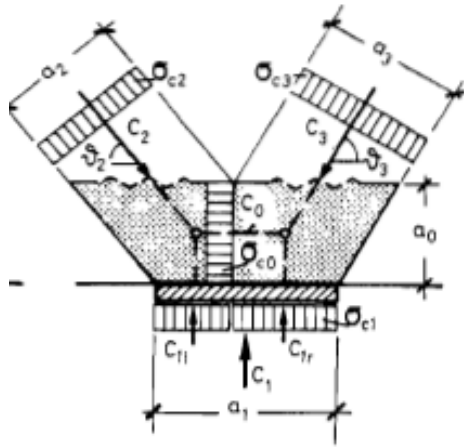


Figure 2.1.9: C-C-C node

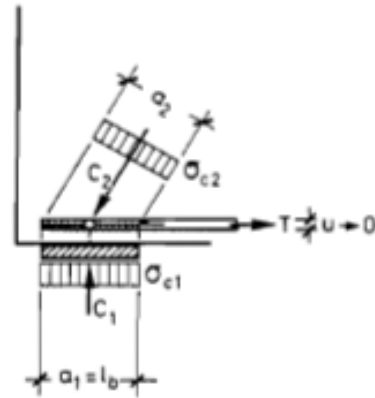


Figure 2.1.10: C-C-T node

Considering the pile caps in this study, only the first two are of interest.

Right under the column a C-C-C node is obtained. Just above the piles of a pile cap a C-C-T node is obtained, the tensile force at this node is coming from the reinforcement.

In the wall girder just above the support, a CCT node is observed.

The compressive stresses that act on the node should be checked. The forces on the nodes follow from equilibrium. The maximum stress that can be applied on a node (following the Eurocode) depends on the type of node

$$\sigma_{Rd,max} = \left(1 - \frac{f_{ck}}{250}\right) f_{cd} \quad \text{For CCC nodes} \quad (2.4)$$

$$\sigma_{Rd,max} = 0.85 \left(1 - \frac{f_{ck}}{250}\right) f_{cd} \quad \text{For CCT nodes} \quad (2.5)$$

The Eurocode states that the design compressive values (given in above formula's), may be increased up to 10% where at least one of the following applies:

- When triaxial compression is assured.
- All angles between struts and ties are larger or equal to 55° .
- Stresses applied at supports or at concentrated loads are uniform, and the node is confined by stirrups.
- Reinforcement is arranged in multiple layers.
- The node is reliably confined by means of bearing arrangement or friction.

2.1.4 Remaining challenges for strut and tie models

The strut-and-tie model is a reliable method and provides safe solutions. In the structures that are analysed in this report, it is also straightforward to use. However, there are also some challenges for designing by using the strut and tie model. According Tjhin and Kuchma (2002) [22], there are five remaining challenges in using the strut and tie method.

Designing for SLS

To be able to analyse serviceability limit state using the strut and tie model, e.g. deflection and crack width, certain values of the strut and tie model are required. For the crack width control, the effective concrete area in tension around the ties is required. For deflection control, the stiffness of the members of the truss is required.

Load-displacement response of struts and ties

Current strut and tie models do not have a feature for finding the load-displacement response of a structure. As the process of determining the stiffness characteristics of the elements (e.g. struts and ties) has not been figured out entirely.

Capacity of the struts

The inconsistency of compressive strength values that are specified in the building codes, research results or guidelines reflects the doubt that is still present on the effective compressive strength of a strut. The strength that is used in the codes is based on the uniaxial concrete compressive strength that is obtained from cylinder tests. Five factors can influence the ultimate compressive capacity of a strut:

- Disturbance in a strut
- Use of distributed reinforcement
- Shape of a strut
- Confinement
- Angle of the strut

Anchorage and distribution of tie reinforcement

To ensure that proper force transfer occurs, it is important to select the correct detailing in the nodal zone. There are however, some doubts regarding the anchorage requirements and the necessity for distributing the reinforcement over the nodal zone.

Nodal zones

There are also some uncertainties in defining the dimensions of the nodal zone (e.g. size, shape and strength). Defining the geometry of nodes is a difficult task as a large number of configuration variation could form depending on the number of stress resultants that are acting on the node. Currently, the code only provides verifications for nodal zones with three acting forces (C-C-C node, C-T-T node etc.). When more forces interact at a node, forces need to be resolved to end up with just the three resulting forces.

2.1.5 Remaining design verifications by the Eurocode

Besides checking the capacity of the nodes, concrete struts and reinforcement ties there are a few other verifications that need to be made. One of them is the orthogonal reinforcement mesh. This verification is discussed in the chapter of the struts. Remaining checks that must be made for designing the pile cap and wall girder are:

- Anchorage length
- Crack width control

Anchorage length

The basic required anchorage length when assuming constant bond stress in a straight bar is defined in the NEN-EN 1992-1-1:2005 [13] formula 8.3 as:

$$l_{b,rqd} = (\phi/4)(\sigma_{sd}/f_{bd}) \quad (2.6)$$

where:

- | | |
|---------------|--|
| ϕ | is the bar diameter in mm. |
| σ_{sd} | is the design stress of the bar at the position from where the anchorage is measured from. |
| f_{bd} | is the design value of the ultimate bond stress for ribbed bars. It is defined in the Eurocode as: |

$$f_{bd} = 2.25 \eta_1 \eta_2 f_{ctd} \quad (2.7)$$

where:

- | | |
|-----------|--|
| f_{ctd} | is the design value of concrete tensile strength. |
| η_1 | is a coefficient related to the quality of bond condition and the position of the bar during concreting. $\eta_1 = 1,0$ when 'good' conditions are obtained. |
| η_2 | is related to the bar diameter:
$\eta_2 = 1,0$ for $\phi \leq 32 \text{ mm}$
$\eta_2 = (132 - \phi)/100$ for $\phi > 32 \text{ mm}$ |

The design anchorage length is then defined in the NEN-EN 1992-1-1:2005 [13] formula 8.4 as:

$$l_{bd} = \alpha_1 \alpha_2 \alpha_3 \alpha_4 \alpha_5 l_{b,rqd} \leq l_{b,min} \quad (2.8)$$

where:

- α_1 Is for the effect of the form of the bars assuming adequate cover.
- α_2 Is for the effect of concrete minimum cover.
- α_3 Is for the effect of confinement by transverse reinforcement.
- α_4 Is for the influence of one or more welded transverse bars along the anchorage design length.
- α_5 Is for the effect of the pressure transverse to the plane of splitting along the design anchorage length.
- $l_{b,min}$ Is the minimum anchorage length.
 For anchorage in tension this is: $l_{b,min} \leq \max \{0.3l_{b,rqd}; 10\phi; 100mm\}$
 For anchorage in compression this is: $l_{b,min} \leq \max \{0.6l_{b,rqd}; 10\phi; 100mm\}$

The design anchorage length of bent bars should be measured along the centreline of the bar axis. The alpha values can be found in the Eurocode. The product of $\alpha_2\alpha_3\alpha_5$ should be ≤ 0.7 . In this research the longitudinal reinforcement starts anchoring above the supports. As stated before, in the pile caps and wall girders a CCT-node is present above the supports. In Figure 2.1.11, which is a figure from the Eurocode, it is indicated from where the reinforcement starts anchoring.

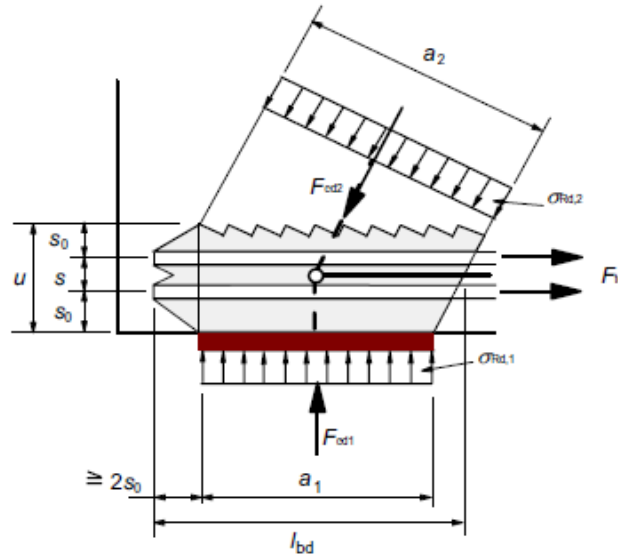


Figure 2.1.11: CCT node [13]

Crack width control

The crack width is defined in NEN-EN 1992-1-1:2005 [13] formula 7.8 as:

$$w_k = s_{r,max} * (\varepsilon_{sm} - \varepsilon_{cm}) \quad (2.9)$$

Where:

$s_{r,max}$ is the maximum crack spacing.

ε_{sm} is the mean strain in the reinforcement.

ε_{cm} is the mean strain in the concrete between cracks.

$$\varepsilon_{sm} - \varepsilon_{cm} = \frac{\sigma_s - k_t \left(\frac{f_{ct,eff}}{\rho_{p,eff}} \right) (1 + \alpha_E \rho_{p,eff})}{E_s} \geq \frac{0.6 \sigma_s}{E_s} \quad (2.10)$$

where:

σ_s is the stress in the tension reinforcement assuming a cracked section.

α_E is the ratio E_s/E_{cm} .

$\rho_{p,eff}$ $A_s/A_{c,eff}$ (no prestressing is taken into account).

$A_{c,eff}$ is the effective area of concrete in tension: $b * h_{c,eff}$ (see Figure 2.1.12)

$h_{c,eff}$ is the effective height of the concrete in tension: $2.5(h - d)$

k_t is a factor dependent on the duration of the load.

short term loading: $k_t = 0.6$

long term loading: $k_t = 0.4$

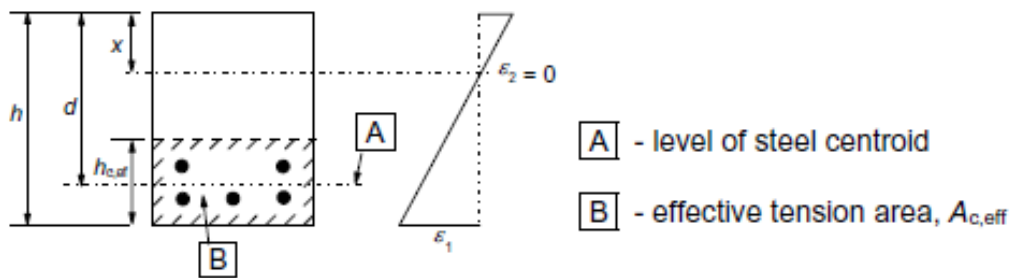


Figure 2.1.12: effective tension area in a beam cross section [13]

$$s_{r,max} = k_3 c + k_1 k_2 k_4 \phi / \rho_{p,eff} \quad (2.11)$$

where:

k_1 Is a coefficient taking into account the bond properties.
= 0.8 for high bond bars.

k_2	Is a coefficient taking into account the strain distribution: = 0.5 for bending = 1.0 for tension
k_3	3.4
k_4	0.425
c	is the cover to the longitudinal reinforcement.

The crack width that is allowed in a structure is depending on the exposure class. The cracking should not impair the durability or functioning of the structure. Maximum allowed values per exposure class are given in the Eurocode.

2.2 Finite element method

2.2.1 Principle of the finite element method

The determination of stress distribution is usually mathematically described by differential or integral equations. However, the analytical solution to these equations is sometimes quite time consuming to obtain or cannot be obtained at all. This is the case for the D-regions: regions where there is stress discontinuity and thus the analytical approach from mechanics could not be depended upon.

When the analytical solution cannot be obtained, approximate solutions from numerical analyses should be used. One of these numerical methods is the finite element method. As this gives an approximate solution, the solution from the finite element should always be validated with experiments or analytical results. Many software is available for the finite element method. Finite element analyses in this report are made using DIANA.

According the fib Model Code 2010 [9], in the evaluation of the resistance of reinforced concrete structures, four levels of approximations can be distinguished. The higher the approximation level, the more complex, but also the more accurate the approximation gets. Level I, II and III refer to analytical calculation methods. Non-linear finite element analyses fall into level IV, which is the most accurate.

In the finite element method process, three stages can be distinguished. The physical problem needs to be simplified to a mechanical model. Therefore, the physical problem needs to be properly understood. This can then be converted to a finite element model. This is the first stage: Pre-processing. Next stage is the analysis itself. After this the results needs to be post-processed. This includes some checks of verification of the obtained results, a common check is the check for force equilibrium.

The analysis is carried out by the software. The equations that are used to solve the system are collected in a matrix by the software. This matrix defines the relation between the degrees of freedom ($[u]$) and corresponding to these DOF's the forces in the nodes ($[f]$). These DOF's can be rotations and translations depending on the element type. The matrix is defined as the stiffness matrix $[K]$. An overview scheme of the procedure that is used to define the stiffness matrix is shown in Figure 2.2.1.

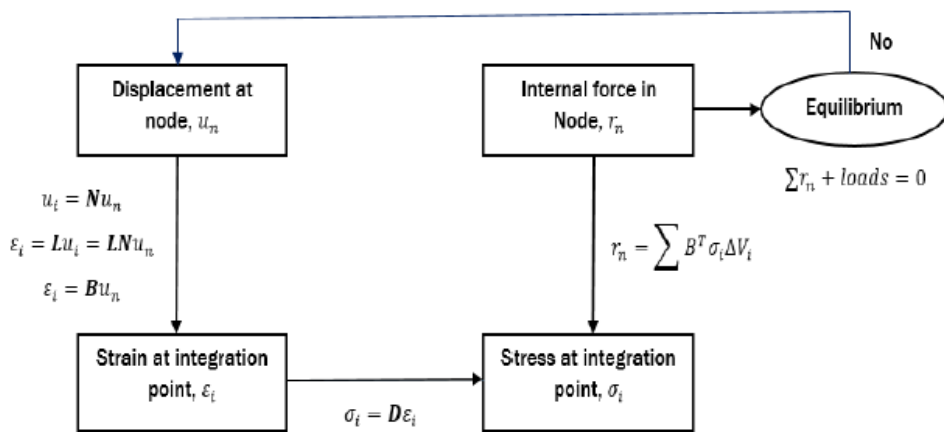


Figure 2.2.1: solution scheme of the finite element method

The relation between displacements and strains is given by the kinematic equations. The relation between strains and stresses is given by constitutive equations. The stresses and forces are related by the equilibrium equations. This is shown in Figure 2.2.2.

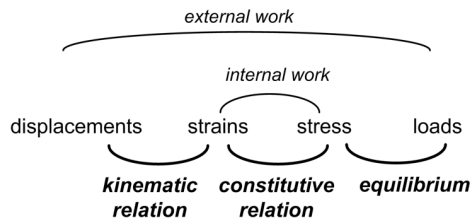


Figure 2.2.2: equilibrium equations

If any of these equations is nonlinear, the process gets more complicated. Nonlinear relations can be distinguished in physical nonlinearity and geometric nonlinearity.

- Physical nonlinearity – in this case the material model is nonlinear. Material properties are functions of the state of stress or strain. This is the case for most structural materials. This source of nonlinearity is of high importance for this research as concrete shows nonlinear behaviour (cracking, crushing, softening) but also the reinforcement steel shows nonlinear behaviour (plasticity).
- Geometrical nonlinearity – In this case either the equilibrium or the kinematic equation is nonlinear. This should be used in buckling analyses. Due to the large deformations in flexural buckling the equilibrium equations should be based on the deformed geometry instead of the initial geometry (linear).

In this report, the focus will thus be on physical nonlinearity. Reinforced concrete is a nonlinear material.

2.2.2 Non-Linear FEA of Reinforced Concrete structures

Modelling of reinforced concrete requires a nonlinear analysis. As the material behaves nonlinear, physical nonlinearity needs to be considered. This makes the finite element calculation more difficult than a linear analysis.

M.A.N. Hendriks, A. de Boer and B. Beletti in 2019 [10] provided Guidelines for the application of Nonlinear Finite Element Analysis on concrete structures. These guidelines are applicable for nonlinear finite element analysis regarding the safety verification under quasi-static, monotonic loading. The guidelines are restricted to be used for existing prestressed and reinforced concrete structures. In their report it is stated that “hidden” capacities can be obtained by making a nonlinear finite element analysis.

Nonlinear Finite Element Analyses become more and more important in the daily design process. However, the problem with FEM is that the results strongly depend on the choices that are made in the process of modelling. When several analysts are asked to model the same structure, a big scatter in results can be detected due to different manners of modelling the considered structure. The Guidelines are made to reduce this scatter.

In order to be able to model the reinforced concrete correctly, its nonlinear material properties and how this can be modelled in DIANA should be understood properly. As stated before, reinforced concrete shows nonlinear behaviour. This nonlinear behaviour originates from different sources caused by both the concrete and the reinforcement.

Cracking

Concrete responds very different in tension compared to its response to compression. The tension strength of concrete is very low compared to the compression strength. A stress-strain curve for concrete loaded in both tension and compression is shown in Figure 2.2.3.

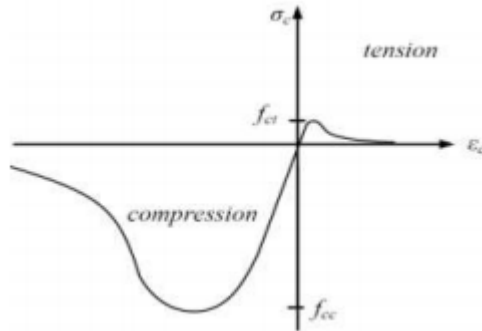


Figure 2.2.3: Concrete loaded in compression and tension

As can be seen from the figure, concrete responds linear elastic to tension until the tensile strength is reached (f_{ct}). When the tensile strength is reached, stable cracks are initiated in the concrete. These cracks are orientated perpendicular to the direction in which the tensile stress is introduced. When increasing the strain after this point, the load capacity decreases rapidly. This is because the cracks that were formed earlier develop into a system of continuous cracks. After cracking, the concrete is still able to resist some tensile stresses across the crack (if the crack width is small). These stresses decrease as the crack width increases, this is called tension softening. As these stresses are small, they are usually ignored, and it is assumed that the reinforcement needs to take all tensile stresses after the tensile strength of concrete is reached.

In finite element software, the cracking of concrete can be modelled in two ways. Smeared cracking and discrete cracking can be used. For discrete cracking the deformations are lumped into a line or a plane. Interface elements are predefined in the mesh at location where cracks are expected to be formed. Interface elements are elements in between the continuum elements (concrete) that have different stiffness and deform more when the tensile strength is reached. Discrete cracking allows a gap between the continuum elements, which represents a crack. The interface elements have an initially high stiffness, this is called the dummy stiffness. The initial stiffness is large because initial elastic deformation of the interface element should be negligible compared to the deformations of the surrounding continuum elements. When the tensile strength is reached in the concrete, a softening crack opens up.

Smeared cracks are different than discrete cracks. Smeared cracks can occur anywhere in the structure in any direction, while discrete cracks can only occur at predefined locations (where the interface elements are modelled). The crack is now 'smeared' over an element and is shown in the model by large strain over an element. Difference between smeared cracks and discrete cracks is that the smeared cracks are expressed in strain and the discrete cracks are expressed as an actual crack width. Both crack models are dependent on the tensile strength (f_t), the fracture energy (G_f) and the shape of the softening diagram. This is shown in Figure 2.2.4. For the smeared cracking model there is one extra parameter h , this represents the crack band width over which the crack is smeared out. There are two different smeared

cracking models. The fixed model determines the orientation of the crack by the direction of the principal stresses that initiated the crack. After further loading, this crack remains its direction. This can cause shear stresses on the crack face as the principal stresses may change direction after cracking.

In the rotated crack model, the orientation of the crack is able to change direction. The direction of the principal stresses always coincides with that of the principal strain for this model.

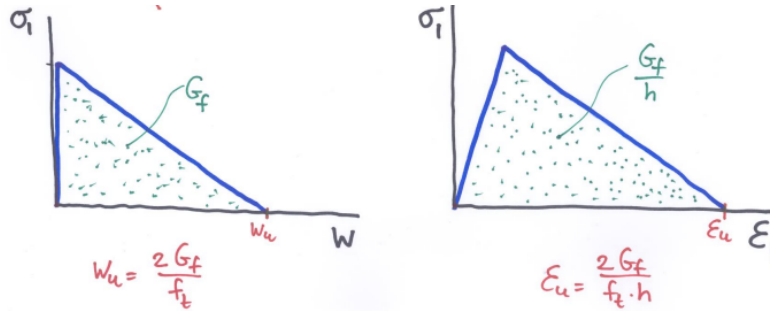


Figure 2.2.4: Cracking models with linear softening

Drawback of the discrete cracking model is that this model does not fit the nature of the finite element displacement method. This is due to a discontinuity of displacements between the continuum elements. Another drawback is that the crack is constrained to follow a path which is predefined along the edges of the elements. A smeared crack model is more convenient computationally, as not all expected crack locations have to be predefined in the model. However, the discrete cracking model gives a better reflection of reality as it creates a discontinuity. The smeared crack approach uses displacement continuity which conflicts with reality.

In the figures above linear softening is shown. For modelling the concrete in tension however, an exponential softening diagram is preferred. Either the exponential softening diagram or the Hordijk softening diagram can be used, if available. Reason for this is because the exponential-type diagram will result in more localized cracks and will avoid large areas of diffuse cracking. The Hordijk softening diagram and the exponential softening diagram are shown in Figure 2.2.6 And Figure 2.2.5 respectively.

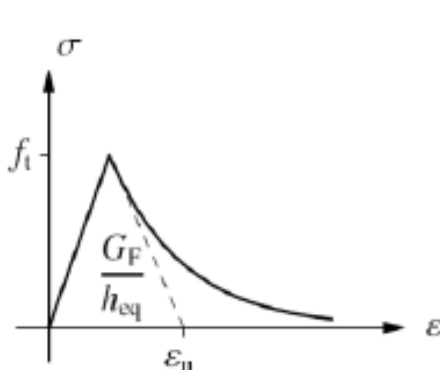


Figure 2.2.5: Exponential softening [10]

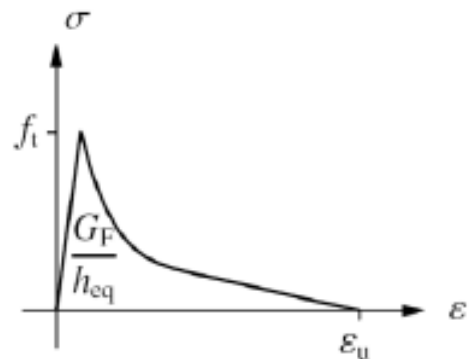


Figure 2.2.6: Hordijk softening [10]

The exponential softening relationship is given by formula 2.12.

$$\sigma = f_t \exp\left(-\frac{\varepsilon^{cr}}{\varepsilon_u}\right) \quad (2.12)$$

The Hordijk softening diagram is given by formula 2.13.

$$\sigma = \begin{cases} f_t \left(1 + \left(c_1 \frac{\varepsilon^{cr}}{\varepsilon_u}\right)^3 \exp\left(-c_2 \frac{\varepsilon^{cr}}{\varepsilon_u}\right) - \frac{\varepsilon^{cr}}{\varepsilon_u} (1 + c_1^3) \exp(-c_2)\right) & 0 \leq \varepsilon^{cr} \leq \varepsilon_u \\ 0 & \varepsilon^{cr} > \varepsilon_u \end{cases} \quad (2.13)$$

The usual parameters c_1 and c_2 are 3.0 and 6.93 respectively.

The ultimate strain for the exponential and Hordijk diagram is respectively given by:

$$\varepsilon_u = \frac{G_F}{h_{eq} f_t} \quad \varepsilon_u = 5.136 \frac{G_F}{h_{eq} f_t}$$

h_{eq} is the equivalent length. The equivalent length is an essential parameter for the softening stress-strain relationship and is also known as the crack band width. Following the guidelines [10], the effective length should be determined using an automatic procedure. A method based on the initial crack direction and the element size is preferred. Alternatively, it can be determined based on the area or volume of the finite element.

Tension Stiffening

When concrete in a tension zone is cracked, the concrete is assumed to have no stiffness and the tensile forces are carried by the reinforcement entirely. However, the concrete does contribute to the stiffness in between the cracks. There is a difference in response between a bar embedded in concrete and a bare bar. This mechanism is referred to as tension stiffening. A higher capacity is obtained for an embedded bar compared to a bare bar, this is shown in Figure 2.2.7. This higher capacity is caused by the contribution of concrete in between the cracks.

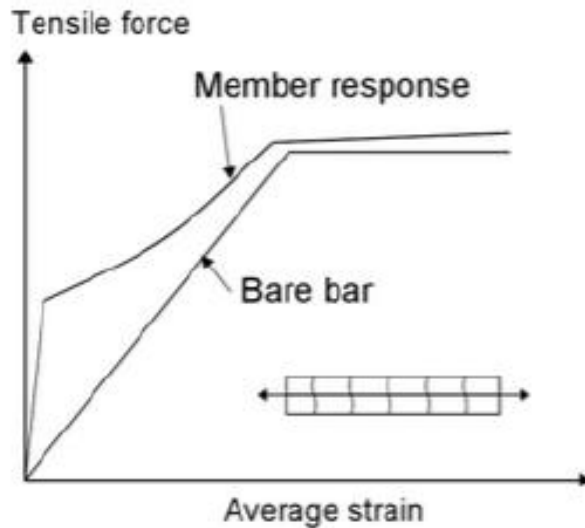


Figure 2.2.7: Tension stiffening effect

The tension stiffening effect can be modelled by modifying the stiffness of either the reinforcement bar or the concrete.

The Guideline for Nonlinear Finite element calculations [10] states that the tension-stiffening effect needs to be taken into account. It is a conservative assumption to only account for the energy dissipated in the cracks and thus neglect tension stiffening.

The tension-softening model can be used if the element size is smaller than the estimated average crack spacing. Otherwise, according to the guidelines, the amount of energy that can be dissipated within a finite element should be related to the size of the element and the average crack spacing. The amount of energy that is released is calculated through formula 2.14.

$$G_F^{RC} = n_{cr} G_F \quad (2.14)$$

where

n_{cr} is the number of cracks, given by:

$$n_{cr} = \max\left(1, \frac{h_{eq}}{s_{r,max}}\right)$$

The crack spacing ($s_{r,max}$) can be determined by the formula that is given in chapter 2.8 of this report.

In this calculation it is assumed that the crack direction is approximately orthogonal with respect to the reinforcement.

Bonding

For low stress levels, the bond is covered by adhesion. When the stresses increase, the bond is covered by the bearing of ribs against the concrete. Cracks around the crest of the bars are formed due to this bond. The bearing forces are acting on the concrete inclined to the bar axis. This is shown in Figure 2.4.7a. This force can be resolved into a force parallel to the bar axis and a force perpendicular (radial) to it. This parallel component can lead to pull-out failure. This failure mechanism occurs when a sliding plane is formed around the bar due to shearing off of the concrete within the ribs (Figure 2.2.8b).

A radial crack can propagate to the cover due to the radial component of the force, this is referred to as splitting bond failure.

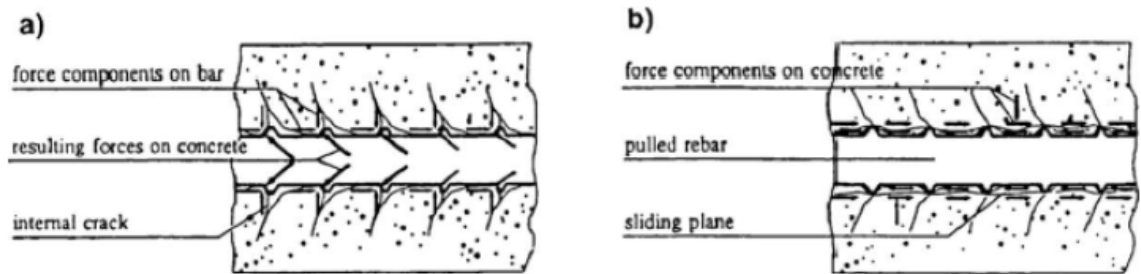


Figure 2.2.8: Bonding of ribbed reinforcing bars in concrete

For parts loaded in compression, uncracked parts loaded in tension and for linear elastic analyses, assuming perfect bond suffices. By assuming perfect bond, the displacement of the steel and the concrete is kept the same (no slip).

In cracked sections however, there is a difference between the displacement of the steel and the concrete as the tensile force is now transferred by the steel. Finite element software makes it possible to take these differences in displacements into account by using bond models. In these bond models a relationship between the bond stress and the relative slip between the reinforcement and the concrete is assumed.

The Guideline for Nonlinear Finite element calculations [10] states that bonding can be modelled if an appropriate model is available.

Crushing

Also in compression, nonlinear material behaviour of concrete is observed. From Figure 2.2.9 the nonlinear stress-strain relationship of concrete in compression can be observed. It shows an initial, nearly linear elastic response. After this the stiffness gradually decreases due to microcracks in the material. After the peak stress is reached, strain softening is observed in the concrete until final failure due to crushing takes place.

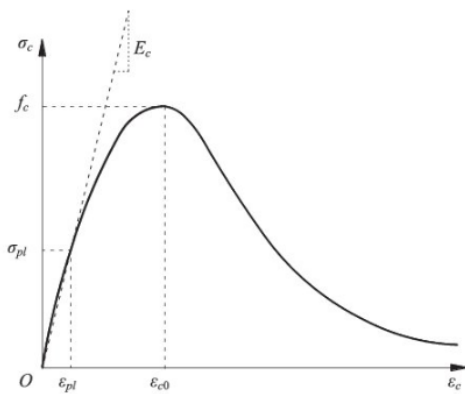


Figure 2.2.9: Concrete loaded in compression

The guideline states that the compressive behaviour needs to be modelled such that the maximum compressive stress is limited. It recommends using a parabolic stress-strain diagram with softening branch. In order to reduce mesh size sensitivity, this softening branch should be based on the compressive fracture energy.

It is not recommended to use models that only limit the concrete compressive strength. An example of such a model is the simple elasto-plastic diagram, which is shown in Figure 2.2.10. When using such a model in the analysis, a post-analysis check of the compressive strains should be included in the procedure.

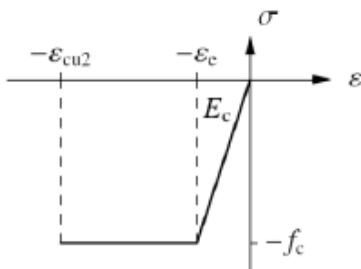


Figure 2.2.10: elasto-plastic approach [10]

Yielding and strain hardening

Also the reinforcing steel shows nonlinear material behaviour. Steel exhibits elasto-plastic behaviour. The elastic limit of the reinforcing steel is the yield strength. Hardening is defined as the post-yielding behaviour and this should also be included in the material model for the reinforcing steel. After yielding, the stiffness should be adjusted to the hardening modulus. The code states that if no specifications of the reinforcing steel are given, a nominal hardening modulus of for example $E_{har} = 0.02 E_s$ can be used. The stress-strain relation that follows from this description is shown in Figure 2.2.11.

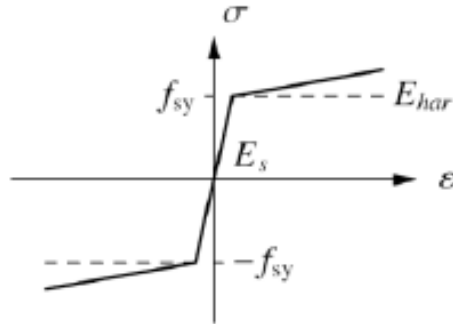


Figure 2.2.11: Nonlinear *bf* the reinforcing bars [10]

The guideline states that an elasto-plastic material model with hardening should be used.

2.2.3 Safety formats

Goal of this thesis is to adjust the design verifications of the code by making a nonlinear finite element analysis. This is done by comparing the results of nonlinear finite element analyses with results of the verifications by the norm.

In the Eurocode material factors and load factors are used in the calculation. To be able to compare this to a finite element model, we need to know what values of the material properties needs to be used (characteristic, mean etc.). The answer to this is given by both the Eurocode [13] and the fib Model Code 2010 [9]. ‘Safety formats’ are prescribed. Three safety formats are prescribed in the fib Model Code 2010:

- GRF (Global Resistance Factor)
- PF (Partial Factor)
- ECOV (Estimation of Coefficient of Variation)

The safety formats are used to discount the uncertainties in the material, load and model. The design process following nonlinear finite element calculations differs from the design process of the analytical calculations. Using the design values of material properties in nonlinear analyses is not recommended. These conservative values can lead to non-realistic failure modes in the nonlinear finite element analysis. To come to a comparable safety level, a higher design load will be used.

Global Resistance Factor

The GRF-method uses 'mean' material values. 'Mean' should not be interpreted as the real mean values, but these values are derived from the characteristic values and take into account the uncertainty between steel and concrete parameters. The more scatter in concrete properties compared to steel properties, leads to a reduction of the characteristic value of concrete strength as 'mean' value: $0.85 f_{ck}$. For steel an increase of the characteristic value is specified as the 'mean' value: $1.1 f_y$. The capacity that follows from the calculation will be divided by 1.27 to be defined as the design capacity, this results in formula 2.15.

$$R_d = \frac{R_{u,calc}}{1.27} \quad (2.15)$$

For this method, only one nonlinear finite element calculation needs to be made.

Partial Factor

The Partial Factor-method is similar to the GRF-method. For the Partial Factor-method the strength parameters are assumed to be lower than for the GRF-method. A reduction of the characteristic value of the concrete strength of 1.5 is used ($f_{ck}/1.5$). On the strength of steel, a reduction factor of 1.15 is used ($f_y/1.15$). The capacity that follows from the calculation with the use of these values is already defined as the design capacity (R_d), no further reduction factor needs to be applied. Also for the Partial Factor-method, only one nonlinear finite element calculation needs to be made.

Estimation of Coefficient of Variation

An alternative method that can be used is the Estimation of Coefficient of Variation (ECOV) Method. This method is based on two nonlinear finite element calculations. One calculation makes use of mean material values and the other uses characteristic material values in its calculation. This results in a capacity for the mean values and a capacity for the characteristic values, respectively R_m and R_k . The following formulas are then used to obtain the design capacity:

$$R_d = \frac{R_m}{\gamma_{Rd}\gamma_R} \quad (2.16)$$

where:

γ_{Rd} is the model uncertainty coefficient
= 1.06

$$\gamma_R = \exp(\alpha_R \beta_R V_R) \quad (2.17)$$

where:

α_R = 0.8

β_R is the reliability index
= 3.8

V_R Is the coefficient of variation
= $\frac{1}{1.65} \ln\left(\frac{R_m}{R_k}\right)$

This method is based on the assumption of a lognormal distribution of the resistance of concrete, defined by two parameters.

On the cover of the guidelines for nonlinear finite element analysis of concrete structures [10] the graph in Figure 2.2.12 is present.

The graph shows the relation between the calculated capacity and the experimentally obtained capacity for different methods. The graph indicates that the results obtained from nonlinear finite element calculations lay in between the Eurocode results and the experimentally obtained results. In other words, it gives a better prediction of reality as the results are closer to the experimental results.

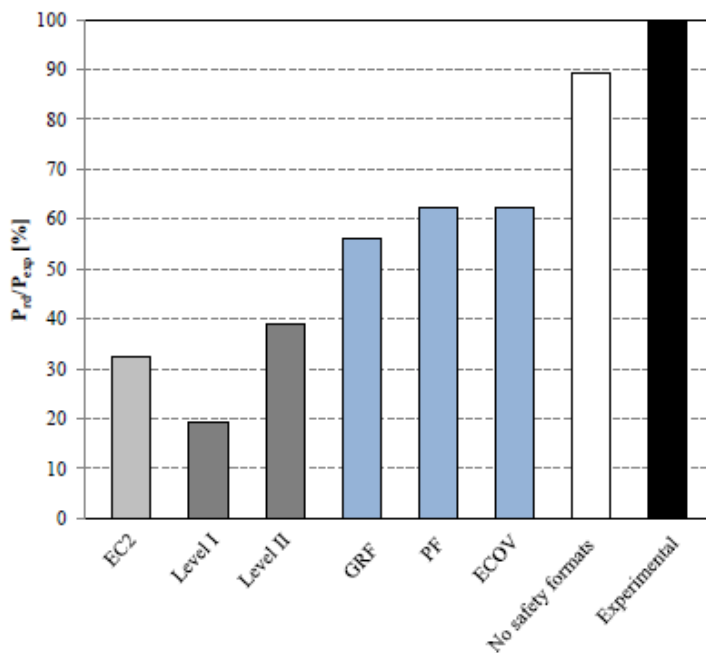


Figure 2.2.12: Calculated capacity vs experimentally obtained capacity [10]

2.3 Previous Research

On the structural elements that are considered in this report, numerous experiments have been carried out in the past. Goal of this research is to adjust the current design codes, where possible, based on a finite element analysis. Adjustments based on just a finite element analysis would be insufficient, experiments should be used to verify the obtained results from the finite element analysis. Based on these previous experiments, a study can be performed on the influence of certain parameters on the load capacity of the structural elements. Based on this study a choice can be made on what parameters to vary in the analyses.

Previous researches are performed on reinforced concrete structures by making use of DIANA. The properties of the constitutive relations that are used in these researches are studied in this chapter.

As was already mentioned earlier in this report, setting up a strut-and-tie model for a continuous wall girder is more complex. Therefore, previous researches on strut-and-tie modelling of wall girders on three supports are studied in this chapter.

2.3.1 Previous experiments on pile caps

Numerous experiments on the behaviour of pile caps have been carried out in the past. These experiments have been performed to study, among other things, the influence of the reinforcement layout and the slenderness of a pile cap on the capacity of the pile cap.

Adebar and Zhou [4] provided in 1996 an article where test results of pile caps from numerous experiments are discussed. A total amount of 48 different pile cap tests are discussed in the paper. The pile cap models that are tested are different in size and in reinforcement layout etc. The pile cap models that are discussed in the paper originate from different experimental researches.

Several researches were done to the design procedure for the pile caps that was suggested by the ACI Building Code (ACI = American Concrete Institute). Following the design procedure suggested by the at that moment active ACI Code, the longitudinal reinforcement in a four-pile cap should be spread out over the width uniformly. In the code, flexural design was used to design the longitudinal reinforcement. As explained earlier in this report, the pile caps are structures with a short span and relatively to that a large height (deep beams). For these deep beams the assumptions that are made for flexural design are not valid.

The strut-and-tie-model gives more insight and a better approximation of the flow of forces in the pile caps.

The ACI Building code suggested a shear check based on a sectional approach. A sectional depth should be sufficient for avoiding failure modes that are related to shear. In previous researches it is however concluded that the ACI Building Code overrates the effective depth significantly. Results of experiments show that this approach of shear can be unconservative for designing deep structural elements, testing of reinforced concrete deep beams designed for flexural failure namely failed in shear. Adebar et al [3] concluded in their experimental research in 1990 that the sectional design method is applicable when the shear span over depth ratio is more than 1.5. They state that when the shear span over depth ratio is less than 0.5, members are controlled by splitting failure.

Deutsch and Walker [8] performed experiments in 1963 on full-scale two-pile cap specimens.

They tested four specimens and goal of the research was to investigate the effect of the amount of reinforcement in the pile caps and the pile cap depth. The specimens they made appeared to be stronger than anticipated, two of the specimens did not fail during the tests. All pile caps behaved similarly, in all of the pile caps one main vertical crack formed at midspan.

In 2015 Abdul-Hameed [1] investigated the influence of several parameters on the behaviour of two-pile caps. He studied the influence of both the horizontal and vertical shear reinforcement (ρ_h and ρ_v respectively), the shear span to effective depth ratio (a/d), the longitudinal reinforcement ratio (ρ) and the compressive strength of the concrete (f_c). From his research he concluded that a decrease in shear span over effective depth ratio, the ultimate shear capacity will increase (e.g. increase in height or decrease of span). Following his tests lead a decreasing ρ_v while increasing ρ_h to a higher diagonal cracking shear strength. Increasing the longitudinal reinforcement will, following his research, result in an increase in ultimate shear strength and diagonal cracking shear strength. Also, an increase of concrete compressive strength will result in a higher ultimate shear strength.

Khattab Saleem Abdul-Razzaq and Mustafa Ahmed Farhood [2] tested 12 pile caps in 2018. They made 4 specimens each for a two-pile cap, three-pile cap and a four-pile cap. In their research they present a new perspective in the design of reinforced concrete pile caps. They made for each pile cap four specimens, two of those specimens contain a reinforcement design based on the design procedure according to the ACI. For the other two specimens they proposed a new design. They only reinforced the load paths that follow from the strut and tie model and omitted the shoulders (e.g. the upper corner parts of the pile caps, above the struts) of the caps, to reduce weight and costs. Failure modes of all specimens turned out to be the same, for all specimens a flexural failure was induced. All specimens designed by their proposed reinforcement method had a greater capacity than the one designed by the ACI Building Code.

The difference between the reinforcement design of their specimens is shown for the two pile caps in Figure 2.3.1 and Figure 2.3.2.

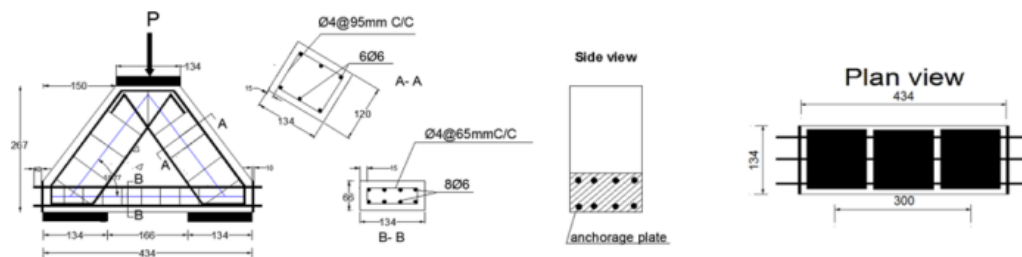


Figure 2.3.1: Reinforcement design in two-pile cap for proposed design procedure [2]

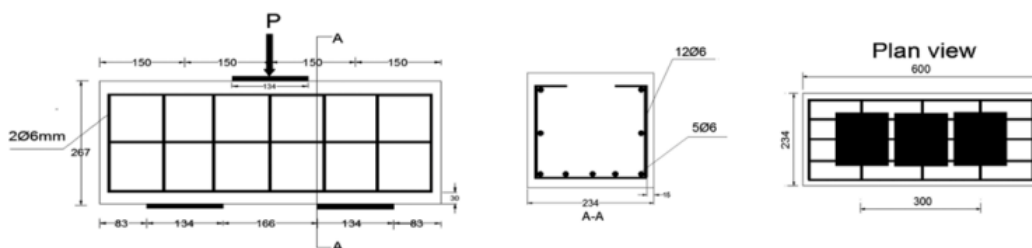


Figure 2.3.2: Reinforcement design in two-pile cap based on ACI Building Code [2]

They concluded in their research that reinforcing the stress paths according the strut and tie model is useful, and so is removing the shoulders of the pile caps. The pile caps based on their design showed a higher ultimate capacity and a reduction in costs. The differently designed pile caps showed similar cracking behaviour, and both specimen types failed in flexure. They state that the difference in strength is caused by exaggerating the importance of the effective depth by the code and neglecting the influence of the longitudinal reinforcement amount.

From these previous researched we can conclude various things. Although all researches are comparing experimental results to the design method by the ACI Building Code instead of the Eurocode, we can conclude what parameters are affecting the capacity of the pile caps the most. An important factor in designing of the pile caps is the shear span to depth ratio of the pile cap. This shear span to depth ratio defines the angle of the stress path from the column to the piles, e.g. the angle of the strut. This shear span to depth parameter has influence on the reinforcement design, for example on the orthogonal reinforcement mesh. When the struts get steeper, the transverse tensile stresses in the struts will get less steep, and this suggests that transverse horizontal reinforcement will be more effective than vertical shear reinforcement. This would thus be an interesting factor to vary in the analyses.

2.3.2 Previous experiments on wall girders

Wall girders are a type of deep beams, the span to depth ratio of these structural elements have low values. As the depth is relatively large compared to the depth of normal beams, a nonlinear strain distribution is obtained over the cross section. This can be explained by the D-regions that were discussed earlier in this report. Shear behaviour of reinforced concrete beams already is influenced by numerous parameters and is therefore already quite complex. For deep beams this complexity is more pronounced due to nonlinear strain distribution over the cross-section. The strut-and-tie method gives a good approximation to model the nonlinearity in the structural element. As mentioned before, the Eurocode allows the application of the strut and tie method, it even recommends its application for deep structural elements such as wall girders and pile caps. The Eurocode provides design verifications for the struts, ties and nodes that result from the strut and tie model. It however lacks some guidance regarding the dimensions of the nodes and the struts. A research from Kamaran S. Ismail [11] in 2018 investigates the selection of appropriate dimensions for the strut and tie model and appropriate effectiveness factors based on experimental and numerical studies.

In their paper they make use of the following formulas for the strut dimensions:

$$W_{ST} = l_{PT} \sin\theta + h_{CS} \cos\theta \quad (2.18)$$

$$W_{SB} = l_{PB} \sin\theta + h_{TIE} \cos\theta \quad (2.19)$$

These formulas are specified in the ACI, the ACI however gives no guidance on the values that should be used for h_{CS} , h_{TIE} and θ . In the paper, h_{TIE} is assumed to be twice the distance from the center of the main longitudinal reinforcement to the outer face of the beam. This is also indicated in Figure 6.27 of section 6.5.4 in the Eurocode. h_{CS} is defined in formula 2.20.

$$h_{CS} = \left[\sqrt{(n\rho)^2 + n\rho} - n\rho \right] d \quad (2.20)$$

Where:

n is the ratio of steel to concrete elastic moduli.
 ρ is the longitudinal reinforcement ratio

θ is defined in the paper as:

$$\theta = \tan^{-1} \frac{d \frac{h_{CS}}{2}}{a} \quad (2.21)$$

All other dimension that are used in the formulas above, are indicated in Figure 2.3.3. Values for h_{CS} and θ are not indicated in the Eurocode.

The paper also gives proposed values for the following factors:

- Node strength factor
- Effectiveness factor for inclined Strut

These proposed dimension and factors can be used in the analyses and in the verification of results obtained from the Finite element analyses. These factors and dimensions are not only applicable for the wall girders, they can also be used for the pile cap analyses.

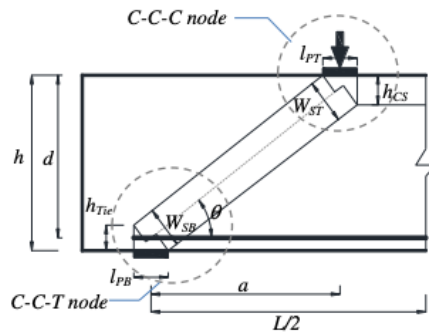


Figure 2.3.3: strut in a wall girder [11]

N.K. Subedi et al. [20] tested thirteen simply supported deep beams with span over depth ratios of 1, 2 and 3 with percentage of main reinforcement ranging from 0.22-1.16 %. The spans of the tested specimen ranging between 500 and 2700 mm. Goal of their research was to provide experimental information about the range of failure modes that should be considered in the design, they mention 3 types of failure modes. They state that based on extensive experimental research done in the past, the by far most common failure mode is diagonal splitting. A diagonal splitting crack grows outwards from mid-depth, this failure mode is more brittle than the other 2, namely flexure and flexural shear. The failure modes are presented in Figure 2.5.5. 5 beams failed in flexure, but all of these beams had relatively low amounts of main reinforcement. The beams containing higher amounts of longitudinal reinforcement, all failed due to diagonal splitting. The failure loads and cracking loads of all beams are specified in the paper, this can be used in verifying the analyses in this report.

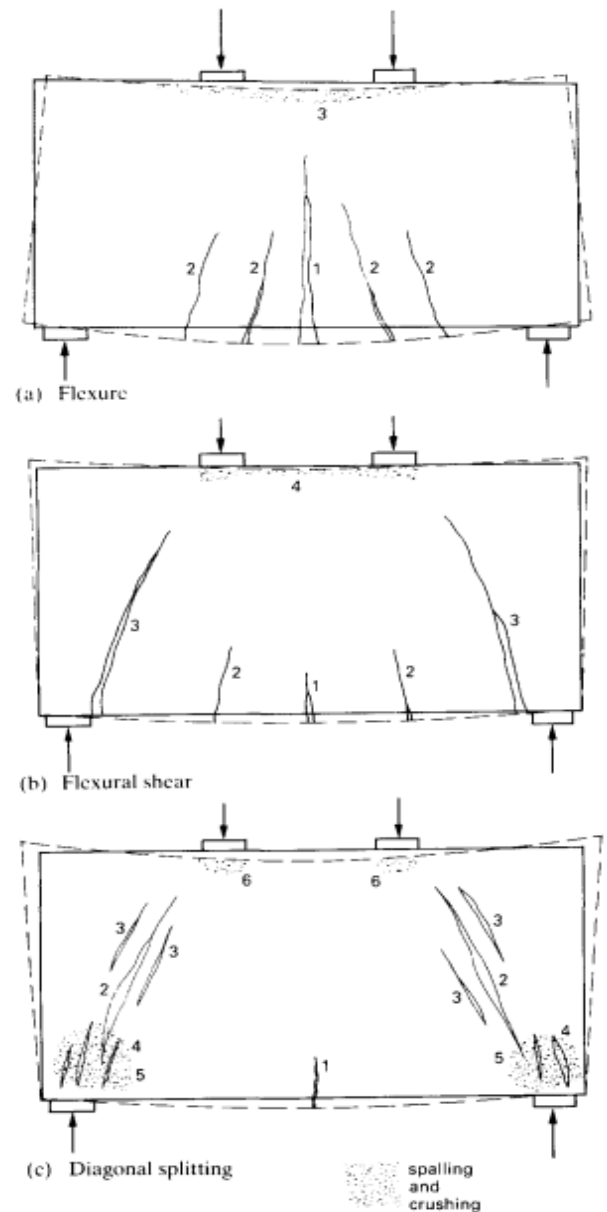


Figure 2.3.4: Failure modes of a wall girder [20]

Yang and Ashour [24] did research on deep beams in 2008. They based their research on experimental results of 75 two-span deep beams compiled from different sources, forty-four specimens were tested by themselves. In their paper they state that “both simple and continuous deep beams are quite dissimilar in the state of stresses of concrete struts, which are the main load transfer elements”. Previous experiments on continuous deep beams also showed that formulas developed for simply supported deep beams are not applicable for continuous deep beams. Goal of their research is to produce a comprehensive data base of continuous deep beams that were tested by different researches. This ‘database’ is presented in the paper, the experimental results that are presented in there can be used for

the analyses of this report. Another goal of their research was to study the influence of certain parameters on the capacity. The parameters considered are the compressive strength, shear span to depth ratio, main reinforcement ratio and shear reinforcement ratio. The shear span to depth ratio of the beams considered in this research range from 0.5 to 2.0. All beams reported to fail in shear. The failure was induced by a major diagonal crack from the loading plates the intermediate support. Strut and tie model of the continuous deep beams is shown in Figure 2.3.5.

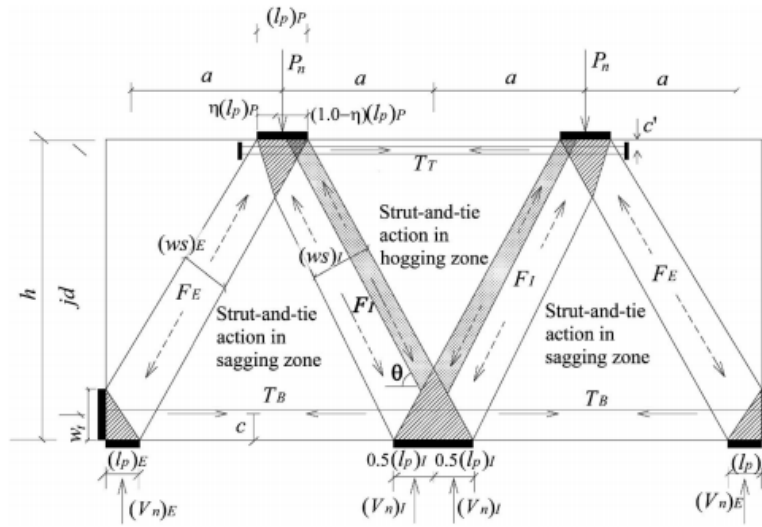


Figure 2.3.5: Strut and tie model of a continuous deep beam [24]

From their research they concluded that the amount of longitudinal reinforcement has more influence on the load capacity than that is assumed by the strut and tie method. For beams with shear span over depth ratio of 0.6 and lower, the load capacity increases when the horizontal shear reinforcement is increased.

2.3.3 Application of 2D NLFEA in previous studies

Sugianto [21] and Bhattarai [6] both did research for their master thesis that includes a nonlinear finite element analysis of reinforced concrete structural elements. Both made 2D nonlinear finite element analyses in DIANA. It is useful for this research to discuss the way they modelled their reinforced concrete structural elements.

In both researches the same elements were used to model the concrete, quadratic plane stress elements (CQ16M). These elements contain 8 nodes with 2 degrees of freedom per node.

A total strain based (smeared) crack model is used in both researches. Bhattarai used a total strain based fixed crack model while Sugianto used a total strain based rotating crack model. The Guidelines [10], approve both the fixed and the rotating crack model to be used. It is however stated that if a total strain based fixed crack model is used, an adequate shear retention model should be used. For fixed crack models a variable shear retention model is strongly recommended, Bhattarai however uses a constant shear retention.

Both Bhattarai and Sugianto use the Rots crack band width specification.

Sugianto used the Hordijk tension softening model, while Bhattarai used the exponential softening model. Both softening models are allowed to be used by the guidelines.

For the compression behaviour of concrete, both used the parabolic behaviour with the Vecchio & Collins 1993 compressive strength reduction model to consider the compression-tension interaction. The guidelines recommend the use of a parabolic stress strain diagram in compression, they also state that compression-tension interaction needs to be considered and specify the Vecchio & Collins 1993 model as a solution for this.

A lower bound reduction curve of 0.4 was used in both analyses. A Selby & Vecchio stress confinement model was used and a damaged based Poisson's ratio reduction model in both analyses. The guidelines state that no compression confinement model needs to be specified as ignoring confinement effects is a conservative assumption. For this research however, a confinement model will be used.

In both researches embedded reinforcement is used with a quadratic interpolation scheme. Both researches neglected the tension stiffening effect, which is allowed to be neglected by the guidelines. By making use of embedded reinforcement, no bond-slip behaviour is added in the model. It is also allowed by the guidelines to neglect this behaviour.

In both researches the load was applied displacement controlled. A Full Newton Raphson Equilibrium iteration was used, and maximum number of iterations was set at 50. Force norm and energy norm tolerances were set at 0.01 and 0.001 respectively.

2.3.4 Previous researches on strut-and-tie modelling of continuous wall girders

Where the strut-and-tie model of a pile cap or a simply supported wall girder is relatively straightforward, this process becomes more difficult for a wall girder on three supports. One of the complications is the distribution of the reaction forces, the intermediate support does not bear the same load as the outer supports. Blaauwendraad [7] discussed this issue in an article in Cement in 2012.

In this article three situations are considered. The situations are distinguished by the moment at the intermediate support. A clearly negative moment, clearly positive moment and a transition area are considered. This moment is based on the span to depth ratio of the wall. When the span to depth ratio becomes larger, the intermediate support reaction becomes larger. The ultimate situation for this is the behaviour of an elastic beam, the intermediate support reaction and outer support reaction for an elastic beam on three supports is equal to $\frac{10}{8}ql$ and $\frac{3}{8}ql$ respectively. When the wall becomes 'deeper' the reaction forces are distributed more equally.

Another problem in finding a suitable strut-and-tie model is assuming credible strut angles. However, no relevant information is found in literature for this problem. Test specimen in literature are generally loaded with point loads at midspan, which makes it clear what the strut angle is. In this study however, the wall girder is loaded by a uniformly distributed load. In various studies it is mentioned that the strut-and-tie model for a continuous wall girder can be designed based on principal stress directions that can be computed using nonlinear finite element analyses. In the compendium of the Concrete Structures 3 course of the department of structural engineering structures of the Norwegian University of Science and Technology [19] a strut-and-tie model is designed based on the principal stresses in the continuous wall girder. This strut-and-tie model is presented in Figure 2.3.6. This model is used in the calculation of the continuous wall girder in this report

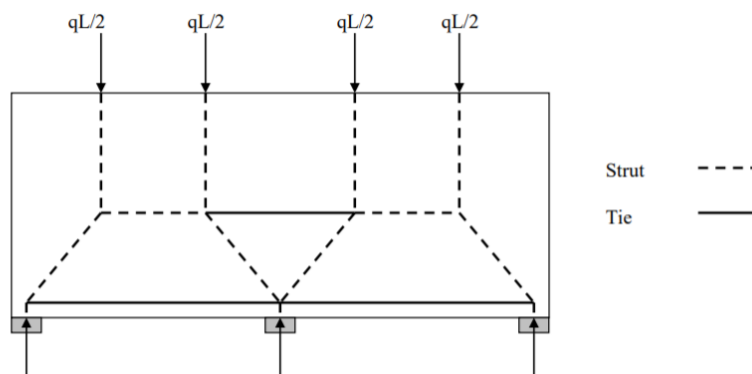


Figure 2.3.6: Strut-and-tie model of continuous wall girder [19]

2.4 Conclusion

The Literature review that is performed in this chapter provides background information that is needed to perform the analyses.

Regarding the strut-and-tie model analyses, it can be concluded that a few challenges need to be faced in this design process. Most important challenge for the strut-and-tie analyses in this report is the dimensioning of the nodal zones. For CCC nodes, no guidelines regarding what dimensions need to be used are given in the Eurocode.

Regarding the nonlinear finite element analysis, it can be concluded that this is a useful method to design the reinforcement of a structural element. However, many choices need to be made in the modelling of reinforced concrete (crack model, reinforcement steel etc.). To be able to conclude which outcomes of the finite element analysis are representative and can be used in drawing conclusions, the finite element model needs to be verified using experimental results. To be able to compare the finite element results to the strut-and-tie model results, a safety format needs to be used. Safety formats aim that the same level of safety is used in both calculation methods.

Experimental researches are performed in the past on the considered structural elements. The parameter that has the most influence on the behaviour of the structural elements appears to be the shear span to depth ratio. This parameter after all determines if the load is transferred to the support directly and at which angle this strut is then present. It is therefore interesting to vary this (shear) span to depth ratio in the analyses.

Previous master theses are available which focus on using nonlinear finite element analyses. In these previous researches, the constitutive models of the concrete and its reinforcement are selected by making use of the Guidelines for the application of Nonlinear Finite Element Analysis on concrete structures [10].

Where the strut-and-tie model can be composed relatively easily for the pile cap and the simply supported wall girder, it can be concluded that this process becomes more difficult for a continuous wall girder. Challenges in composing a representative strut-and-tie model are the distribution of the reaction forces of the supports and the angles of the struts.

3 Specifications and verification of the FE model

In this Chapter the specifications of the finite element model that will be used to model reinforced concrete will be specified. The constitutive model and the choice of elements that will be used are discussed. Also, the attempt to validate this nonlinear finite element model is discussed in this chapter. This validation is done based on experimental results of previous studies. Deep beams that were tested in the researches performed by Subedi et al. in 1986 [20] and Jun-Hong Zhang et al. in 2020 [24] are used for the verification. The verification is done by modelling deep beams that are used in the experiments using nonlinear finite element analysis and compare the results to the experimentally obtained results

3.1 Specifications of the FE model

The specifications of the finite element model that will be used in this research are based on the guidelines [10] that were discussed earlier in this report. Also, the FE models of the previous master thesis reports of Sugianto [21] and Bhattarai [6], which were discussed in chapter 2.5.3, were used. The type of elements that will be used and the constitutive relations of the materials are presented in Table 3.1.1 and 3.1.2. The guidelines also specify some values that should be used in the model. These values are presented in Table 3.1.3.

Table 3.1.1: Finite elements and constitutive relations of concrete

Concrete	
Finite Element	
Element Type	Plane Stress Element CQ16M
Interpolation scheme	Quadratic
Integration scheme	Full (2x2 point Gauss)
Constitutive Modelling	
Model	Total strain based rotating crack model
Tensile behavior	Exponential softening
Compressive behavior	parabolic
Crack Bandwidth	Rots
Compressive strength reduction model due to lateral cracking	Vecchio & Collins 1993
Lower bound reduction curve	0.4
Stress confinement model	Selby & Vecchio
Poisson's ratio reduction model	Damage based

Table 3.1.2: Finite element and constitutive relations of reinforcement

Reinforcement	
Finite Element	
Embedded Reinforcement	Yes
Interpolation scheme	quadratic
Integration scheme	Full Integration
Constitutive Modelling	
Material model	Elasto-plastic with hardening

Table 3.1.3: material properties of concrete [10]

Parameter	
Characteristic cylinder compressive strength	f_{ck}
Mean compressive strength	$f_{cm} = f_{ck} + \Delta f$ $\Delta f = 8 \text{ MPa}$
Minimum reduction factor of compressive strength due to lateral cracking	$\beta_{\sigma}^{\min} = 0.4$; $\beta \geq \beta_{\sigma}^{\min}$ (40% of the strength remains)
Lower-bound characteristic tensile strength	$f_{ctk;0.05} = 0.7 f_{ctm}$
Mean tensile strength	$f_{ctm} = 0.3 f_{ck}^{2/3}$ for $\leq \text{C50/60}$ and $f_{ctm} = 2.12 \ln(1 + 0.1 f_{cm})$ for $> \text{C50/60}$
Fracture energy	$G_{Fk} = 0.7 \times 0.073 f_{cm}^{0.18}$
Compressive fracture energy, (Nakamura and Higai, 2001)	$G_{Ck} = 250 \times f_{ck} / f_{cm} \times 0.073 f_{cm}^{0.18}$
Young's modulus after 28 days	$E_{cm} = 22000 (0.1 f_{cm})^{0.3}$
(Initial) Poisson ratio	$\nu = 0.20$
Density plain concrete	$\rho = 2400 \text{ kg/m}^3$
Density reinforced concrete	$\rho = 2500 \text{ kg/m}^3$
Long term effect coefficient \times the reduction factor for the determination of concrete	$\alpha_{cc} k_t = 1.0$

In Table 3.1.3 characteristic values for the fracture energy and the compressive fracture energy are given. In the validation of the model, test results are used. The values of the compressive strength, tensile strength and other values follow from experiments (mean values) and no factors are applied to these values. Also, no safety formats are applied on these models. Therefore, the mean value for the Fracture energies should be used, resulting in:

$$G_F = 0.073 f_{cm}^{0.18} \quad [\text{N/mm}]$$

$$G_C = 250 G_{Fk} \quad [\text{N/mm}]$$

3.2 Experimental research performed by Subedi et al.

3.2.1 Description of the experiment

Thirteen simply supported deep beams were tested by Subedi et al. in 1986 [20]. The beams had a span/depth ratio of either 1, 2 or 3 and the main reinforcement ratios of the beams vary from 0.22 to 1.16 percent. The failure loads are predicted by CIRIA Guide 2 and these values are compared to the actual experimental values in the report. However, the calculation procedure following the CIRIA Guide 2 is intended for beams with a span to depth ratio up to 2 as they are based on a sectional analysis (instead of strut-and-tie model), which makes the theoretical failure loads for the beams with a span to depth ratio of 3 invalid. Three failure modes are reported in the report. Namely flexure, diagonal splitting and local crushing. The beams are tested using a four-point bending test.

The material properties are given as mean values that resulted from tests. The compressive cube strength is given, the Modulus of Elasticity and the tensile strength that resulted from a cylinder splitting test. The cube compressive strength (f_{cu}) should be reduced to the cylindrical compressive strength (f_c) following: $f_c = 0.8 f_{cu}$. For the reinforcement, the yield strength, yield strain and Modulus of Elasticity is given. The beams are made from different mixes, resulting in different material properties for each beam. The material properties for the relevant beams that are discussed in this chapter are presented in Table 3.2.1. The reinforcement properties are presented in Table 3.2.2.

For the verification of the finite element model that is used in this research, the beams that have a span to depth ratio of 3 are modelled. This includes beams 1B1 and 1B2. These beams are chosen as its span to depth ratio is similar to the span to depth ratio that will be used in the wall girders analyses in this report. It also includes the two failure modes that are most common for deep beams, so in this verification it can be validated if the expected failure modes for deep beams will also be acquired from the nonlinear finite element analysis. Difference between the two beams is the amount of reinforcement. The main reinforcement (tension reinforcement) ratios of beam 1B1 and 1B2 are 0.2 % and 0.8 % respectively. The shear reinforcement is identical for both beams: vertical shear reinforcement contains 2 bars with a diameter of 4.75 mm spaced 160 mm from each other. The Horizontal shear reinforcement contains again 2 bars with a 4.75 mm diameter, but now spaced 70 mm from each other. Only for beam 1B2, more reinforcement is located above the support plates and below the loading plates. In Figure 3.2.1 and 3.2.2 half of both beams are presented, in the figures also the amount of reinforcement is specified.

It is also chosen to model beam 1A1. This beam is chosen as the CIRIA Guide 2 calculation of this beam is valid. Hereby the experimentally obtained results and the NLFEA results can also be compared to the theoretical failure load. However, it must be mentioned that this code is in the paper criticized for overpredicting the influence of the depth in its calculation (as it is based on a sectional analysis), resulting in a higher capacity. The shear reinforcement consists of 2 bars with a diameter of 4.75 mm which are spaced 150 mm from each other for the vertical bars and 70 mm from each other for the horizontal bars. The main reinforcement ratio of beam 1A1 is 0.2 %. The beam is presented in Figure 3.2.3.

Table 3.2.1: concrete properties of beam 1B1, 1B2 and 1A1

Specimen	f_{cu} [N/mm ²]	f_c [N/mm ²]	f_t [N/mm ²]	E_c [N/mm ²]
1B1	31	24.8	2.60	17500
1B2	37	29.6	2.75	22500
1A1	32.5	26	3.05	18500

Table 3.2.2: Reinforcement properties [20]

Series	Diameter (mm)	Yield strength f_y or f_{sy} (N/mm ²)	Strain at yield $\times 10^{-6}$	Modulus of elasticity E_s (kN/mm ²)
I	4.75	454	2054	221
	6	331	1615	205
	8	382	2011	190
	12	326	1680	194
	16	493	2221	222
	25	330	1500	220

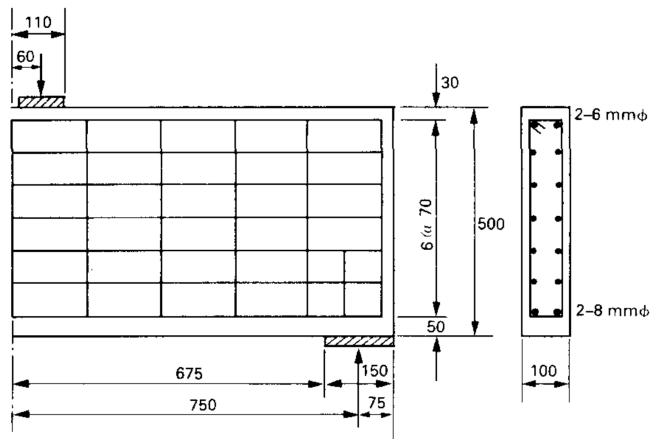


Figure 3.2.1: Beam 1B1 [20]

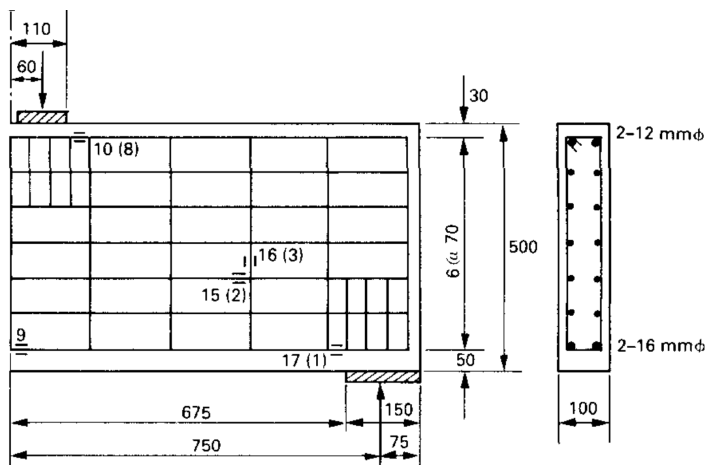


Figure 3.2.2: Beam 1B2 [20]

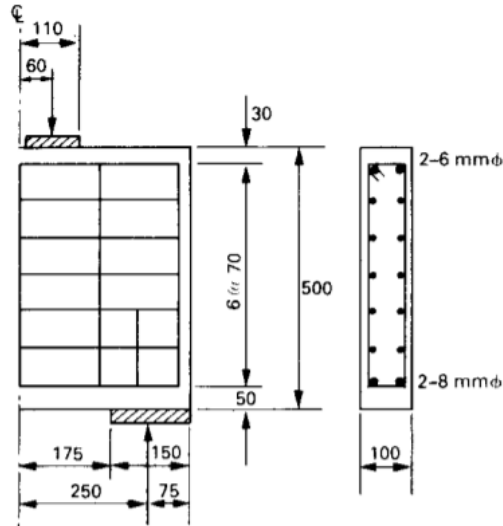


Figure 3.2.3: Beam 1A1 [20]

Various experimental data is given in the report. A table is given in the report where the following values are given for every beam:

- First flexural cracking load
- First diagonal cracking load
- Observed failure mode
- Failure load
- Failure load according to CIRIA Guide 2.

These values can all be compared to what is acquired by the NLFEA. In addition to this, for beam 1B2, a curve is given for the strain of reinforcement versus the applied load. Several curves are observed in the graph, for several positions of the reinforcement. The graph is presented in Figure 3.2.4. The numbers that are indicated in the curves represent the different positions, the same numbers can be found in Figure 3.2.3 where the positions are indicated.

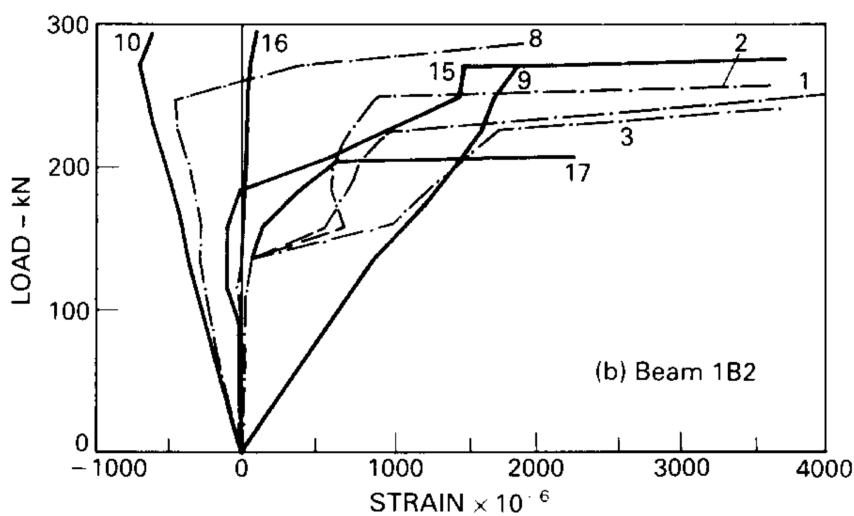


Figure 3.2.4: Load-strain curve for beam 1B2 [20]

3.2.2 Nonlinear finite element model

The constitutive model that is described in chapter 3.2.1 is used in this finite element model. The input variables for the constitutive model of concrete are based on the experimental data, mean values are used in the model. All input variables for the constitutive model of concrete are given in Table 3.2.3 for all three beams. For the reinforcing steel an elasto-plastic material model with hardening is used ($E_{hor} = 0.02 E_s$). The ultimate tensile strength of the reinforcement bars is not given in the paper, neither is the ultimate strain. The ultimate tensile strength of all reinforcement bars is assumed to be equal to 1.25 times the yield strength. The constitutive model for the reinforcement bars with a 6 mm diameter is presented in Figure 3.2.5.

Table 3.2.3: Input parameters for the constitutive model of concrete for all three beams tested by Subedi et al.

Constitutive model of Concrete				
	Beam 1B1	Beam 1B2	Beam 1A1	
Linear material properties				
Young's Modulus	17500	22500	18500	N/mm ²
Poisson's ratio	0.2	0.2	0.2	
Mass density	2400	2400	2400	kg/m ³
Tensile behaviour				
Tensile strength	2.6	2.75	3.05	N/mm ²
Mode-I tensile fracture energy	0.130	0.134	0.13	N/mm
Residual tensile strength	0	0	0	N/mm ²
Compressive behaviour				
Compressive strength	24.8	29.6	26	N/mm ²
Compressive fracture energy	32.53	33.58	32.81	N/mm
Residual compressive strength	0	0	0	N/mm ²
Lower bound reduction curve	0.4	0.4	0.4	

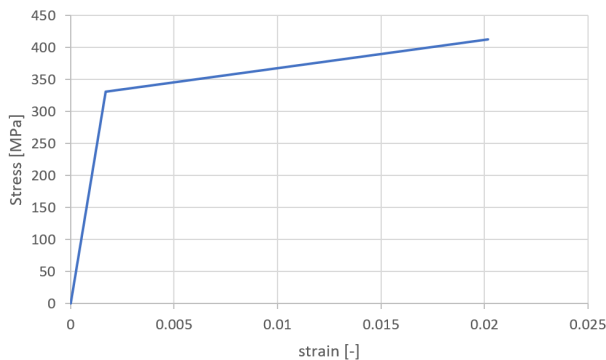


Figure 3.2.5: Constitutive model for 6 mm diameter reinforcement bars

The mesh size is determined based on the maximum allowed mesh size that is given by the Dutch Guidelines [10]. This maximum mesh size is specified in the guidelines as:

$$\min\left(\frac{l}{50}, \frac{h}{6}\right)$$

For beams 1B1 and 1B2 this results in a mesh size of 30 mm. for beam 1A1 a mesh size of 10 mm is used. The load is applied using displacement control. A vertical downward displacement is incrementally applied at both loading plates. The full Newton-Raphson method is used with a maximum number of iterations of 50. Convergence norms of energy and forces are used with a tolerance of 0.001 and 0.01 respectively. The geometry of the three models is presented in Figure 3.2.6, 3.2.7 and 3.2.8.

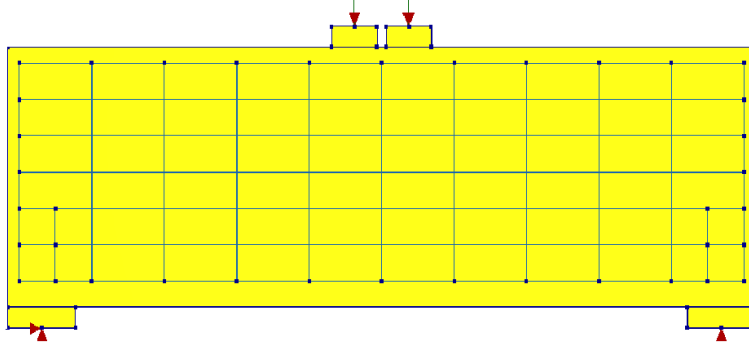


Figure 3.2.6: Geometry of beam 1B1

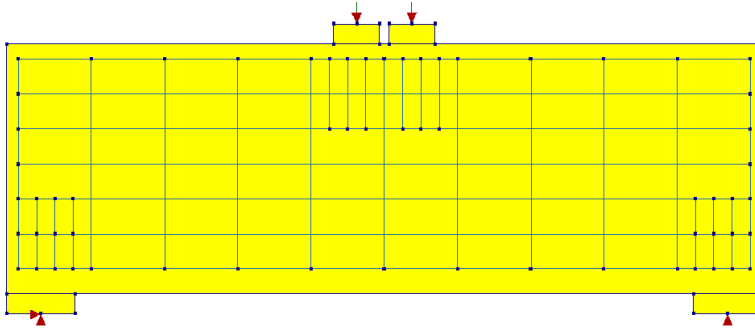


Figure 3.2.7: Geometry of beam 1B2

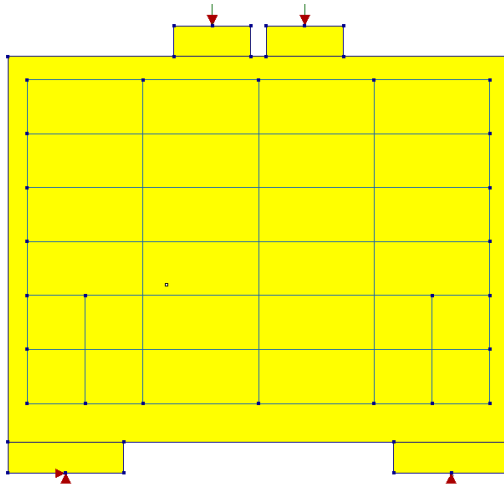


Figure 3.2.8: Geometry of beam 1A1

3.3 Experimental research performed by Zhang et al.

3.3.1 Description of the experiment

Eight simply supported deep beams were tested by Zhang et al. in 2020 [24]. The tests were performed on high strength reinforced concrete deep beams. Goal of the research is to study the effects of shear-span to depth ratio, longitudinal reinforcement ratio and vertical stirrup ratio. The beams all have the same dimension: $l \times b \times h = 1600 \times 200 \times 600$ mm. The loading point is shifted to acquire shear-span to depth ratios of 0.3, 0.6 and 0.9. Longitudinal reinforcement ratios of 0.67%, 1.05% and 1.27% are used. The vertical stirrup ratios considered are: 0%, 0.25%, 0.33% and 0.5%. The beams are also calculated theoretically using various codes, one of these codes being the Eurocode 2. The beams are loaded using a four-point bending test.

The material properties are given as mean values that resulted from tests. The compressive cube strength is given, the Modulus of Elasticity and the tensile strength that resulted from a cylinder splitting test. Both the cube compressive strength and the cylindrical compressive strength are given. For the reinforcement, the yield stress, ultimate stress and modulus of elasticity is given for each bar diameter. The beams are made from the same concrete mix and these concrete properties are presented in Table 3.3.1. The properties of the reinforcement steel are given in Table 3.3.2.

Three of the eight beams from this experiment are modelled to verify the nonlinear finite element model. The considered beams are referred to in the research as beam MDB-2, MDB-3 and beam MBD-4. All three beams have a vertical web reinforcement ratio of 0.33%, a horizontal web reinforcement ratio of 0.33%. Beam MBD-3 has a shear span to depth ratio of 0.9, the other two have a shear span to depth ratio of 0.6. Beam MBD-2 and MBD-3 have a longitudinal reinforcement ratio of 1.05% while beam MBD-4 has a longitudinal reinforcement ratio of 0.67%. The vertical web reinforcement of the beams consists of 8 mm diameter bars, spaced 150 mm from each other. The longitudinal reinforcement is present in 2 layers of 2 bars. The beams are presented in Figure 3.3.1, 3.3.2 and 3.3.3.

Table 3.3.1: concrete properties [24]

f_{cu}/MPa	f_c/MPa	f_t/MPa	E_c/GPa
59.8	42.9	3.75	34.6

Table 3.3.2: Reinforcing steel properties [24]

Reinforcement	d/mm	f_y/MPa	f_u/MPa	E_s/GPa
HTRB600	16	670	865	198.5
HTRB600	20	653.7	823.3	196.6
HTRB600	22	630	800	195.8
HRB400E	8	456.8	647.7	205.3

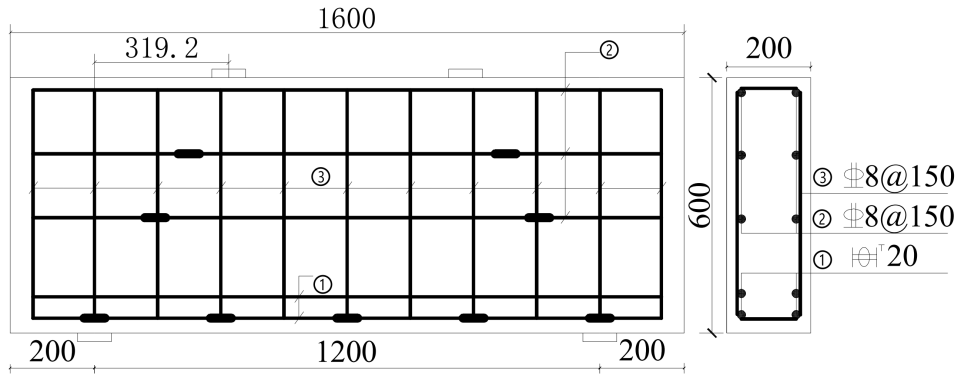


Figure 3.3.1: Beam MDB-2 [24]

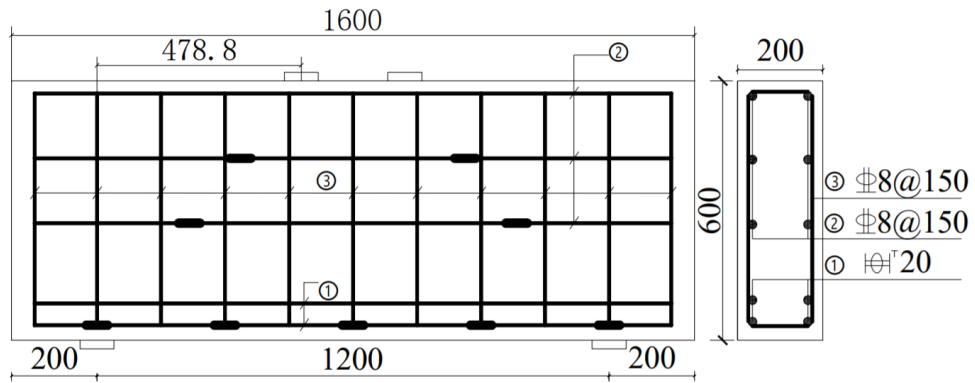


Figure 3.3.2: Beam MDB-3 [24]

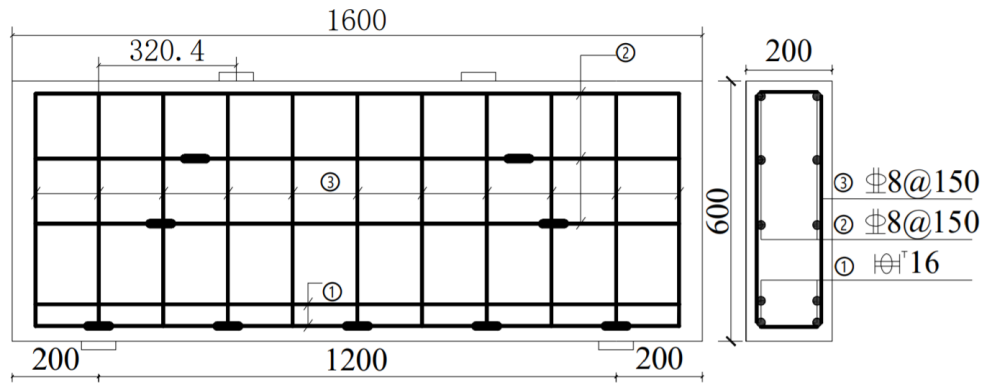


Figure 3.3.3: Beam MDB-4 [24]

3.3.2 Nonlinear finite element model

The constitutive model that is described in chapter 3.2.1 is used in this finite element model. The input variables for the constitutive model of concrete are based on the experimental data, mean values are used in the model. All input variables for the constitutive model of concrete are given in Table 3.2.3 for all three beams. For the reinforcing steel an elasto-plastic material model with hardening is used. The hardening modulus is chosen at $E_{har} = 0.02 E_s$. The ultimate tensile strength of the reinforcement bars is given in the paper, the strain is calculated using the assumed hardening modulus.

Table 3.3.3: Input parameters for the constitutive model of concrete of the beams tested by Zhang et al.

Concrete		
Linear material properties		
Young's Modulus	34600	N/mm ²
Poisson's ratio	0.2	
Mass density	2400	kg/m ³
Tensile behaviour		
Tensile strength	3.75	N/mm ²
Mode-I tensile fracture energy	0.144	N/mm
Residual tensile strength	0	N/mm ²
Compressive behaviour		
Compressive strength	42.9	N/mm ²
Compressive fracture energy	35.901	N/mm
Residual compressive strength	0	N/mm ²
Lower bound reduction curve	0.4	

The mesh size is determined based on the maximum allowed mesh size that is given by the Dutch Guidelines [10]. This maximum mesh size is specified in the guidelines as:

$$\min\left(\frac{l}{50}, \frac{h}{6}\right)$$

This results in a mesh size of 24 mm, the mesh size used in the calculations is 20 mm. The load is applied using displacement control. A vertical downward displacement is incrementally applied at both loading plates. The full Newton-Raphson method is used with a maximum number of iterations of 50. Convergence norms of energy and forces are used with a tolerance of 0.001 and 0.01 respectively. The geometry of the three models is presented in Figure 3.3.4 and 3.3.5.

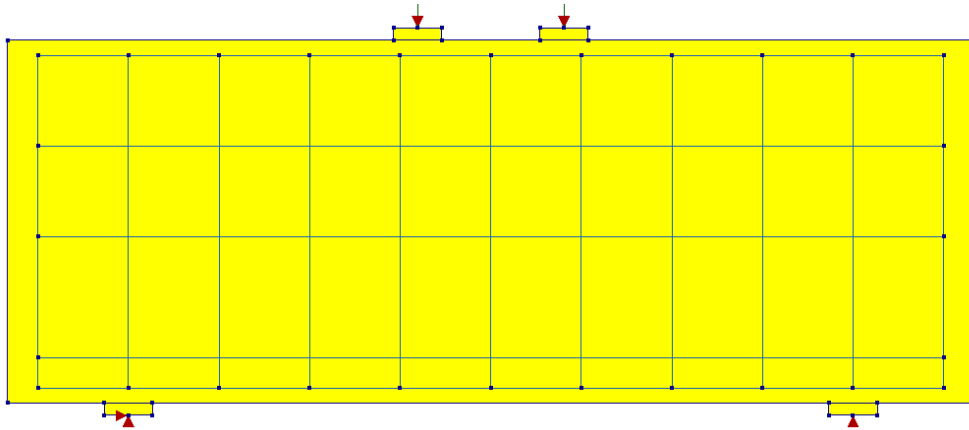


Figure 3.3.4: Geometry of beams MDB-2 and MDB-3

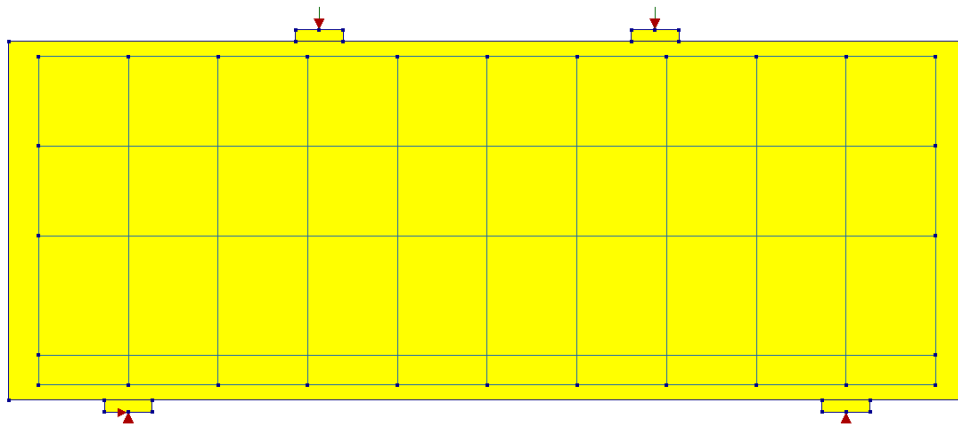


Figure 3.3.5: Geometry of beam MDB-4

3.4 Comparison of results

In this chapter the comparison between the NLFEA results and the experimental results (of the test cases described in chapter 3.2 and 3.3) is made. The comparison will consist of three aspects:

- Comparison of the failure modes
- Comparison of the failure- and cracking loads
- Comparison of the Load-deflection and/or Load-strain curves

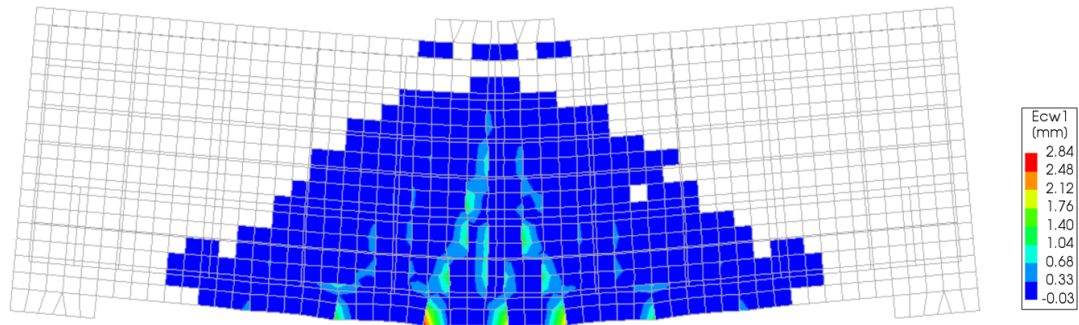
3.4.1 Failure mode comparison

From the six beams that were discussed in this chapter, two failure modes can be distinguished. The deep beam can fail in flexure if no sufficient amount of longitudinal reinforcement is provided, causing a failure in tension at midspan. Due to the fact that the beam is 'deep', the load can (partly) be distributed to the supports directly through the struts. As discussed earlier in this report, a transverse tensile force is generated perpendicular to the struts. This tensile force can be controlled by the web reinforcement. If this reinforcement is not applied sufficiently, the beam will fail in diagonal shear. A diagonal crack is formed from mid-depth extending between the load and the support. This is recognized to be the most common failure mode for deep beams [20]. This failure mode is initiated in a more brittle manner than flexure.

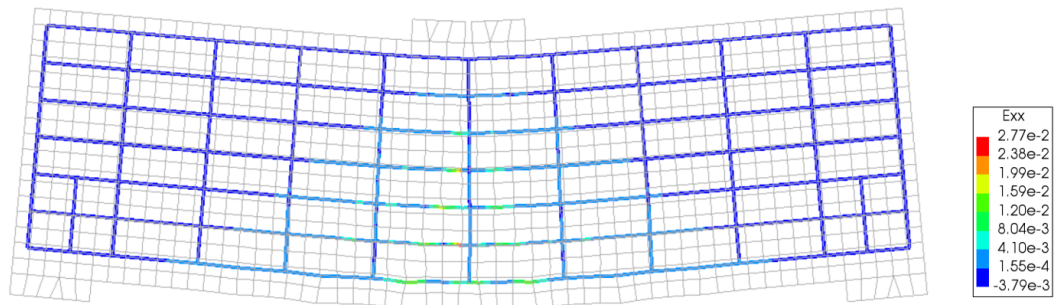
Of the six beams that were modelled in this chapter, two failed in flexure and the other four failed in diagonal splitting. The failure mode that was found in the experiments is, for all six beams, also found by the numerical analysis. The failure mode can be observed from the crack width (E_{cw1}) and the reinforcement strain (E_{xx}) contour plots. These contour plots, including the actual crack pattern that was found experimentally, can be found for all beams in Figure 3.4.1 up to and including 3.4.6. These contour plots are collected from the last converging load-step of each numerical analysis.

Beam 1B1 and 1A1 failed in flexure in the actual experiments. In the numerical analyses of these beams, also a flexural failure mode was observed. This can be seen from the reinforcement strain and the crack width contour plots in Figure 3.4.1 and 3.4.2. The failure mode can be clearly observed from the crack pattern. The cracks are at midspan, indicating a flexural failure. Rupture of the lowest horizontal web reinforcement bars is observed in both beams (at a strain of 2.77×10^{-2}).

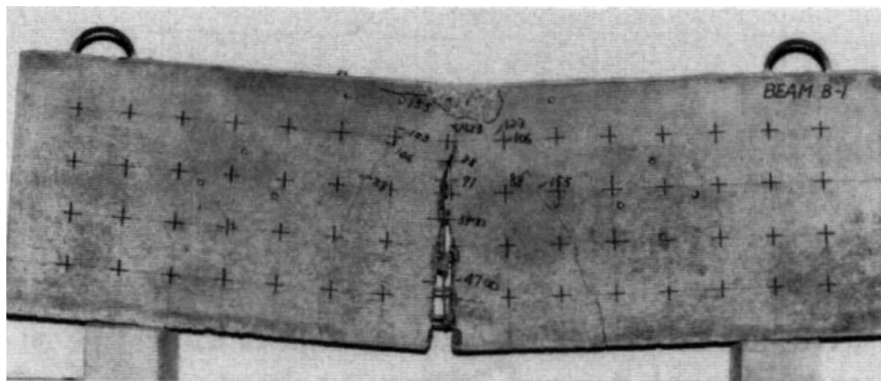
The other four beams fail due to diagonal splitting. This can for all four beams clearly be observed in the crack pattern and reinforcement strain plots. The largest cracks are formed from mid-depth reaching from the load points to the supports. The largest reinforcement strains are also observed in this diagonal section. The reinforcement strain stays for all beams significantly below the rupture strain.



(a) Crack pattern

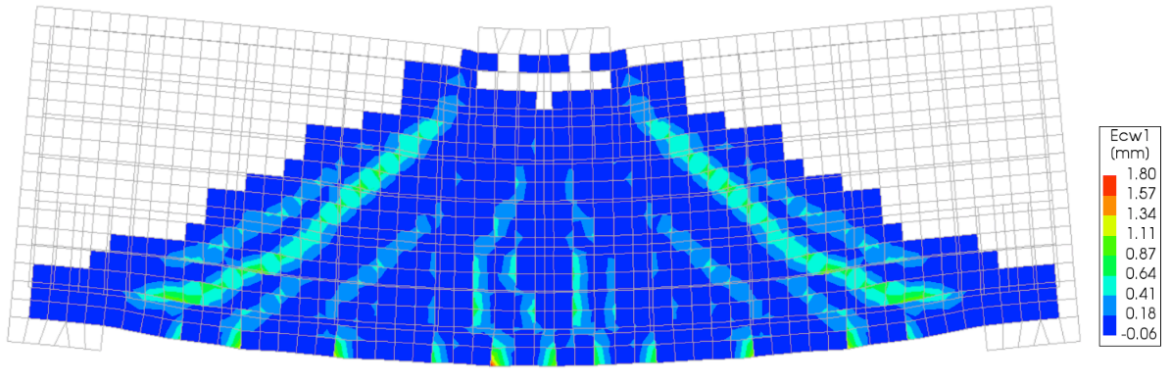


(b) Reinforcement strain in local X-direction

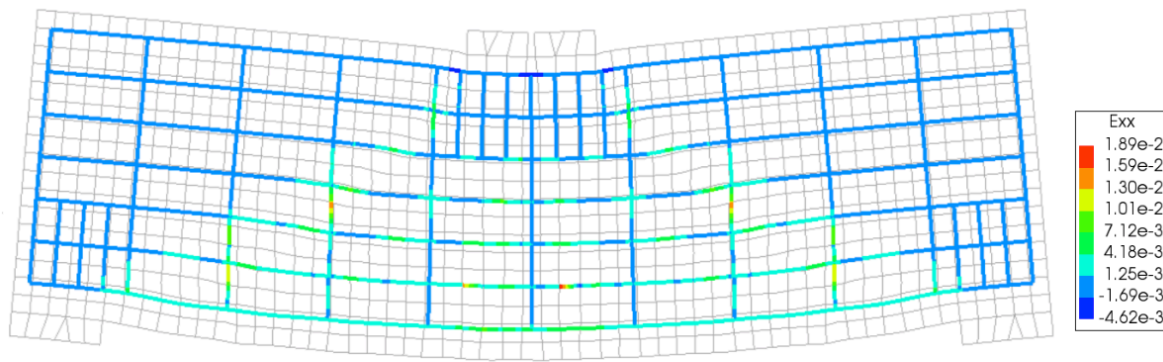


(c) Actual failure [20]

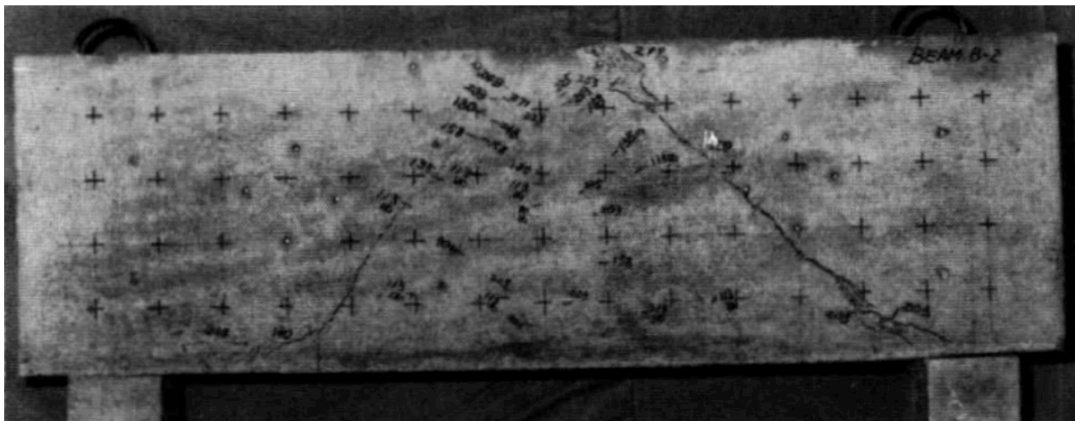
Figure 3.4.1: Numerical results (a, b) and experimental results (c) of the failure mode for beam 1B1 (rupture strain = 2.77×10^{-2})



(a) Crack pattern

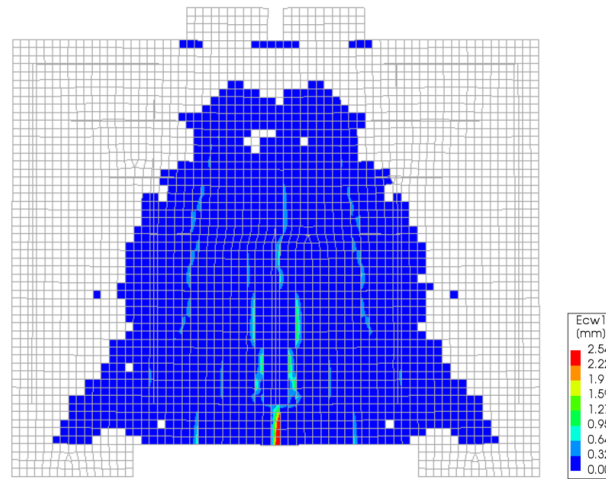


(b) Reinforcement strain in local X-direction

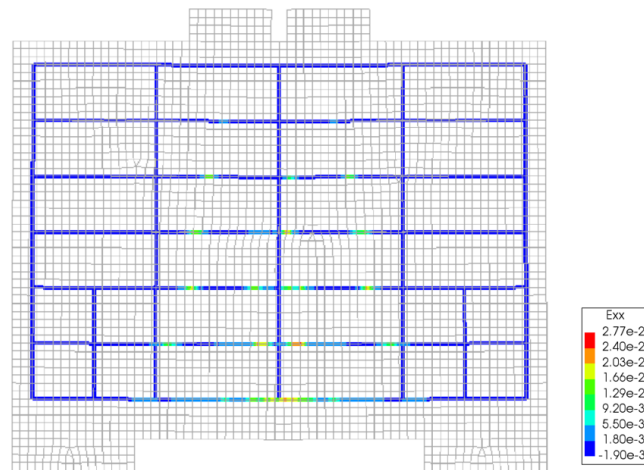


(c) Actual failure [20]

Figure 3.4.2: Numerical results (a, b) and experimental results (c) of the failure mode for beam 1B2



(a) Crack pattern

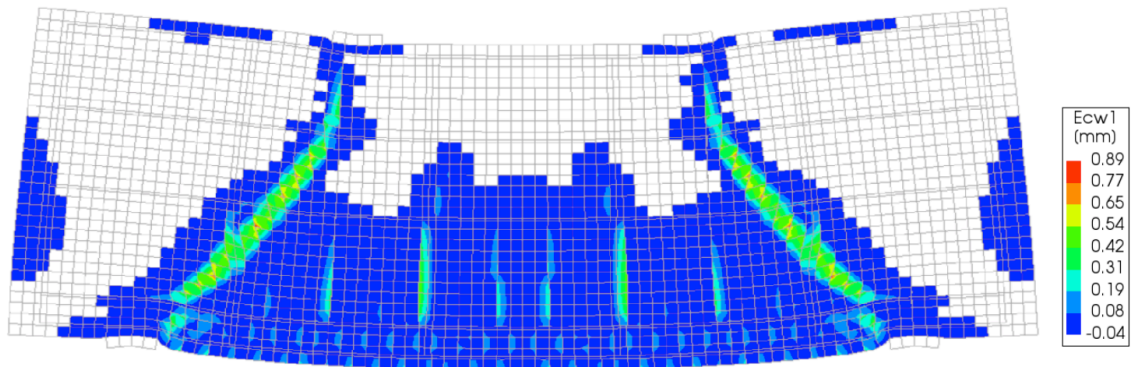


(b) Reinforcement strain in local X-direction

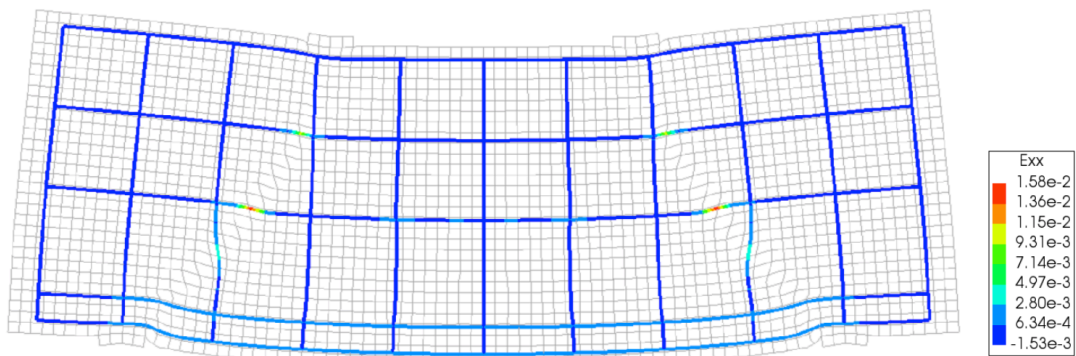


(c) Actual failure [20]

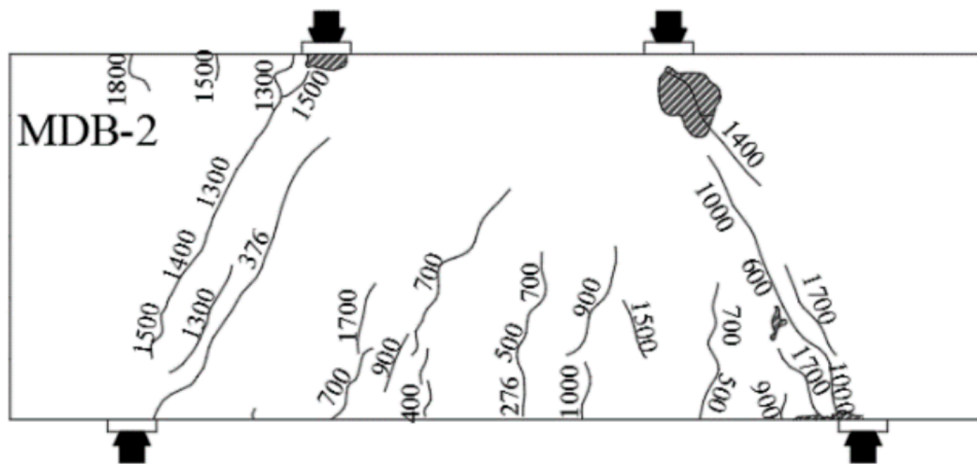
Figure 3.4.3: Numerical results (a, b) and experimental results (c) of the failure mode for beam 1A1 (rupture strain = 2.77×10^{-2})



(a) Crack pattern

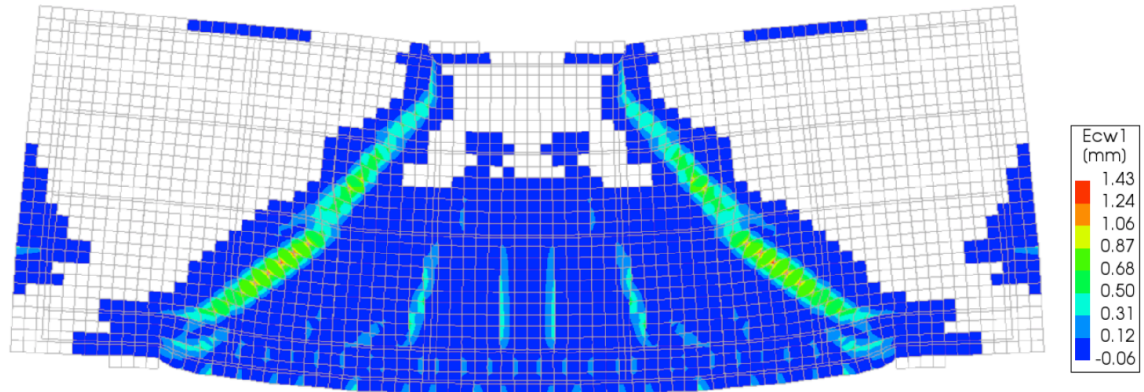


(b) Reinforcement strain in local X-direction

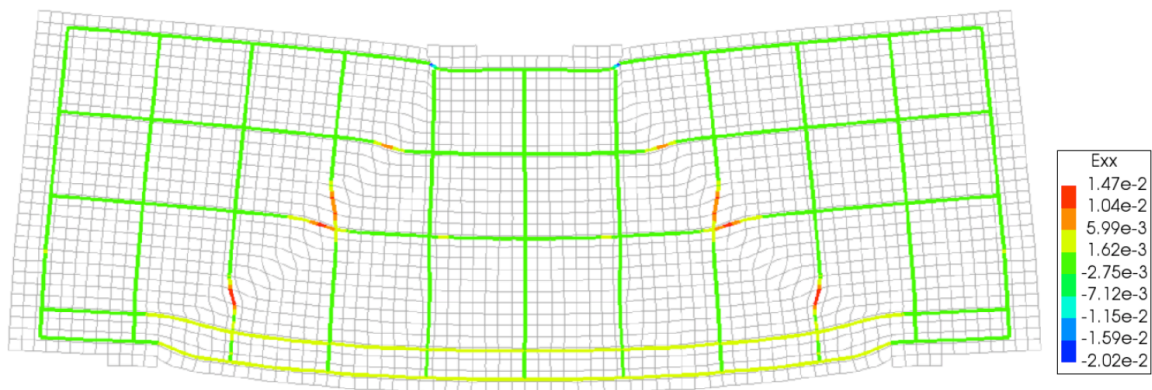


(c) Actual failure [24]

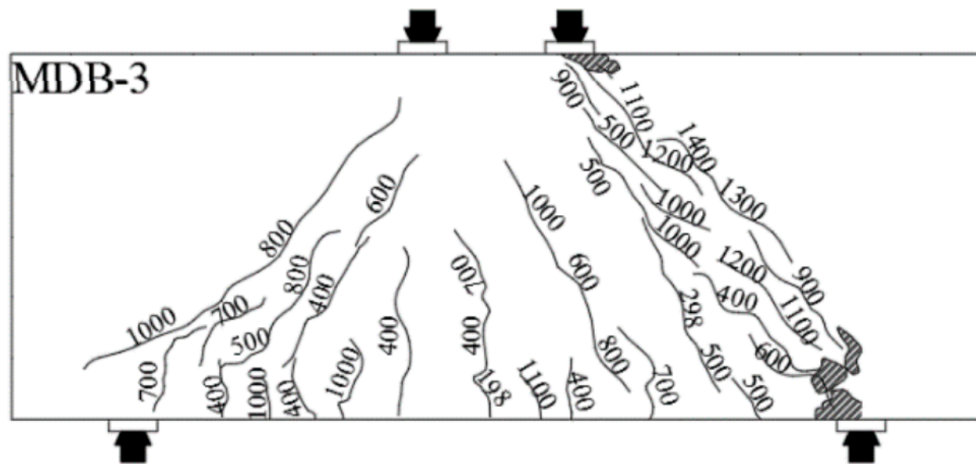
Figure 3.4.4: Numerical results (a, b) and experimental results (c) of the failure mode for beam MDB-2



(a) Crack pattern

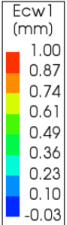


(b) Reinforcement strain in local X-direction

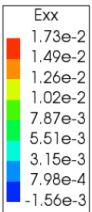


(c) Actual failure [24]

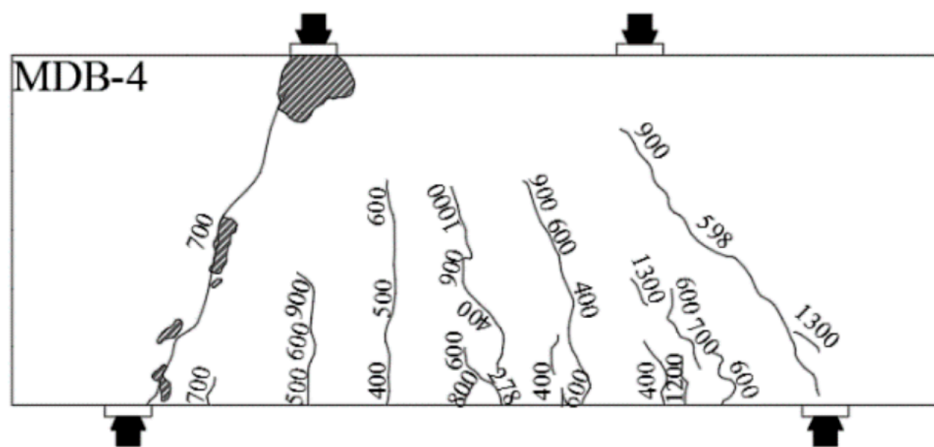
Figure 3.4.5: Numerical results (a, b) and experimental results (c) of the failure mode for beam MDB-3



(a) Crack pattern



(b) Reinforcement strain in local X-direction



(c) Actual failure [24]

Figure 3.4.6: Numerical results (a, b) and experimental results (c) of the failure mode for beam MDB-4

3.4.2 Comparison of failure- and cracking loads

For all numerical analyses that are made in this chapter, a failure load is generated that is at a similar load level as the actual failure load of the specimens. It can be observed that the numerical analyses provide a conservative approach with respect to the experiments, as all experimentally obtained loads are higher than the numerical ones. Only for beam 1B2 an equal ultimate capacity is obtained. This is further discussed in chapter 3.4.3.

The results obtained from the experiments of Zhang et al. [24] are very useful for this research. The specimens were also computed analytically by making use of the strut-and-tie calculation of the Eurocode 2. From these three beams it can be seen that through this numerical analysis a failure load is obtained, that is conservative with respect to the experimental failure load, but at the same time a better approach than the load that is obtained by the Eurocode 2 calculation.

From Table 3.4.2 it can be observed that the cracking loads are significantly higher for the numerical analyses compared to the experiments. This can be explained by the fact that in the numerical model a 'perfect concrete' cross-section is assumed. In reality there are always small microcracks (imperfections) in the concrete, causing the earlier cracking in the experimental results.

Table 3.4.1: Comparison of the failure loads

Experiment	Specimen	Experimental Load [kN]	Numerical Load [kN]	R_{exp}/R_{num}	Analytical Load (EC2) [kN]	Analytical Load (CIRIA) [kN]	$R_{exp}/R_{analytical}$
Subedi	1B1	156	113.5	1.37	-	-	-
Subedi	1B2	299	298.7	1	-	-	-
Subedi	1A1	479	423.3	1.13	-	454	1.06
Zhang	MDB-2	903.5	731.6	1.23	502.40	-	1.80
Zhang	MDB-3	785.0	606.6	1.29	455.08	-	1.72
Zhang	MDB-4	750.0	674.5	1.11	494.69	-	1.52

Table 3.4.2: Comparison of cracking loads

Experiment	Specimen	Flexural cracking load [kN]			Diagonal cracking load [kN]		
		Experimental	numerical	Num/Exp	Experimental	Numerical	Num/Exp
Subedi	1B1	47	75.4	1.60	-	-	-
Subedi	1B2	68	134.7	1.98	158	177.5	1.12
Subedi	1A1	193	344.7	1.79	323	403.6	1.25
Zhang	MDB-2	138	423.8	3.07	188	415.9	2.21
Zhang	MDB-3	99	360.3	3.64	149	360.3	2.42
Zhang	MDB-4	139	402.4	2.89	299	402.4	1.35

3.4.3 Load-deflection curve and Load-strain curve comparison

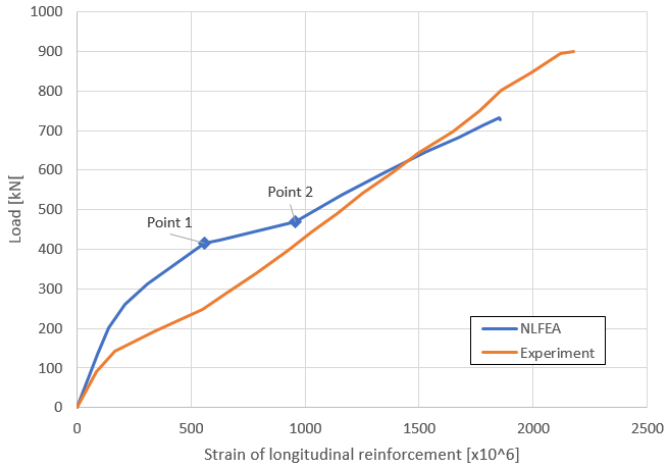
For the experiments of Zhang et al. [24] both a Load-deflection (L-D) curve and a Load-longitudinal reinforcement strain (L-S) curve is given. These are presented in Figure 3.4.7, 3.4.8 and 3.4.9. The L-S curve for beam 1B2 from the research of Subedi et al. is presented in Figure 3.4.10.

For all three load-deflection curves, a few things stand out. Most obvious is that less displacement is obtained by the numerical analyses. The initial stiffness of the response is higher for the numerical analysis. And as discussed earlier, the cracking load is reached at a higher load than in the experiments. After the diagonal cracking load is reached, first a decrease in stiffness is obtained from the results. The cracking load is indicated in the plots as point 1, the decreased stiffness holds on to point 2 in the graphs which is the next load step for model MDB-3 and MDB-4. After point 2 the stiffness obtained by the numerical analysis is similar to the stiffness obtained in the experiments (load-deflection curves approximately parallel). For model MDB-3 and MDB-4 an additional 'kink' in the load deflection curve is observed, this is denoted in the curve as point 3. This 'kink' is observed due to formation of additional cracks in the beams.

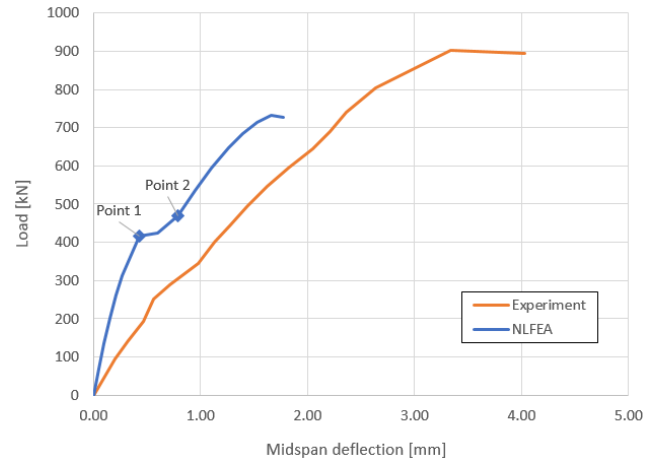
Modelling the reinforcement of the structure as embedded rebars might result in an underestimation of the deformation of the model. By neglecting the fact that the reinforcement can slip in the concrete, which was done in this numerical model, contributions to the total deformation due to local deformation caused by each slip are not accounted for.

From the L-S curve of the experiments performed by Zhang et al. also a few differences can be observed in all three curves. Initially the strain response is similar, up to about a 100 kN load for all specimens. After this, the strain increases significantly more in the experiments compared to the numerical results. This might be the result of earlier cracking in the experiments and due to slipping of the reinforcement. After the cracking load is reached in the numerical analyses, an increase in load results in a larger increase of strain compared to the experiment. This can be observed in the curves by the steeper slope of the curve from the experiment in the last stage.

In Figure 3.4.10, the L-S curve for beam 1B2 is presented. In this curve it is again observed that the strain initially is higher for the experimental analysis. This might again be due to the earlier cracking and the slipping of reinforcement. Most significant difference in this curve is the yielding of the reinforcement. The reinforcement yields at a higher load- and strain level for the numerical analysis compared to the experimental analysis. From the numerical analysis the yield strain can be observed as 0.0022. This is also the yield strain that is given in the paper. However, the strain curve that is obtained from the experiment suggests a yield strain of about 0.0019. It seems that the yield strain of this bar that is given in the paper, differs from the actual yield strain that is obtained during the experiment. This might also declare why the numerical failure load of this beam is much closer to the actual failure load obtained in the experiments, compared to the other beams.

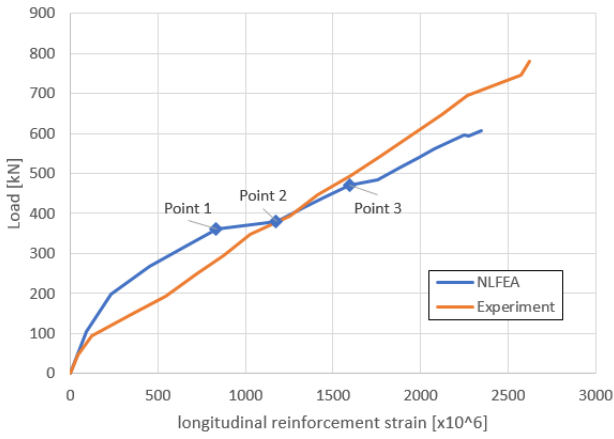


(a) Load-Reinforcement strain curve

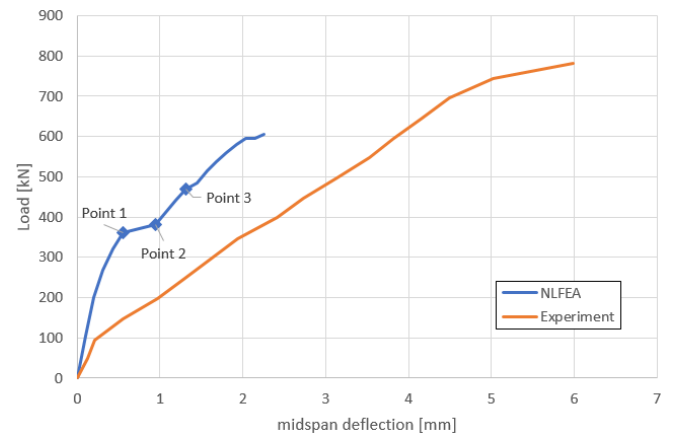


(b) Load-deflection curve

Figure 3.4.7: L-S curve (a) and L-D curve (b) of beam MDB-2

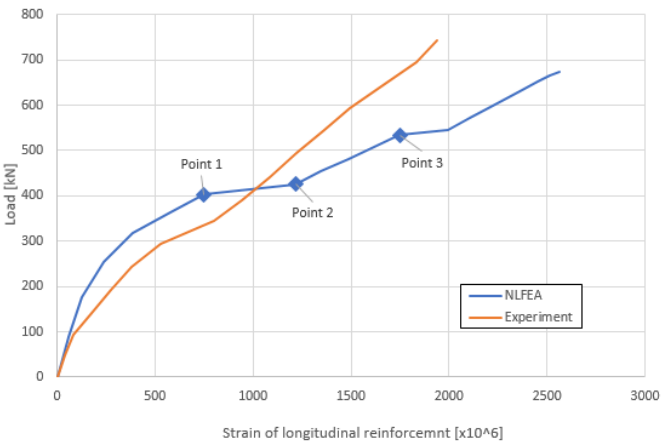


(a) Load-Reinforcement strain curve

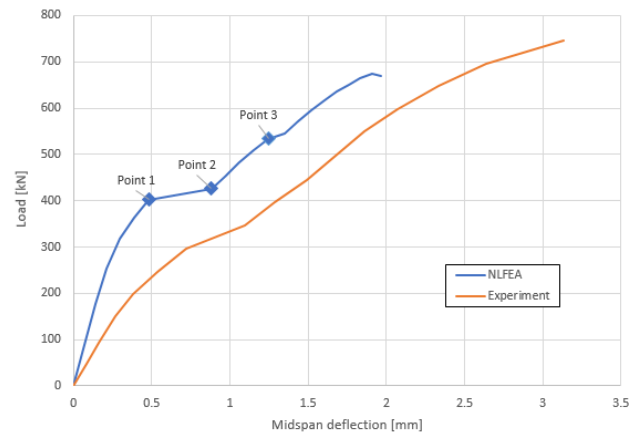


(b) Load-deflection curve

Figure 3.4.8: L-S curve (a) and L-D curve (b) of beam MDB-3



(a) Load-Reinforcement strain curve



(b) Load-deflection curve

Figure 3.4.9: L-S curve (a) and L-D curve (b) of beam MDB-4

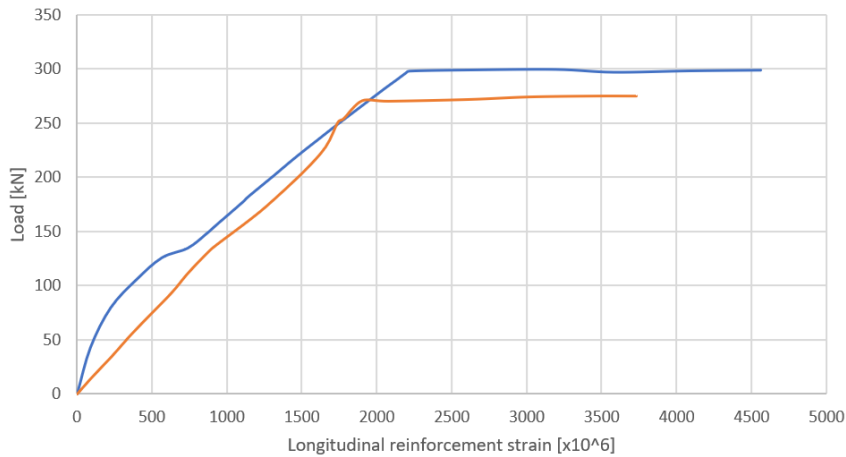


Figure 3.4.10: L-S curve of beam 1B2

3.5 Conclusion

As discussed in this chapter, despite the similarities, also various differences can be observed between the numerical and the experimental results. However, the intention of this verification is not to examine in-depth the differences between the results. The intention is to examine to what extend numerical modelling is suitable to be used in the design of concrete structures.

From the results that are discussed in this chapter, it can be concluded that the numerical analyses underestimate the deformation capacity of the structures. This makes the model not suitable for performing validations with respect to displacement control. However, all numerical models in this chapter proved to correctly model the failure mode that is obtained in experiments. The failure load that is obtained in the numerical analyses is for all beams lower than the experimentally obtained failure load. In addition to this, the failure loads obtained are in between the EC2 analytical failure loads (obtained by use of strut-and-tie model) and the experimentally obtained failure loads. This is exactly what is desired from the numerical analysis for this research. This makes the numerical model, that is described in this chapter, suitable for the analyses that are made in this research.

4 Pile cap analyses

4.1 General overview

In this chapter the analyses for the two-pile caps are discussed. Both a NLFEA and a strut-and-tie model analysis are made. The strut-and-tie model, with the Eurocode verifications, is applied on three different two-pile caps with varying span-to-depth ratio.

In chapter 2.1 the Eurocode verifications, that should be used when the strut and tie model is applied, are discussed. The Eurocode contains verifications for the struts and the nodes (concrete), the ties (main reinforcement) and for the web reinforcement that should be applied for the perpendicular tensile stresses that will be formed in the struts. There are, however, extra conditions that need to be met for the web reinforcement. It is stated in the Eurocode that the web reinforcement for 'deep beams' should at least contain 0.1%. The amount of web reinforcement that is based on this condition can be significantly higher than the amount of web reinforcement that is based on the calculation for the perpendicular tensile force that is formed in the struts. Pile caps have a relatively large width and therefore a large cross-section. Therefore, a higher amount of reinforcement can be obtained with the condition based on the cross-section, than the condition that is actually based on the forces in the structural element.

Analyses in this chapter are performed on three different pile caps. The span of the pile caps is for all three models equal to 1300 mm. This value of the span is based on pile caps that are actually realised. The width and the distance from the centre of the pile cap to its outer edge are also the same for all three models, namely 600 mm and 400 mm respectively. The height of the three pile caps differ for all three models, the height is chosen such that strut angles of 45°, 55° and 65° are obtained. These particular angles are chosen to vary between the total range of the strut angles that is allowed by the Eurocode. In the Eurocode it is stated that for corbels, which is also designed by the strut-and-tie method, the minimum strut angle is 45 ° and the maximum strut angle is 68.1°. The reinforcement is designed for these three models using the Eurocode verifications. These models will subsequently be modelled in DIANA. For each model that is designed by the Eurocode verifications, an alternative reinforcement design will be made. This alternative design differs from the original design by the web reinforcement. The web reinforcement for the alternative design will be based on the force that is formed perpendicular to the struts, and not on the cross section. So, in total six DIANA models will be computed, and three Eurocode analyses will be performed. Aim of designing the alternative models in DIANA, is acquiring a similar capacity with less reinforcement used in the structural element.

Also the verification regarding crack width control will be checked in DIANA. In the Eurocode it is stated that for deep beams an internal lever arm of $z = 0.2 l + 0.4 h \leq 0.6 l$ may be used. This will, for pile caps with relatively large height, result in a lever arm that is much smaller than the lever arm that is acquired by the strut and tie model itself. Using this lever arm results in a larger steel stress in the longitudinal reinforcement. In this analysis the lever arm suggested by this formula is used, it is subsequently checked in the numerical results if this assumption is fair.

Specifications of the models that will be discussed in this chapter are presented in Table 4.1.1 and Table 4.1.2. The heights are calculated to obtain the desired strut angle. Calculation of these heights is presented and further discussed in chapter 4.2.

Table 4.1.1: specifications of the pile caps used for the strut-and-tie model analyses

Model	Span	Depth	Span/effective depth ratio
A	1300 mm	720 mm	2
B	1300 mm	810 mm	1.76
C	1300 mm	925 mm	1.52

Table 4.1.2: Specifications of the pile caps used for the NLFEA

Model	Span	Depth	Span/effective depth ratio	Web reinforcement design
A1	1300 mm	720 mm	2	Eurocode
A2	1300 mm	720 mm	2	Alternative
B1	1300 mm	810 mm	1.76	Eurocode
B2	1300 mm	810 mm	1.76	Alternative
C1	1300 mm	925 mm	1.52	Eurocode
C2	1300 mm	925 mm	1.52	Alternative

4.2 Strut-and-tie model

In this chapter the three different models that are designed with the strut and tie model are discussed. The reinforcement layout is designed by making use of Eurocode calculations. The environmental class of the structural elements designed in this chapter is XC2, and the structural class is S4. C30/37 concrete is used and the design working life is 50 years. The minimum cover on the longitudinal reinforcement can now be calculated using the specifications described above. This results in a minimum cover of 35 mm. A cover of 50 mm will be applied on the longitudinal reinforcement of all the models that are analysed in this chapter.

Longitudinal reinforcement bars with a diameter of 20 mm are used and stirrups with a bar diameter of 10 mm are used. This sets the level of the reinforcement bars at:

$$h - d = c + \phi_{st} + \frac{1}{2}\phi_l = 50 + 10 + 10 = 70 \text{ mm}$$

Where:

- c is the cover on the reinforcement.
- ϕ_{st} is the diameter of the stirrups.
- ϕ_l is the diameter of the longitudinal reinforcement bars.

Square piles of 300 x 300 mm are used in the calculations. The column that is used in the calculations is rectangular with dimensions of 400 x 450.

The height that should be used to obtain the desired strut angle can now be calculated using the information that is discussed above. The maximum force that can be applied on the model, and for which the reinforcement of the model subsequently will be designed, can be calculated based on the maximum stresses that can be applied at the nodes. The node under the column is designed such that the stresses on each 'surface' of the node are equal. This is done separately for all three models in this chapter. Also, the resulting reinforcement layout is presented in this chapter.

4.2.1 Model A (strut angle of 45°)

The height of the pile cap for model A should be equal to half the span + 70 mm = 650 + 70 = 720 mm (+ 70 due to position of longitudinal reinforcement) to obtain the desired strut angle of 45°. The strut and tie model of this model, including its dimensions is presented in Figure 4.2.1.

The maximum force that can be applied (and for what the reinforcement can be modelled) on the pile cap can now be determined based on the maximum stresses that can be applied on the nodes. The node under the column is designed such that the stresses are equal on all surfaces. The maximum stress that can be applied on a CCC-node is equal to:

$$\sigma_{RD,max} = k_1 v' f_{cd} = 17.6 \text{ MPa}$$

The maximum force that can be applied on the pile cap, considering the column node, therefore becomes:

$$F_{max} = \sigma_{RD,max} * b_{column} * d_{column} = 3168 \text{ kN}$$

The maximum stress that can be applied on the surfaces of the pile node is lower:

$$\sigma_{RD,max} = k_2 v' f_{cd} = 15 \text{ MPa}$$

The diagonal surface of the node appears to be governing. The maximum force that can be applied on the pile cap is 1950 kN (ULS). The SLS load is assumed to be 1.5 times lower than the ULS Load. This results in a SLS load of 1300 kN for this model, this is used for the crack width calculation.

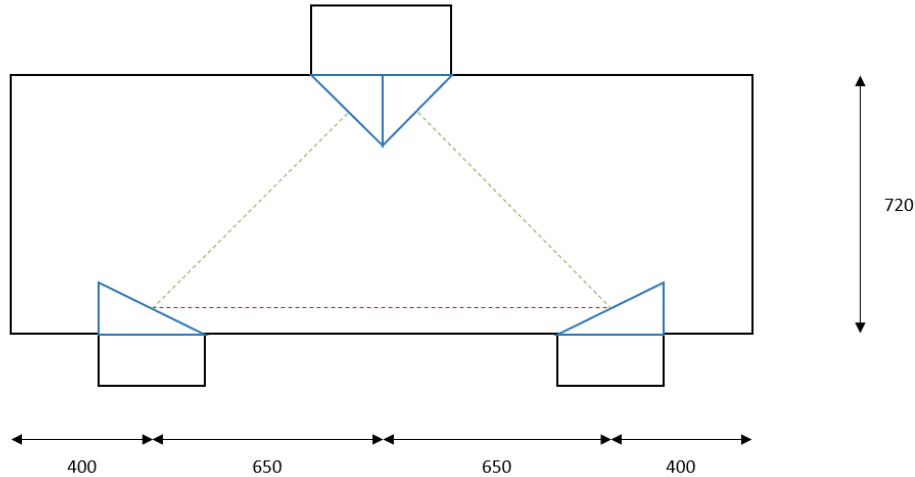


Figure 4.2.1: Strut-and-tie model of pile cap model A

The Eurocode verifications are performed in an excel sheet, the excel sheet for this model can be found in Appendix A1.

Although the structural element is only analyzed in ULS, a SLS calculation is made to design the longitudinal reinforcement regarding crack width. 8 bars with a 20 mm diameter are required for the longitudinal reinforcement. The 10 mm bars web reinforcement should be placed at least every 130 mm, both in vertical and horizontal direction.

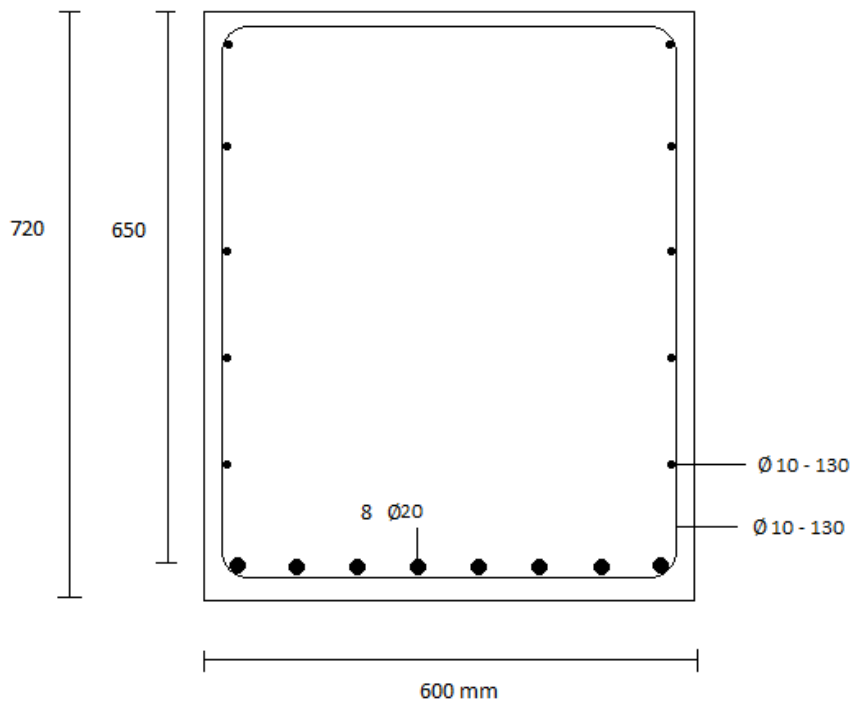


Figure 4.2.2: Reinforcement layout model A

4.2.2 Model B (strut angle of 60°)

The required height of model B is more complicated to calculate, as this contains a strut angle of 60° instead of 45°. This is done in an excel sheet by varying the height until the desired angle is obtained. The angle is calculated in excel as follows:

To obtain equal stresses on all surfaces, the triangle of the node should have relative dimensions to the triangle of the total strut. The width of the column and the effective height (h-70 mm) of the beam are known. By making use of the relations between the triangles and the abc-formula, the vertical dimension of the column node can be expressed as:

$$a_0 = d - \sqrt{d^2 - b_{column}(0.5l - 0.25 * b_{column})}$$

The strut angle can subsequently be calculated as:

$$strut\ angle = \tan^{-1}\left(\frac{d - 0.5a_0}{0.5l - 0.25 b_{column}}\right)$$

This eventually results in a required height of 1080 mm for model B. The maximum force that can be applied on the pile cap is determined in the same way as for model A. Again, the diagonal surface of the pile node appears to be governing. The maximum load that can be applied on pile cap model B is 2450 kN. This results in a 1633 kN SLS load.

The strut and tie model of model B, including its dimensions is presented in Figure 4.2.3.

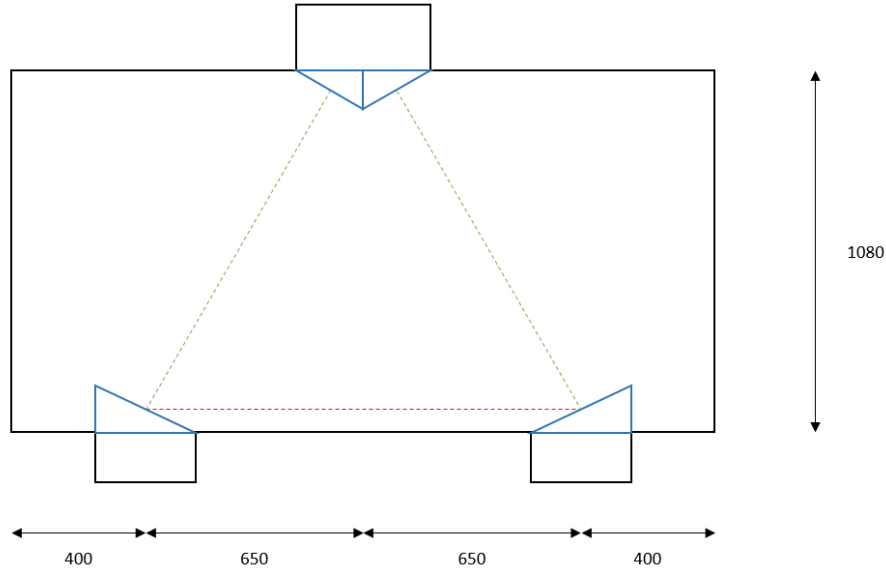


Figure 4.2.3: Strut-and-tie model of pile cap model B

The Eurocode verifications are performed in an excel sheet, the excel sheet for this model can be found in Appendix A2.

7 bars with a 20 mm diameter are required for the longitudinal reinforcement. The 10 mm bars web reinforcement should be placed at least every 130 mm, both in vertical and horizontal direction.

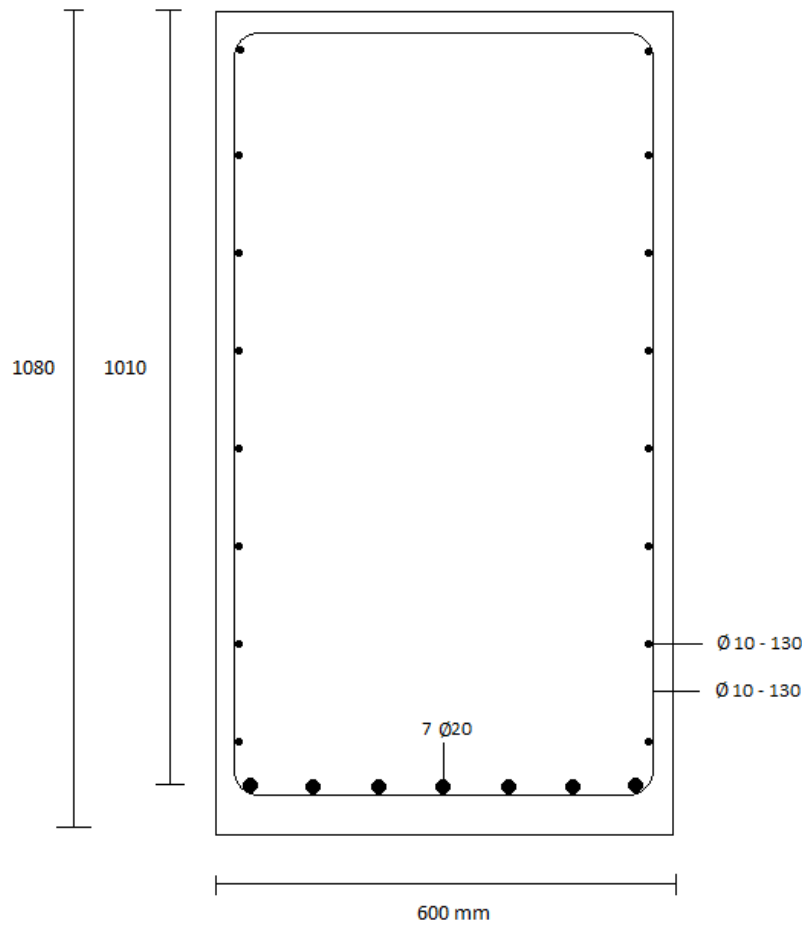


Figure 4.2.4: Reinforcement layout model B

4.2.3 Model C (strut angle of 65°)

The required height of this model is calculated the same way as for model B. To obtain the strut angle of 65° , the total height of the model should be 1300 mm.

The maximum force that can be applied on the pile cap is determined in the same way as for model A. Again, the diagonal surface of the pile node appears to be governing. The maximum load that can be applied on pile cap model C is 2600 kN. This results in a 1733 kN SLS load. The strut and tie model of model C, including its dimensions is presented in Figure 4.2.5.

The Eurocode verifications are performed in an excel sheet, the excel sheet for this model can be found in Appendix A3.

7 bars with a 20 mm diameter are required for the longitudinal reinforcement. The 10 mm bars web reinforcement should be placed at least every 130 mm, both in vertical and horizontal direction.

The same amount of longitudinal reinforcement is applied as model B. It was chosen to use bars of 20 mm for the longitudinal reinforcement. Although a lower reinforcement area is required, 6 bars are not sufficient. A different bar diameter could have been used to optimize the longitudinal reinforcement of model C. However, that is not the essence of this analysis. This analysis focusses on the web reinforcement difference that is discussed in chapter 4.3.

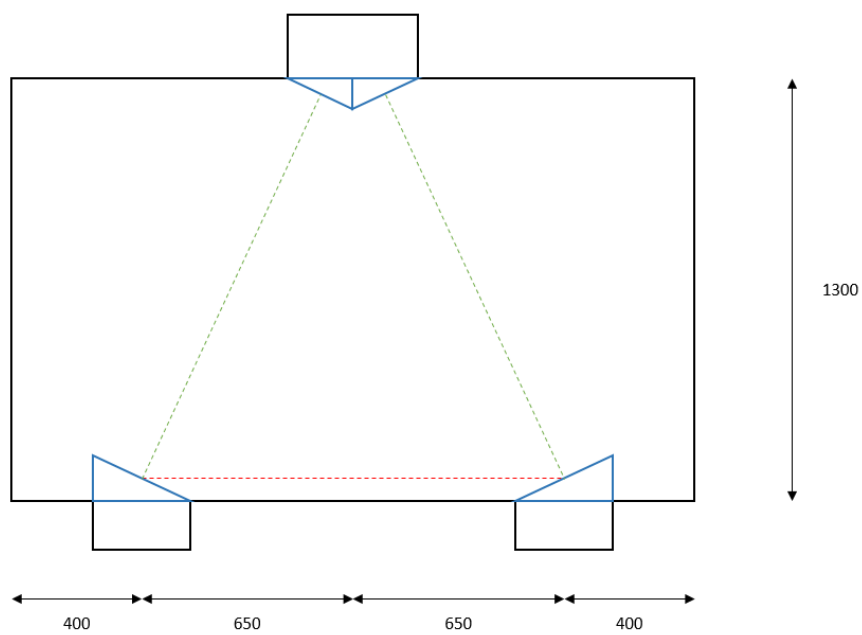


Figure 4.2.5: Strut-and-tie model of pile cap model C

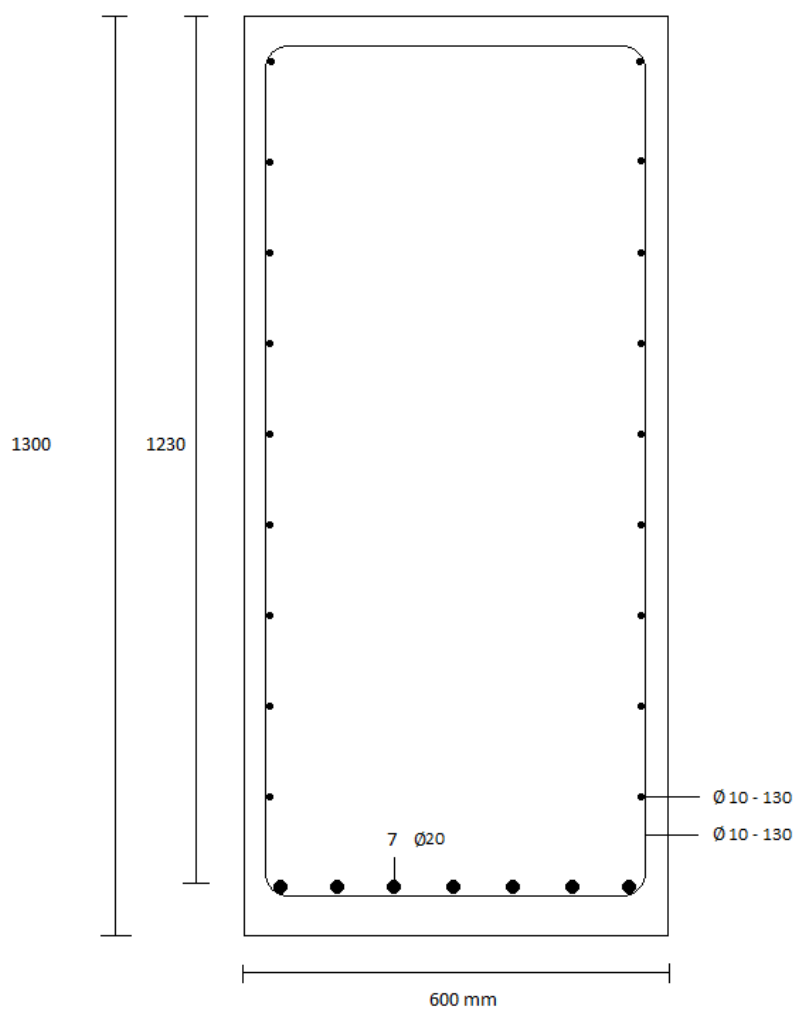


Figure 4.2.6: Reinforcement layout model C

4.3 Finite element models and results

In this chapter, the pile cap models that are used in the numerical analysis of this report are discussed. Six models are computed in DIANA. Three of those models are exactly the same as the models that are described in chapter 4.2 (model A1, B1 and C1). The other three models have an alternative web reinforcement layout. The results that follow from the different models are compared and discussed in chapter 6.

To be able to compare the analytical results (EC2) and the numerical results (DIANA), safety formats are used. The safety formats are already discussed in chapter 2.3.3 of this report.

The Global resistance factor is used for the analyses in this report. The GRF-method uses 'mean' material values. 'Mean' should not be interpreted as the real mean values, but these values are derived from the characteristic values and consider the uncertainty between steel and concrete parameters. The final capacity that results from the numerical computation should subsequently be divided by 1.27 to obtain the design capacity.

The Guidelines give the 'mean' values that should be used. This is presented in Table 4.3.1 and 4.3.2.

Table 4.3.1: concrete properties for the Global Resistance Factor

$f_c [MPa]$	$f_{ct} [MPa]$	$E_c [MPa]$	$G_F \left[\frac{N}{mm} \right]$	$G_C \left[\frac{N}{mm} \right]$
$f_{cm,GRF} = 0.85 f_{ck}$	$f_{ctm,GRF} = 0.7 f_{ctm}$	$E_{ci} = E_{c0} \left(\frac{f_{cm,GRF}}{10} \right)^{\frac{1}{3}}$	$G_F = 0.0073 f_{cm,GRF}^{0.18}$	$G_C = 250 G_F$

Table 4.3.2: Reinforcement properties for the Global Resistance Factor ($A = f_{tm}/f_{ym}$)

$f_y [MPa]$	$f_t [MPa]$	ϵ_y
$f_{ym,GRF} = 1.1 f_{yk}$	$f_{tm,GRF} = A \cdot f_{ym,GRF}$	$\epsilon_{ym,GRF} = f_{ym,GRF} / E_s$

The same concrete strength (C30/37) and the same reinforcement bars (B500) are used for all models. In Figure 4.3.1 the constitutive relation for the reinforcement bars is given, with its relevant values presented in table 4.3.3. In Table 4.3.4 the input variables for the concrete constitutive model are presented.

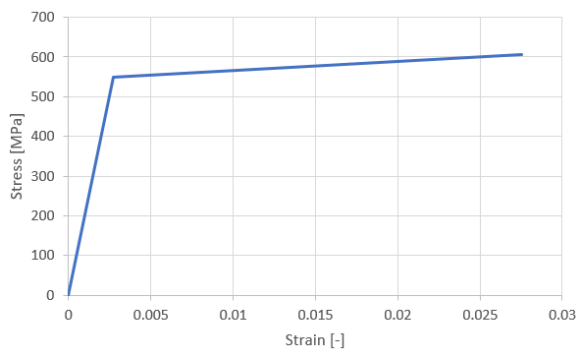


Figure 4.3.1: constitutive relation of the reinforcement bars

Table 4.3.3: Reinforcement properties

Yield stress [MPa]	Ultimate stress [MPa]	Yield strain [-]	Ultimate strain [-]
550	605	0.00275	0.0275

Table 4.3.4: input variables for the constitutive model of concrete in DIANA

Concrete		
Linear material properties		
Young's Modulus	29373.2	N/mm ²
Poisson's ratio	0.2	
Mass density	2400	kg/m ³
Tensile behaviour		
Tensile strength	2.6	N/mm ²
Mode-I tensile fracture energy	0.1308	N/mm
Residual tensile strength	0	N/mm ²
Compressive behaviour		
Compressive strength	25.5	N/mm ²
Compressive fracture energy	32.692	N/mm
Residual compressive strength	0	N/mm ²
Lower bound reduction curve	0.4	

The load is incrementally (50 increments) applied on the pile cap models using displacement control. Energy and force norms are used with a tolerance of 0.001 and 0.01 respectively. The maximum number of iterations is set at 50.

The mesh size is, same as for the beams tested in the verification, based on the maximum allowed mesh size that is given in the Guidelines [10]. This suggests a maximum mesh size of 26 mm. The mesh size is chosen to be 20 mm as this fits better in the model.

The reinforcement design of models A1, B1 and C1 is the same as was already introduced in chapter 4.2. For models A2, B2 and C2 a different web reinforcement design is applied. This different amount of web reinforcement is based on the perpendicular tensile force in the struts, for which a formula is given in the Eurocode. The web reinforcement for the other models is based on a minimal amount of web reinforcement that should be applied for deep beams (based on cross section).

The web reinforcement of model A2 is placed, both vertically and horizontally, every 310 mm at each side of the pile cap.

For model B2 the web reinforcement is, both vertically and horizontally, placed every 300 mm at each side of the pile cap.

For model C2 the web reinforcement is, both vertically and horizontally, placed every 320 mm at each side of the pile cap.

The finite element models that are computed in DIANA are presented in the Figures below.

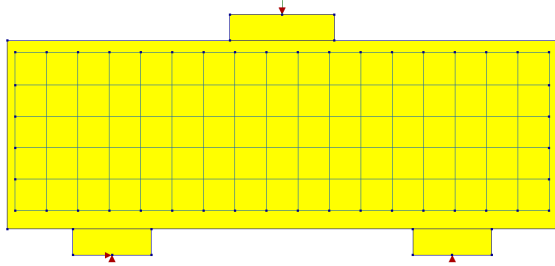


Figure 4.3.2: Finite element model for Pile cap model A1

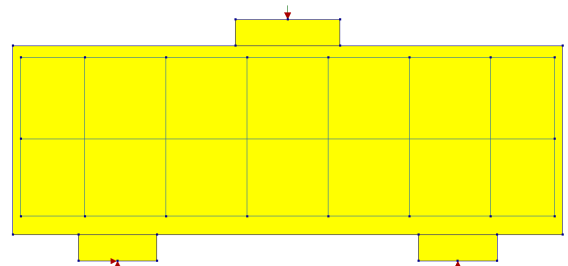


Figure 4.3.3: Finite element model for Pile cap model A2

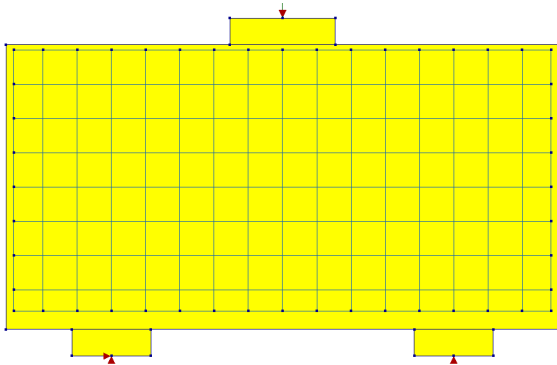


Figure 4.3.4: Finite element model for Pile cap model B1

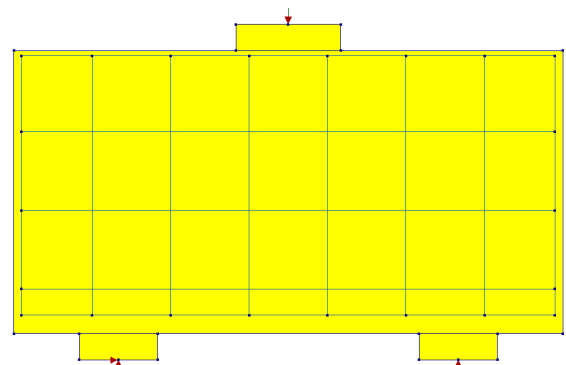


Figure 4.3.5: Finite element model for Pile cap model B2

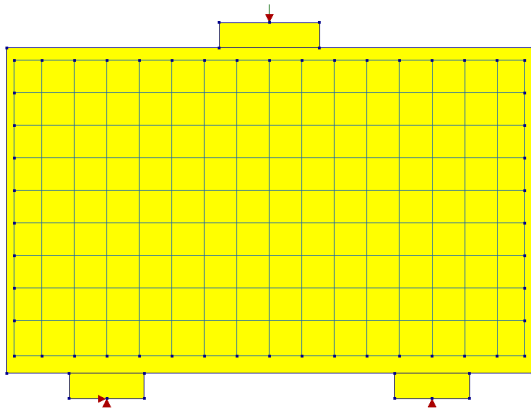


Figure 4.3.6: Finite element model for Pile cap model C1

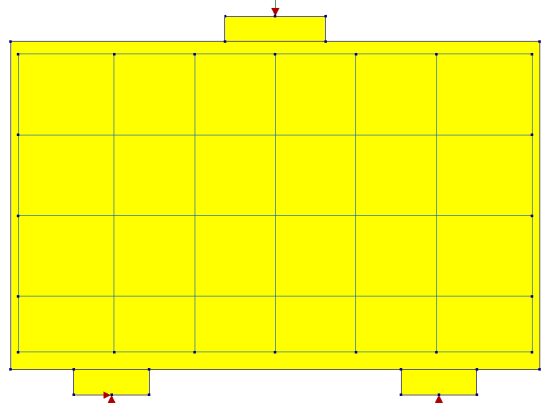


Figure 4.3.7: Finite element model for Pile cap model C2

The load-deflection curves for the models are presented in Figure 4.3.8, 4.3.9 and 4.3.10.

The analytical load and the numerical loads for both reinforcement designs are presented in the plots. The amount of horizontal web reinforcement (ρ_h) is also indicated in the plots. This is determined by dividing the total amount of horizontal reinforcement (bottom reinforcement excluded) by the cross-section area of the pile cap.

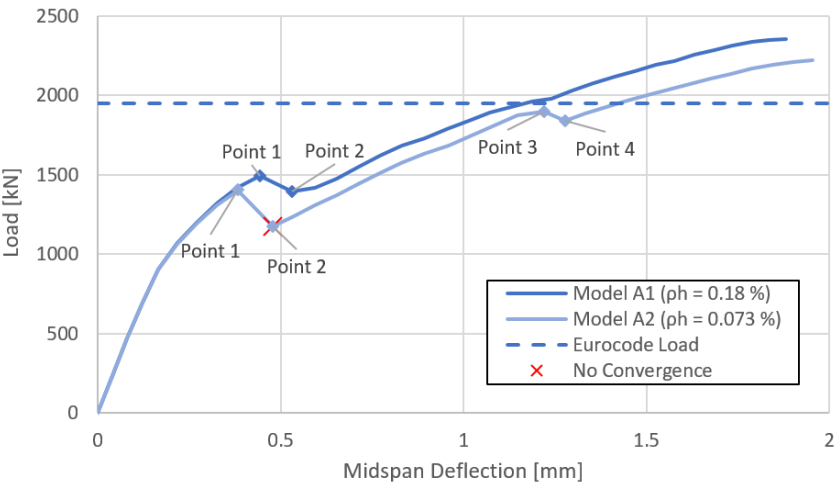


Figure 4.3.8: Load deflection curve of model A1 an A2

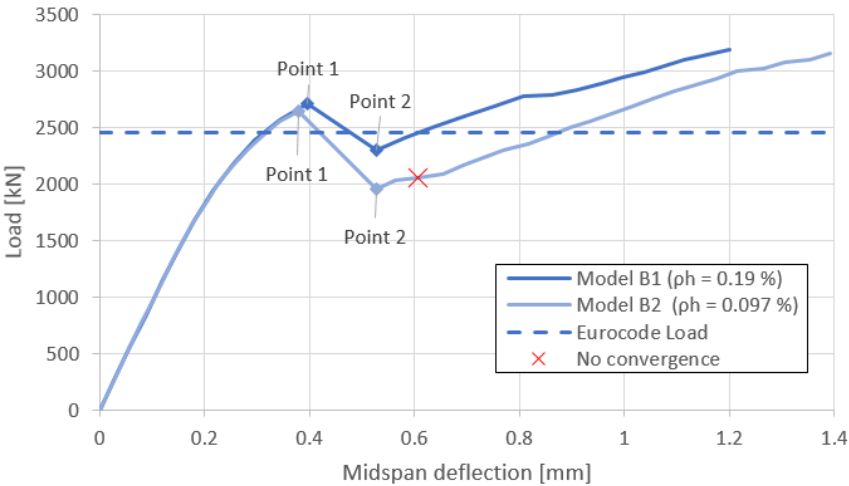


Figure 4.3.9: Load deflection curve of model B1 and B2

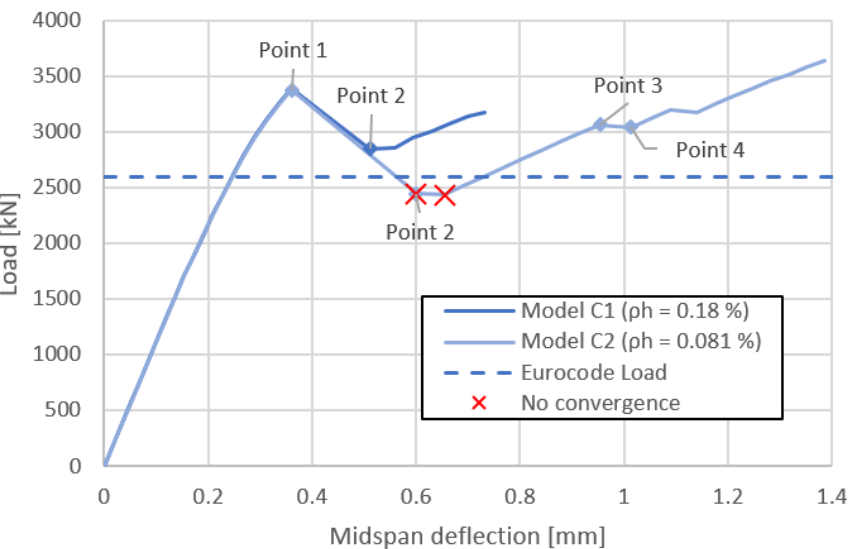


Figure 4.3.10: Load deflection curve of model C1 and C2

All numerical calculations are post-checked by letting the calculation continue if the convergence criteria are not met. Some intermediate load-steps don't show convergence, these steps are indicated in the graphs by the red crosses.

In the graphs it is observed that all models have a higher numerical failure load compared to the analytical failure load. The load-deflection curves look similar for all models. First a linear part is observed, this gradually decays due to cracking of the concrete. Subsequently a sudden decrease in load and high increase in deformation is observed for all models, at this point the diagonal splitting cracks initiate from mid depth of the pile cap. This is indicated in the graphs by point 1. In Figure 4.3.11 the final crack patterns of pile cap models A1, A2, B1 and C1 are presented. The diagonal cracks are observed in this crack pattern, it is also observed that pile cap model A1 contains a significant different crack pattern than model A2. Model A2 shows beside the diagonal cracks, also large vertical crack. These cracks are also initiated at mid-depth of the pile cap. No significant difference in crack pattern between model B1 and B2 is observed, the same holds for model C1 and C2.

After the decrease in load, from point 2 the load increases for all models nearly linearly to the final failure load. For model A2 and C2, a small decrease in load is observed between point 3 and point 4 in the graphs. For model C2, this is the result of rupture of two web reinforcement bars at mid depth located at the diagonal cracks. For model A2 the reason for this small decrease in load is unclear.

The final failure is for all models initiated due to crushing of the concrete at the column node. The concrete stresses at the last load step before final failure are presented for model A1, B1 and C1 in Figure 4.3.12.

A remarkable observation is that model C2 shows a higher maximum load than model C1, despite the more reinforcement of model C1. However, for pile cap models B1, B2, C1 and C2 the diagonal cracking loads can be assumed to be the failure loads, with diagonal splitting as the failure mechanism. This is assumed due to the size of the diagonal cracks and the decrease in load after this point in the Load-deflection curve (from point 1 to point 2).

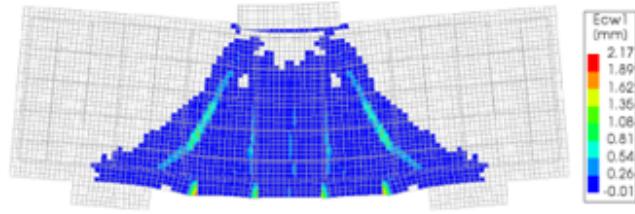
The numerical results for all models are summarized in Table 4.3.5.

Further details of the numerical results are discussed in the discussion chapter of this report. The following plots of each model can be found in Appendix B:

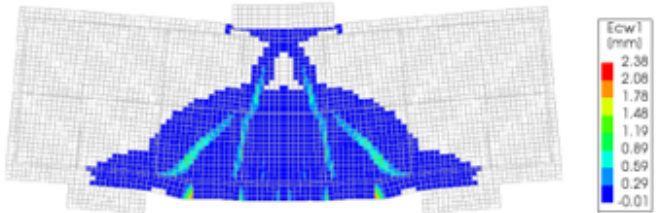
- Principal concrete compressive stresses at last load step before failure
- Reinforcement strains at last load step before failure
- Crack width at last load step before final failure

Table 4.3.5: Numerical results of pile cap models

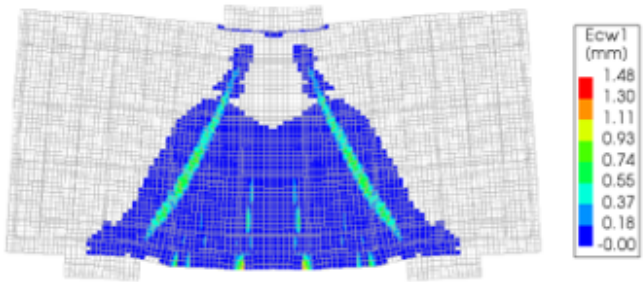
Model	Maximum numerical Load [kN]	Diagonal cracking Load [kN]	Numerical failure Load [kN]	Failure mechanism	Analytical Load [kN]	Horizontal Web reinf. ratio* [%]	Main reinf. ratio [%]	Strut angle [°]
A1	2351.5	1491	2351.5	Crushing under column	1950	0.18	0.58	45
A2	2218.6	1403	2218.6	Crushing under column	1950	0.073	0.58	45
B1	3186.0	2708	2708	Diagonal Splitting	2450	0.19	0.34	60
B2	3154.9	2639	2639	Diagonal Splitting	2450	0.097	0.34	60
C1	3390.6	3391	3391	Diagonal Splitting	2600	0.18	0.28	65
C2	3640.6	3378	3378	Diagonal Splitting	2600	0.081	0.28	65



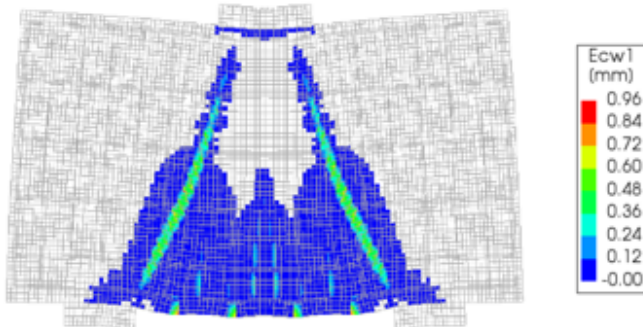
(a) Model A1



(b) Model A2

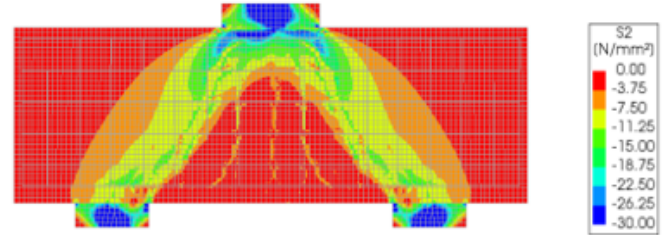


(c) Model B1

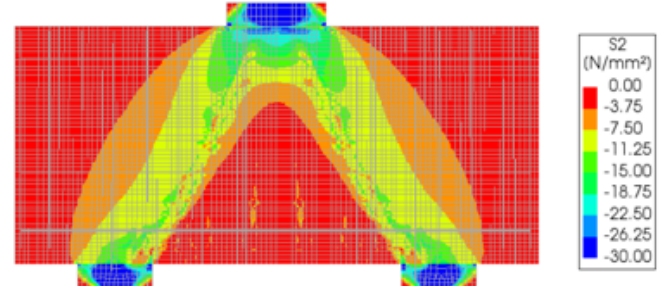


(d) Model C1

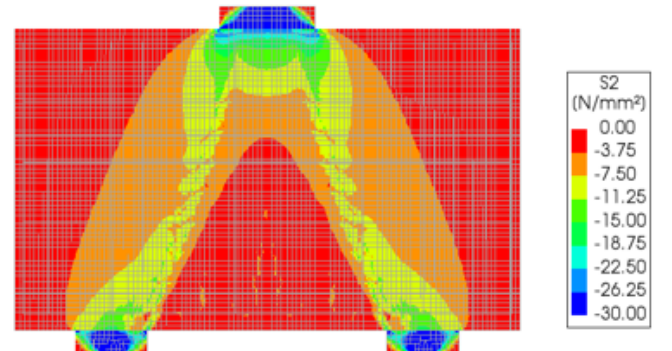
Figure 4.3.11: Crack pattern at failure load for pile cap model A1 (a), A2 (b), B1 (c) and C1 (d)



(a) Model A1



(b) Model B1



(c) Model C1

Figure 4.3.12: Concrete compressive stresses at final load step before failure for pile cap model A1 (a), B1 (b) and C1 (c)

4.4 Conclusion

From the results of the calculations discussed in this chapter, it can be concluded that the numerical failure load appeared to be higher than the analytical failure load for all pile cap models. Two different failure mechanisms are observed. Pile cap models A1 and A2 failed due to crushing of the concrete under the column. The other models failed due to diagonal splitting, large diagonal cracks are formed from mid-depth.

The difference in failure loads between the two reinforcement designs becomes smaller when the span to depth ratio decreases. The same failure mechanism is observed for both reinforcement designs of the models and the load-deflection curve is also similar for both reinforcement designs.

Further differences between the reinforcement designs and differences between the numerical results and the analytical assumptions will be discussed in chapter 6 of this report.

5 Wall girder analyses

5.1 General overview

In this chapter the analyses for the wall girders are discussed. Three models are designed using the strut and tie model and the Eurocode. For these models, two finite element analyses are made. Difference between these models, for the simply supported walls, is the reinforcement detailing above the support, this is further discussed in chapter 5.3. The difference between wall model F1 and F2 is explained and discussed in chapter 5.2.2.

Two of the three models are simply supported wall girders, both with a length of 10 m. One model with a height of 3 m and the other with a height of 6 m. Dimensions are based on dimensions that are used in practice. Supports of 750 mm are used and the thickness of the wall is 250 mm. These wall girders represent walls in apartments of 1 floor (3 m) and 2 floors (6 m) respectively. The strut and tie model and verifications that are used to design the reinforcement in these wall girders is further discussed in chapter 5.2.

Also, a wall girder on 3 supports is analysed. Dimensions of this wall girder are again based on dimensions used in practice. This model represents a wall girder of 1 floor, it has a total length of 10 m and a height of 3 m. An overview of the models is presented in Table 5.1.1 for the strut and tie models and in Table 5.1.2 for the finite element models.

Several things are investigated in the analyses of the wall girders. Similar to the analyses on the pile caps, the dimensions of the nodes are investigated. For the wall girders, nodes are only present above the supports as the wall girders are subjected to a uniformly distributed load. The height of these nodes is in the Eurocode shown to be two times ($h-d$). This is shown in the Eurocode for two layers of bottom reinforcement. However, for the wall girders more layers of bottom reinforcement are required as it is a thin structural element with large loads on it. This will result in a large dimension of the node. It will be checked in DIANA if this way of dimensioning the node is valid.

The detailing of the reinforcement above the supports is analysed. Walls are large structural elements with large loads, this will result in large stresses at the supports. Two finite element analyses are made for each model to study the influence of the reinforcement above the supports.

Table 5.1.1: specifications of the wall girders used for the strut-and-tie model analyses

Model	Length [m]	Height [m]	Number of Supports
D	10	3	2
E	10	6	2
F	10	3	3

Table 5.1.2: specifications of the wall girders used for the numerical analyses

Model	Length [m]	Height [m]	Number of Supports	Extra reinforcement above supports
D1	10	3	2	No
D2	10	3	2	Yes
E1	10	6	2	No
E2	10	6	2	Yes
F1	10	3	3	No
F2	10	3	3	No

5.2 Strut-and-tie-model wall girder

In this chapter the three different wall girder models that are designed with the strut and tie model are discussed. Similar as was introduced for the pile caps: the environmental class of the structural elements designed in this chapter is XC2, and the structural class is S4. C30/37 concrete is used and the design working life is 50 years. Design sheets are made to be able to effectively calculate the wall girder based on the applied reinforcement. This is done separately for the simply supported wall girder models and the continuous wall girder. The calculation procedure of the girders is discussed in chapter 5.2.1 and 5.2.2 respectively.

5.2.1 Simply supported

An example of the strut and tie model that is used for the wall girders is presented in Figure 5.2.1. This is the general model that is used. However, the number of struts that are present in the wall depends on the length and the height of the wall and on the position of the reinforcement. The vertical position of the horizontal ties (presented in red in Figure 5.2.1) is taken as the centre of gravity of the layers of bottom reinforcement and the horizontal struts (presented in blue) is taken as the position of the uppermost reinforcement. The maximum strut angle is set at 68° , based on this maximum angle the number of struts in the wall are determined which results in a strut and tie model as presented in the figure. The distributed load is modelled as equal point loads on each node, subsequently all forces in the model can be calculated. The load that is applied on the models is determined based on the capacity of the nodes above the supports. The calculation procedure of the capacity of these nodes is the same as for the pile caps.

The amount of bottom reinforcement follows from the maximum force in the horizontal tensile ties. This bottom reinforcement can be smeared out over a vertical distance of $0.2 l$. This is not mentioned in the Eurocode, but it is used in previous Dutch codes. As the Eurocode does not mention anything about this distance, this rule is used.

The horizontal web reinforcement follows from the tensile (splitting) force that is present perpendicular to the struts, calculation of this force is already discussed for the pile caps. The vertical web reinforcement follows from this splitting force of the struts in addition to the forces that are present in the vertical ties of the model. These total forces are summed, and the amount of reinforcement needed to resist this force is smeared out over the span of the wall. The Eurocode also provides some extra regulations for the web reinforcement:

$0,002 A_c \leq A_{s,v} \leq 0,04 A_c$ Amount of vertical reinforcement should be between these two values, half of it should be applied at each side.

$A_{s,h} \geq 0,001 A_c$ Amount of horizontal reinforcement should be larger than this value. Recommended value is $A_{s,h} = 0,25 A_{s,v}$.

Maximum spacing between web reinforcement bars should not be greater than 400 mm.

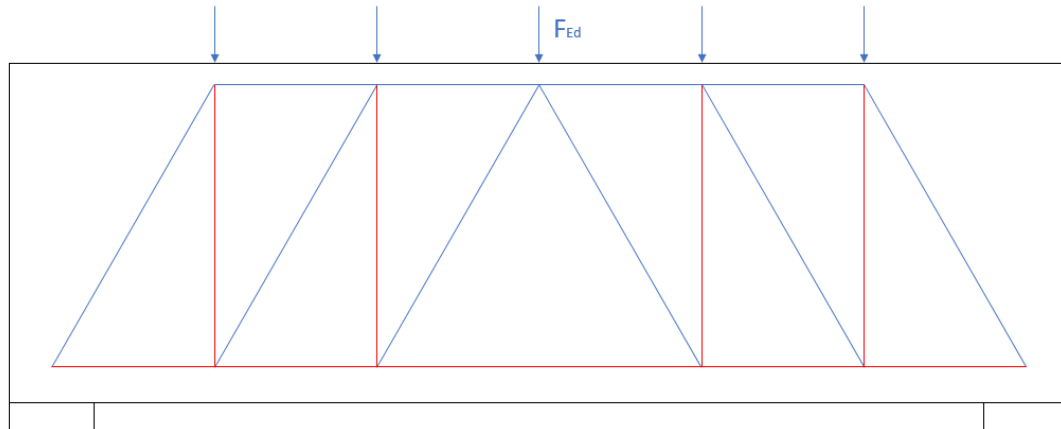


Figure 5.2.1: General strut and tie model for the simply supported wall girder

The excel sheets that are used for the two models are presented in Appendix A4 and A5. Overview of the reinforcement designs are presented in Table 5.2.1 and 5.2.2 for model D and model E respectively. In Figure 5.2.2 and 5.2.3 the reinforcement design is presented for half of the wall girder models (models are symmetric).

Table 5.2.1: Reinforcement design of model D

Model D			
q (ULS)	510 kN/m	q (SLS)	340 kN/m
n		s	
Bottom reinforcement	1 layer 3 x Ø25	100 mm	
	5 layers 2 x Ø25		
Vertical web reinforcement	Ø20	320 mm	
Horizontal web reinforcement	Ø10	320 mm	

Table 5.2.2: Reinforcement design of model E

Model E			
q (ULS)	550 kN/m	q (SLS)	366.667 kN/m
n		s	
Bottom reinforcement	1 layer 3 x Ø25	100 mm	
	5 layers 2 x Ø25		
Vertical web reinforcement	Ø12	370 mm	
Horizontal web reinforcement	Ø8	400 mm	

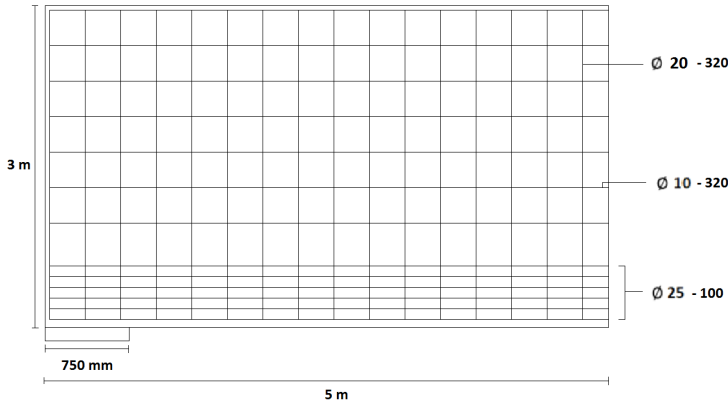


Figure 5.2.2: Reinforcement design of wall girder D

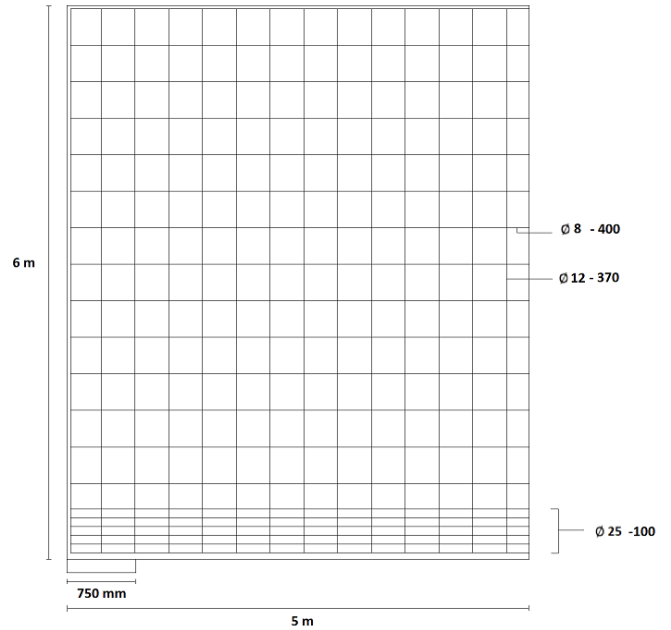


Figure 5.2.3: Reinforcement design of wall girder E

5.2.2 Continuous wall girder on three supports

The strut-and-tie model that is used for the calculation of the continuous wall girder is presented in Figure 5.2.2. From force equilibrium of the model, it follows that there is no force in the upper tensile tie. However, it is assumed that the tensile force in this tie is equal to the tensile force in the bottom tensile tie. The strut-and-tie model is a simplification of the structure and as the wall is continuous, it is known that a tensile force is present above the intermediate support. The diagonal struts are assumed to have an angle of 45° , the vertical position of the upper tensile tie can be determined using the strut angle. The (distributed) load is schematized as 4 equal point loads at a distance of $\frac{1}{3}l$ from each support.

The load follows from the capacity of the nodes. The node of the intermediate support appears to be governing and the maximum distributed load that can be applied is equal to 660 kN/m. The SLS load is set equal to 440 kN/m.

The forces in all struts and ties can subsequently be determined. The amount of longitudinal reinforcement simply follows from the force in the ties. The minimum web reinforcement follows from the perpendicular tensile forces that will result from diagonal splitting of the struts. It appears that this results in such low amount of web reinforcement in vertical direction, that the minimum web reinforcement criterium is governing in vertical direction. These criteria are indicated in chapter 5.2.1

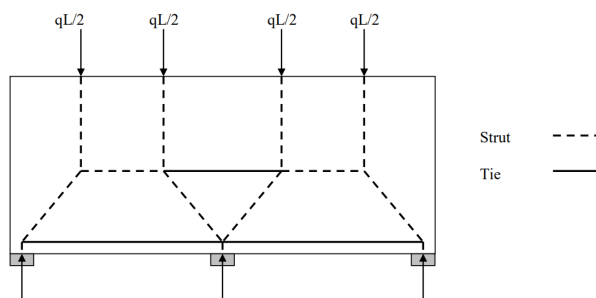


Figure 5.2.4: Strut-and-tie model for continuous wall girders

Two possible ways of designing the reinforcement regarding the upper tensile tie are considered in this report (model F1 and F2). One model contains a few layers of reinforcement at the level at which the upper tie is assumed in the strut and tie model, that can fully take the tensile force. The reinforcement bars are not necessary to extend in the full horizontal distance of the wall, as the tensile force is only present above the intermediate support. The bars extend to a distance of $0.4 l$ on both sides of the support.

For the second model, the force that is assumed in the upper tie is fully taken by the horizontal web reinforcement. The force is in this case, in the calculation, smeared out over the full effective depth of the beam.

The required reinforcement ratio is again calculated using a calculation sheet in excel. This calculation sheet is presented in Appendix A6.

The reinforcement design of wall F1 and F2 is presented in Figure 5.2.3 and 5.2.4 respectively. Half of the walls are presented as they are symmetric. The specifications are presented in Table 5.2.3 and 5.2.4.

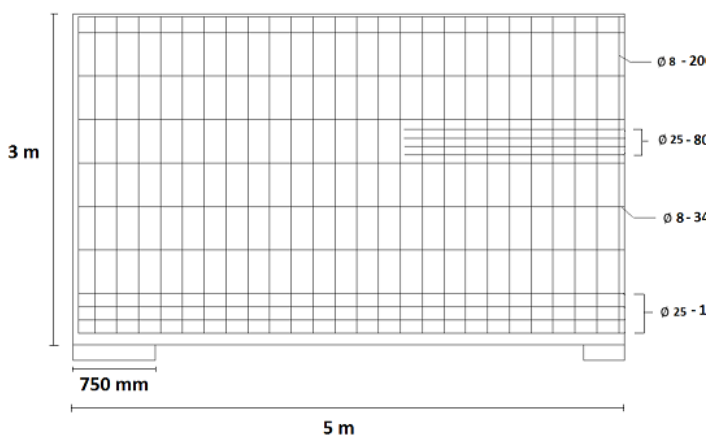


Figure 5.2.5: Reinforcement design of wall girder F1

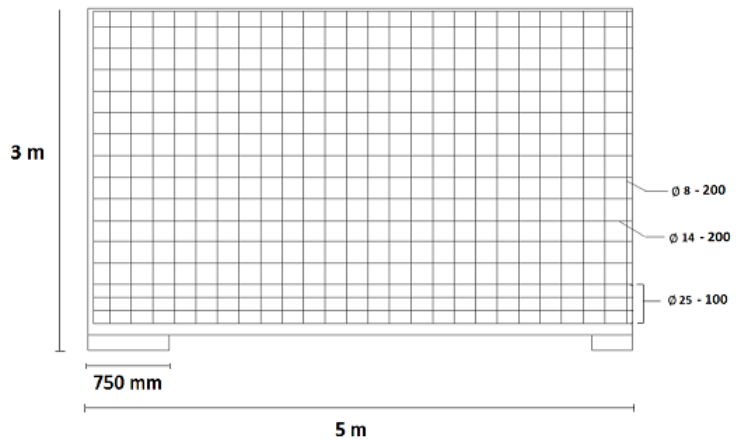


Figure 5.2.6: Reinforcement design of wall girder F1

Table 5.2.3: Reinforcement design of model F1

Model F1			
q (ULS)	660 kN/m	q (SLS)	440 kN/m
n		s	
Bottom reinforcement	4 layers 2 x Ø25		100 mm
Vertical web reinforcement	Ø8		200 mm
Horizontal web reinforcement	Ø8		340 mm
Upper tensile reinforcement	4 layers 2 x Ø25		80 mm

Table 5.2.4: Reinforcement design of model F2

Model F2			
q (ULS)	660 kN/m	q (SLS)	440 kN/m
n		s	
Bottom reinforcement	4 layers 2 x Ø25		100 mm
Vertical web reinforcement	Ø8		200 mm
Horizontal web reinforcement	Ø14		200 mm

5.3 Finite element models and results

In this chapter, the wall girder models that are used in the numerical analysis of this report are discussed. The material properties of the concrete and the reinforcement are the same as for the analyses on the pile caps. The material properties are discussed in chapter 4.3 of this report. The safety format is already discussed in chapter 4.3, for the wall girders also the GRF-method is used.

The distributed load is incrementally applied on the wall girders. Unfortunately, no use can be made of displacement control (as the load is distributed over the full length of the wall). Energy and displacement norms are used with a tolerance of 0.001 and 0.01 respectively. The maximum number of iterations is set at 50. The mesh size is chosen using the Guidelines, resulting in a mesh size of 150 mm for models D1, D2, E1 and E2. For models F1 and F2 a mesh size of 90 mm is used. The load is applied in load steps of 7.87 kN/m. When approaching the failure load, Load steps of 1.57 kN/m are applied for models D and E, this is done to study the influence of the additional reinforcement above the supports in more detail.

Model D1 and E1 are already presented in Figure 5.2.2 and Figure 5.2.3. Difference between Models D1 and D2, and E1 and E2 is the amount of reinforcement above the supports. To study the influence of the reinforcement above the supports, an increased amount of reinforcement is applied locally above both supports for model D2 and E2. This is presented in Figure 5.3.1 and 5.3.2, the red bars represent the additional reinforcement with respect to model D1 and E1. The additional vertical bars have a diameter that is equal to the vertical web reinforcement and is applied at both sides of the wall. The additional horizontal reinforcement has the same diameter as the horizontal web reinforcement and is also placed at both sides of the wall. Models F1 and F2 are already presented in chapter 5.2 (Figure 5.2.5 and 5.2.6). In the Figures below the geometry of the finite element models is presented.

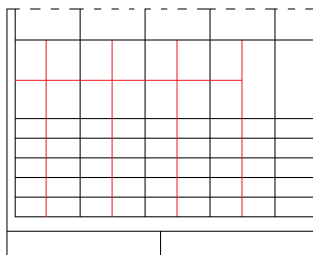


Figure 5.3.1: Reinforcement detail model D2

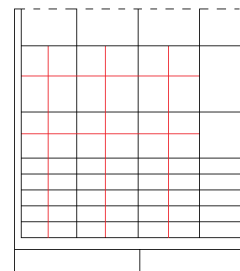


Figure 5.3.2: Reinforcement detail model E2

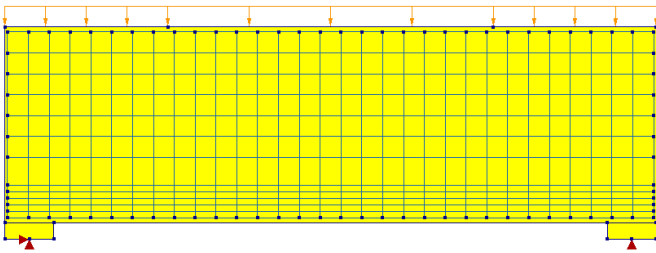


Figure 5.3.3: Finite element model for wall girder model D1

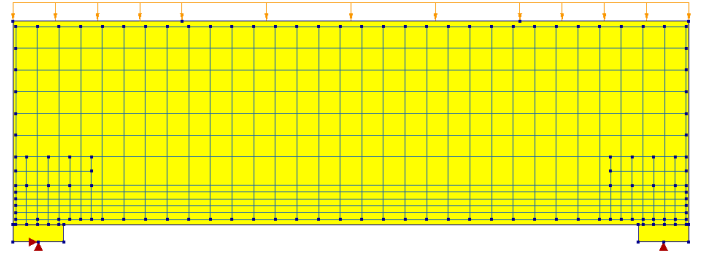


Figure 5.3.4: Finite element model for wall girder model D2

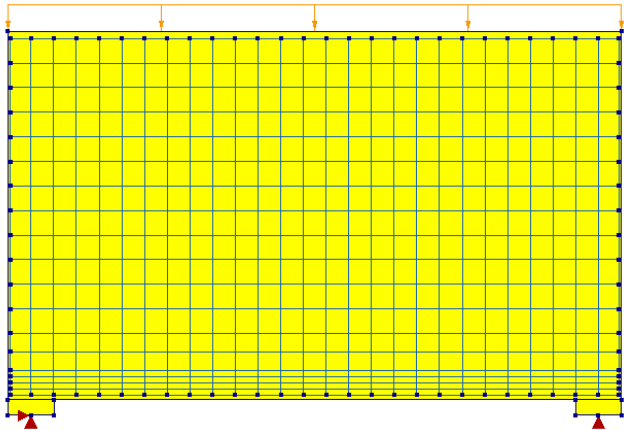


Figure 5.3.5: Finite element model for wall girder model E1

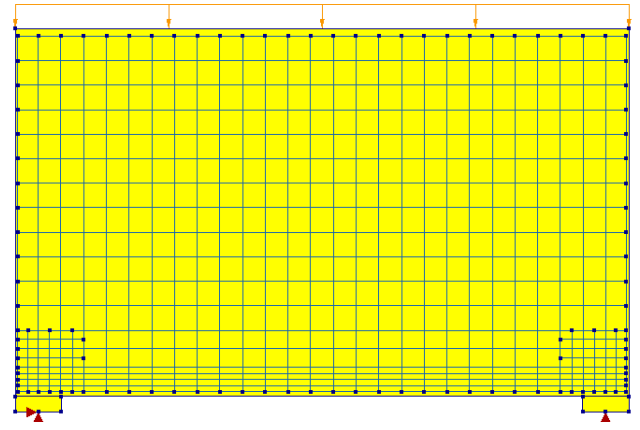


Figure 5.3.6: Finite element model for wall girder model E2

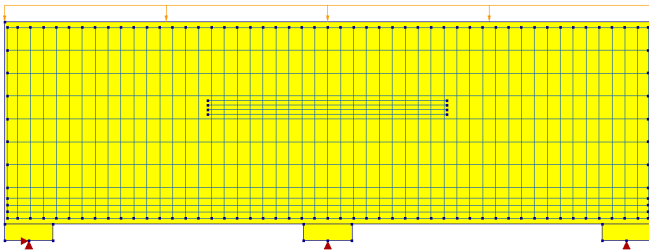


Figure 5.3.7: Finite element model for wall girder model F1

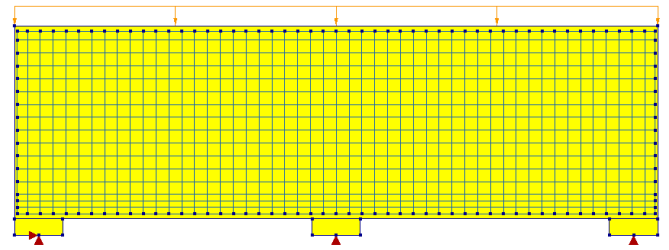


Figure 5.3.8: Finite element model for wall girder model F2

The load-deflection curves for the models are presented in Figure 5.3.9, 5.3.10 and 5.3.11. The curves of model D1 and D2 are very similar and follow approximately the same path. The difference can be found in the final capacity, the same holds for model F1 and F2.

The analytical load and the numerical loads for both reinforcement designs are presented in the plots. For model F1 and F2 the total horizontal reinforcement ratio is indicated in the graph. This includes both main reinforcement and web reinforcement. For model F1 the amount of top reinforcement is multiplied by 0.4, as it is only applied over 0.4 times the length of the wall.

The numerical calculations are post-checked by letting the calculation continue if the convergence criteria are not met. For a lot of load steps in the calculation, no convergence is observed. These load steps are indicated in the curves by the red crosses. This is only done for the model in the graph that contains the most load steps without convergence, in order to maintain clarity of the graph. A maximum variation of displacement of 0.0303 and a maximum variation of energy of 0.0294 is observed for the last iteration of the load steps, while the tolerances are set at 0.01 and 0.001 respectively.

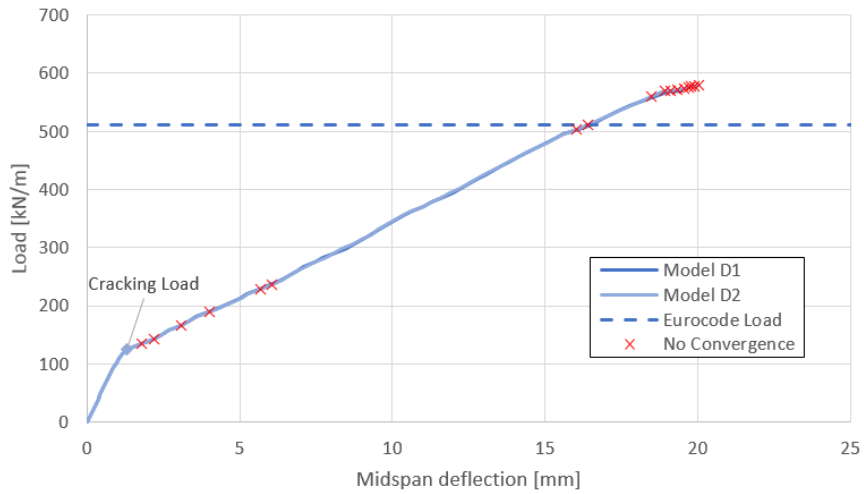


Figure 5.3.9: Load deflection curve of model D1 and D2

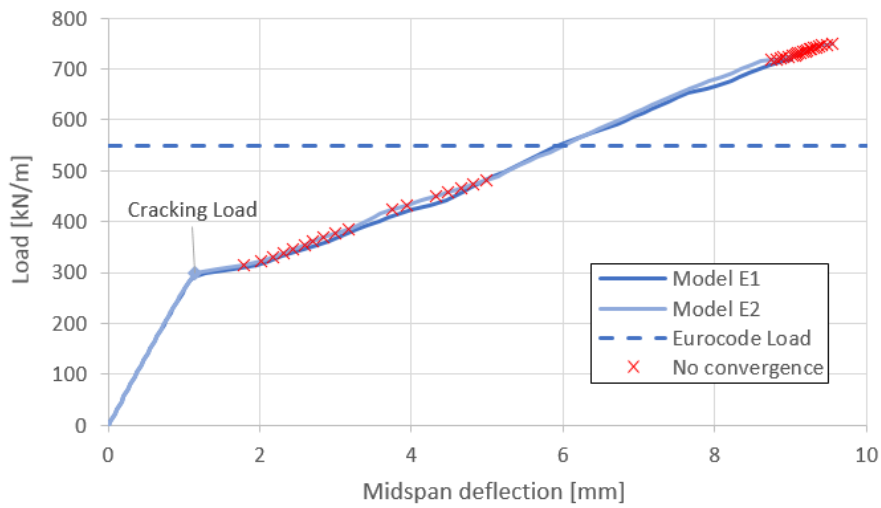


Figure 5.3.10: Load deflection curve of model E1 and E2

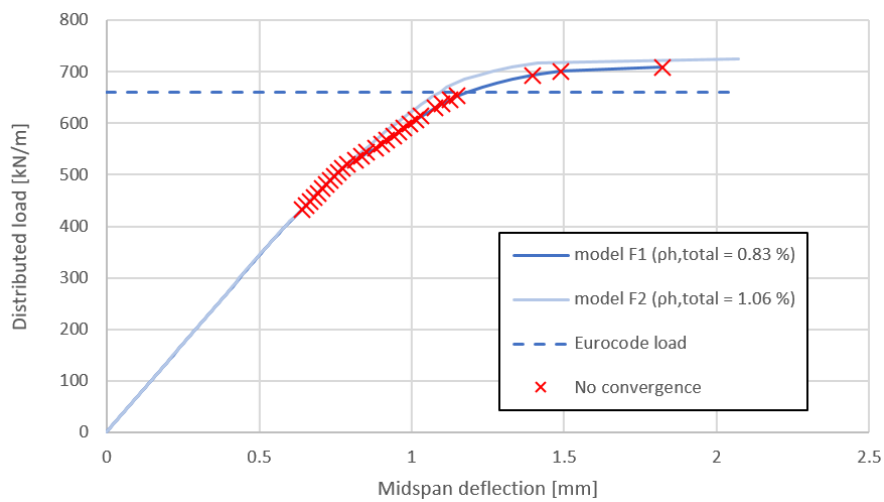


Figure 5.3.11: Load deflection curve of model F1 and F2

In the graphs it is observed that all models have a higher numerical failure load compared to the analytical failure load. The numerical failure loads for the continuous models (F1 and F2) are closer to the analytical load compared to the simply supported models (D and E). This is explained by an underestimation of the middle support reaction. For the simply supported walls, it is clear that both supports bear the same load. For the continuous walls it is assumed in the calculation (chapter 5.2) that the middle support bears two times more load than the outer supports. From the numerical results it however followed that this assumption was not valid and underestimates the middle support reaction. This will be discussed in more detail in chapter 6.

The curve looks similar for the simply supported models. First a linear part is observed, subsequently a kink in the curve is observed at the point where the first stable cracks are initiated, this point is indicated in the graphs. After this kink another (approximately) linear part is observed, but with a lower stiffness. This linear part decays when approaching final failure of the wall, this failure is initiated above the supports. A significant difference between model D and model E is that the cracking load of model E is higher than for model D. Model D is loaded more in bending than model E, and therefore this earlier cracking makes sense. Plots of the crack pattern and the concrete stresses at the last load step before failure of model D1, E1 and F1 are presented in Figure 5.3.12 and 5.3.13. From the concrete stresses it can be observed that model D1 is loaded more in bending than model E1, by the compressive stresses at the top of the beam. Also, the deflection of model D is significantly higher than the deflection of model E. This was expected, as model E1 is 'deeper' than model D1.

The load-deflection curve for model F is different. This curve contains no 'kink'. Initially the curve is linear, the curve gradually decays until failure. This failure is initiated by crushing of the concrete above the middle support. Deflections of the continuous wall are very small, it can also be observed from the plots that the crack width is also very small compared to model D and E. The capacities for each model are presented in Table 5.3.1.

Further details of the numerical results are discussed in the discussion chapter of this report.

The following plots of each model can be found in Appendix C:

- Concrete compressive stresses at last load step before failure
- Horizontal reinforcement stresses at SLS load
- Reinforcement strains at last load step before failure
- Crack width at last load step before failure

Table 5.3.1: Numerical Failure Loads of wall girder models

Model	Numerical Failure Load [kN/m]	Analytical Failure Load [kN/m]	Crack Load [kN/m]	Wall Height [m]	Wall span [m]	Number of spans	Longitudinal Reinforcement ratio [%]	Failure mode
D1	568.5	510	126	3	9.25	1	0.85	Shear next to support
D2	579.5	510	126	3	9.25	1	0.85	Shear next to support
E1	718.1	550	299	6	9.25	1	0.43	Crushing above support
E2	749.6	550	299	6	9.25	1	0.43	Crushing above support
F1	708.7	660	393	3	4.63	2	0.52	Crushing above support
F2	724.4	660	393	3	4.63	2	0.52	Crushing above support

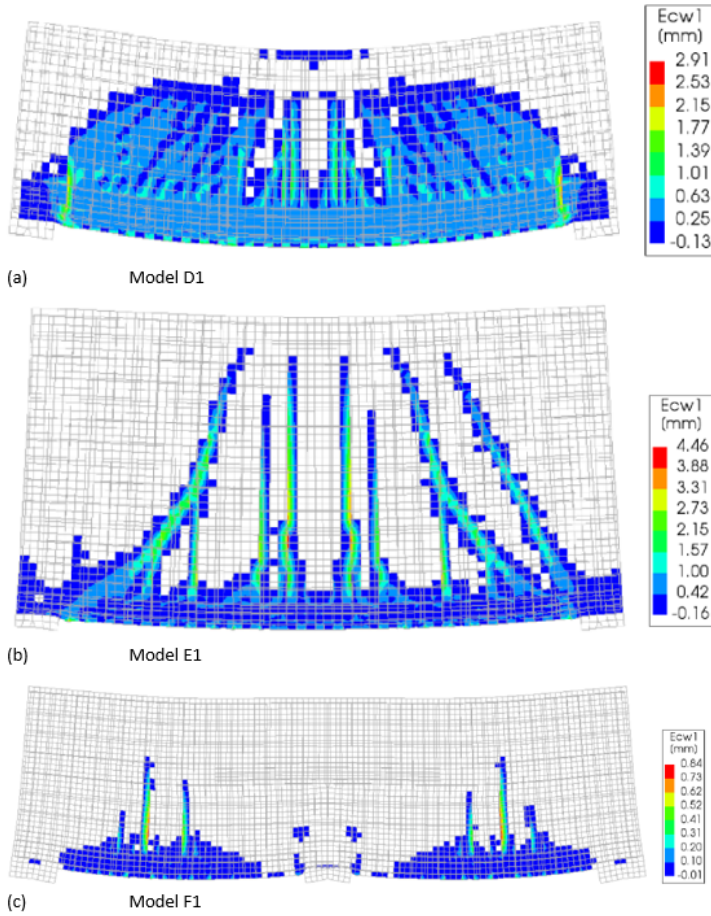


Figure 5.3.12: Crack pattern at final load step before failure for wall girder model D1 (a), E1 (b) and F1 (c)

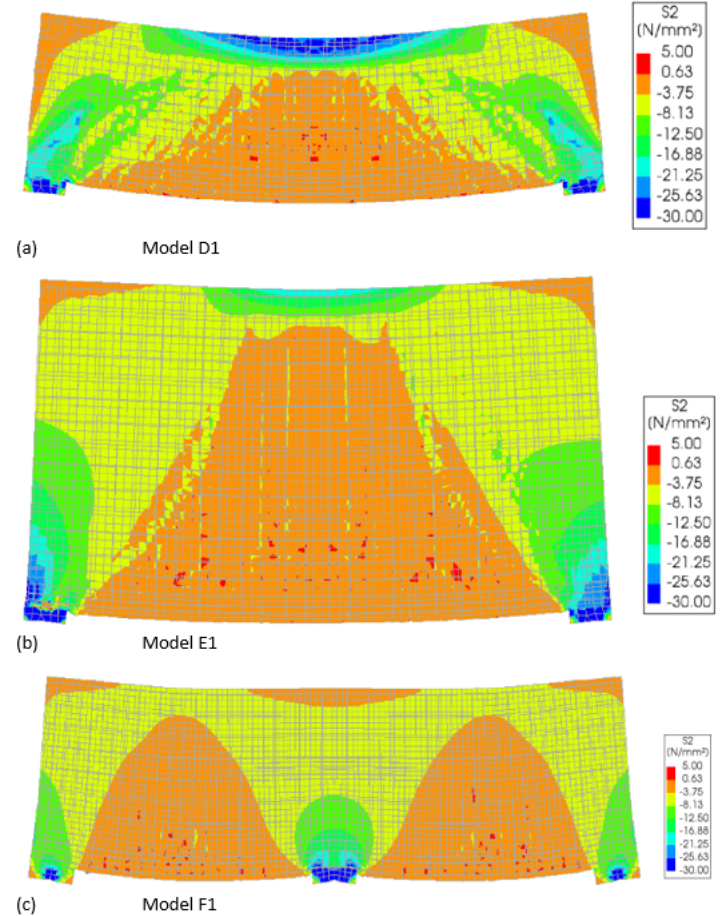


Figure 5.3.13: Concrete compressive stresses at final load step before failure for wall girder model D1 (a), E1 (b) and F1 (c)

5.4 Conclusion

From the results of the calculations discussed in this chapter, it can be concluded that the numerical failure load appeared to be higher than the analytical failure load for all wall girder models. Failure of the wall girders is for all models initiated at the support. However, differences are observed between the failure of models D and E. Models D fail due to shearing off of the section above the support, while models E fail due to crushing of the concrete above the support.

The additional reinforcement results in a higher numerical capacity, as expected. The application of additional reinforcement appears to be more efficient when the span to depth ratio becomes smaller as it results in a higher capacity increase for model E compared to model D. This is discussed in more detail in chapter 6.4.

The load deflection curves for both reinforcement designs of model D and E are approximately identical, only the capacity is higher for model D2 and E2 compared to model D1 and E1 respectively.

For model F, the same failure mechanism is observed as for model E. The continuous wall girder fails due to crushing of the concrete above the intermediate support. The numerical capacities for models F1 and F2 are closer to the analytical capacity of model F compared to models E, despite the same failure mechanism. This is discussed in more detail in chapter 6.5.

6 Discussion of results

6.1 Dimensions of the nodes

6.1.1 CCT nodes

Above the piles of the pile caps and above the supports of the wall girder, CCT nodes are present. The node contains two compression surfaces, the dimensioning of the first compression surface is straightforward as this is just the pile or support dimension. As already discussed before, the node also contains a diagonal compression surface. The dimension of this diagonal surface depends on the height of the node. In section 6.5.4 of NEN-EN 1992-1-1:2005 [13] an expression for the height of the node is provided which is dependent on the position of the main reinforcement. This is illustrated in Figure 6.1.1.

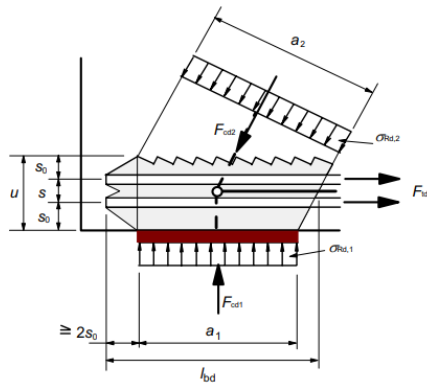


Figure 6.1.1: CCT node [13]

The height of the node (u) is defined in the Eurocode as two times the distance from the bottom of the concrete to the center of gravity of the main reinforcement. A significant difference between the pile caps and the wall girders in this report is the distribution of the main reinforcement. The pile caps contain one layer of main reinforcement, while the wall girders contain several (up to 6) layers of main reinforcement. This results in a higher node for the wall girder as the center of gravity of the reinforcement lays significantly higher than for the pile caps. Another significant difference is the strut angle. For the pile caps it is assumed that the load transfers through one strut directly to the supports, so the strut angle follows from the geometry of the pile cap. For the wall girder a maximum strut angle of 68° is assumed, where multiple struts are present in the strut-and-tie model.

In Figure 6.1.2, 6.1.3, 6.1.4 and 6.1.5 the compressive stresses at the nodes are presented for model A1, C2, D1 and E1 respectively. A contour plot is presented in the figures where the dimensions of the node are indicated. In this plot, a local axis is indicated along the node. At the right side of the figures, a plot is given of the compressive stresses along this local axis. The stress that is assumed analytically, from the Load level that is observed, is also plotted in the graphs. The dimension and position of the node is indicated in this plot by point A and point B. The node is, following the Eurocode, in between these points.

The node dimensioning of the Eurocode is obviously a simplification of reality and the actual stress field at the nodes will not exactly look like how it is assumed in calculations. However, from the compressive stress contour plots of the pile caps it can be observed that the dimensions that are used in the calculation are similar to the numerical results. The strut angle that resulted from the calculation is also approximately observed in the numerical

results. In the contour plots it is observed that the numerical strut is wider than the calculated strut width, but a smaller part of the strut contains larger stresses. This part falls within the calculated width of the strut. This also follows from the graphs of the stresses. In these graphs it is observed that the peak values of the compressive stresses are within the node (in between point A and point B). From the graphs it is observed that the strut-and-tie model gives an overestimation of the stresses compared to the numerical results. From this it follows that the strut-and-tie method provides a conservative solution with respect to numerical results.

For the wall girders, more differences are observed between the assumed struts and nodes and the numerical ones. The strut for model D1 appears to run more horizontal than assumed while the strut of model E1 appears to run more vertical than assumed. Similar as for the pile cap models, the stresses are spread over a larger surface than assumed by the node dimensioning of the Eurocode. From the graphs it can however again be observed that the largest stresses are actually within the node dimensions. However, the compressive stresses are distributed over a wider area than assumed by the strut width of the strut-and-tie method. For model D1 it looks like two struts with different angle are present, these can be distinguished by the two peaks in the graph. Stresses in the node exceed the assumed stress in the node, as can be seen from the stress graphs. For model D1 the total stress over the width of the node is numerically higher than was assumed analytically (area under stress graph within node). This can be prescribed to the fact that a higher strut angle was assumed. A higher strut angle results in a lower strut force.

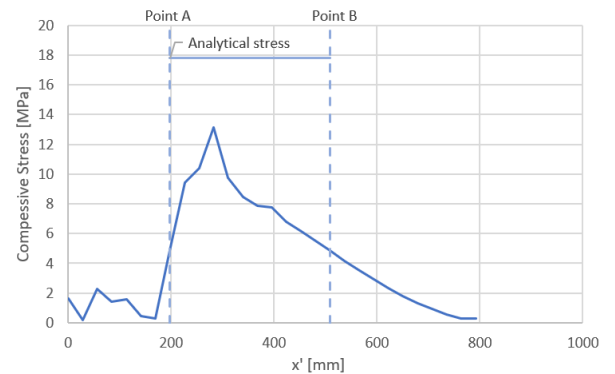
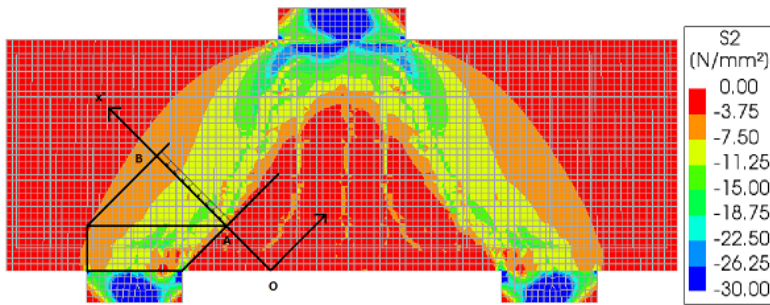


Figure 6.1.2: Numerical and Analytical (strut-and-tie model) compressive stresses along node (in between point A and B) in pile cap model A1

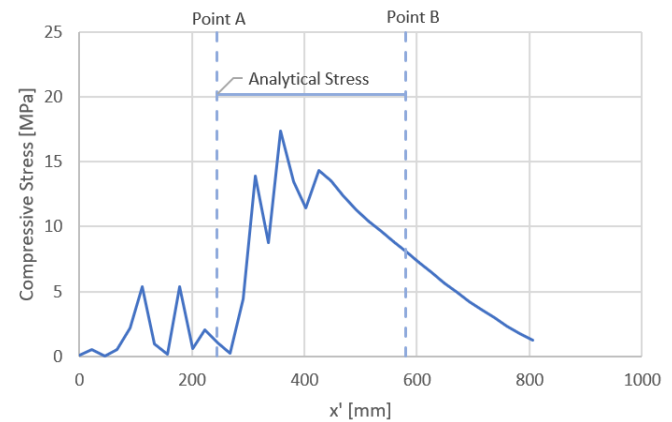
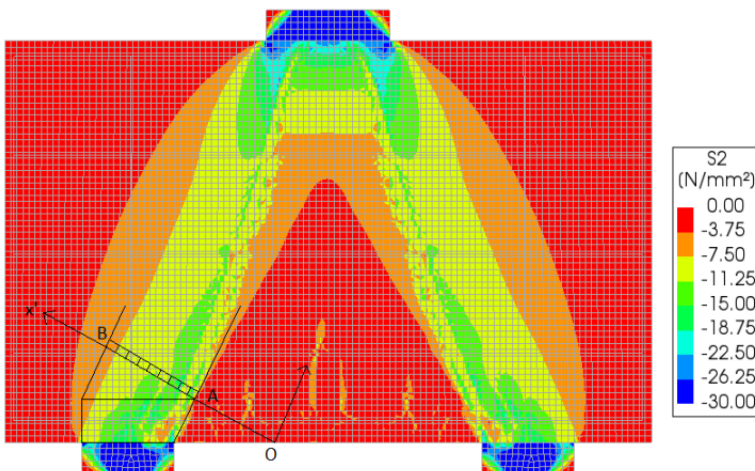


Figure 6.1.3: Numerical and Analytical (strut-and-tie model) compressive stresses along node (in between point A and B) in pile cap model C2

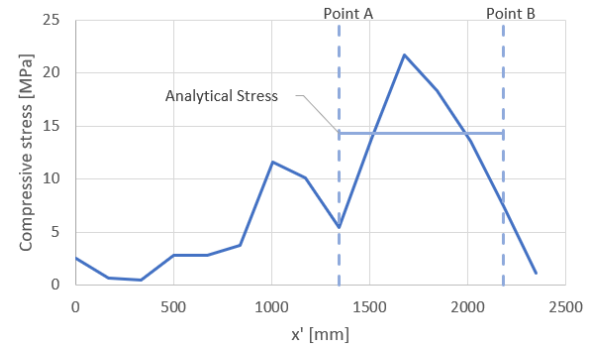
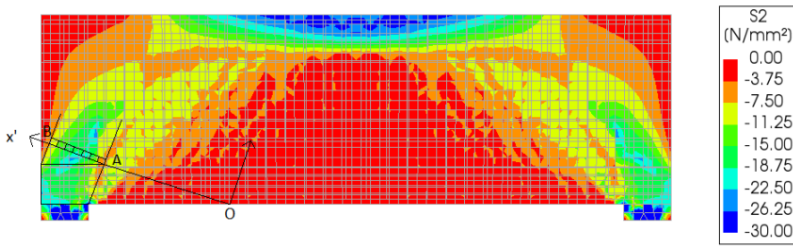


Figure 6.1.4: Numerical and Analytical (strut-and-tie model) compressive stresses along node (in between point A and B) in wall girder model D1

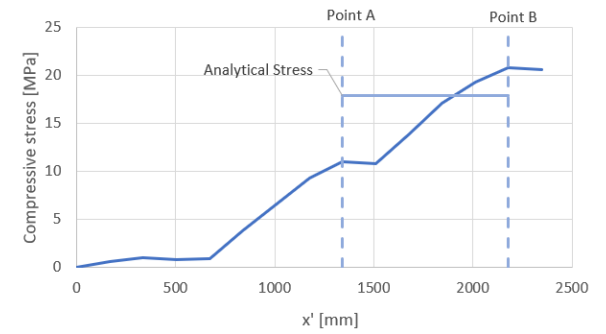
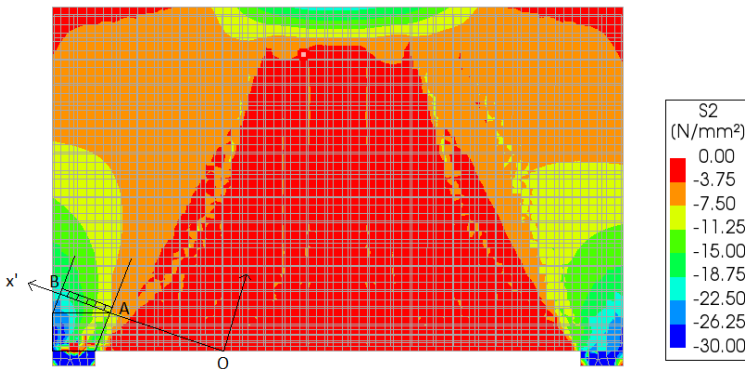


Figure 6.1.5: Numerical and Analytical (strut-and-tie model) compressive stresses along node (in between point A and B) in wall girder model E1

The CCT nodes also play an important role in anchoring of the main reinforcement. Starting of the anchorage is assumed to be at the node, as here the compression zone starts. In Figure 6.1.6 and 6.1.7 the concrete stresses at main reinforcement level along the pile cap are presented for pile cap model A1 and C2 respectively. The plot starts at $x = 250$, this is above the outer point of the pile. The point where the node ends (and anchorage starts) is indicated in the graphs.

In the graphs it is observed that for both models the full node is in compression. At the end of the node and left to this, only compressive stresses are observed. This makes it a fair assumption to use the dimension of the node for anchorage of the main reinforcement.

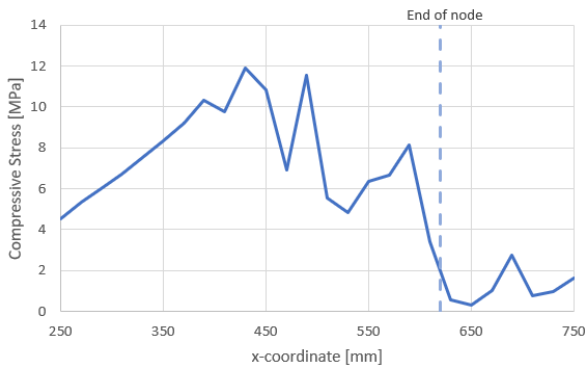


Figure 6.1.6: Compressive stresses at main reinforcement level for pile cap model A1

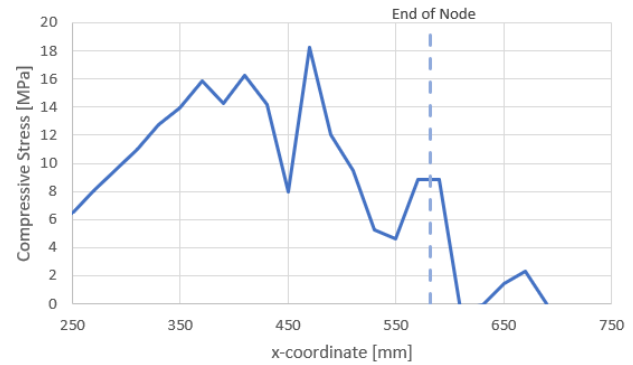


Figure 6.1.7: Compressive stresses at main reinforcement level for pile cap model C2

6.1.2 CCC node pile cap

For the CCC node, that is present under the column of the pile cap, no dimensions are proposed in the Eurocode. The engineer has to assume the dimensions of this node. In the calculations that are made in this report a hydrostatic node is assumed. In a hydrostatic node, as was already introduced in chapter 2.1.3 of this report, the stresses are equal on all surfaces of the node.

In Figure 6.1.8, 6.1.9 and 6.1.10 the concrete compressive stresses at the last load step before failure are presented in a contour plot for pile cap models A1, B1 and C2 respectively. In these plots, the assumed node dimensions are indicated. The compressive stresses along the local axis x' , that is indicated in the contour plot, are plotted in the figures. In these plots, the assumed end of the node is indicated by the dotted vertical line. Also alternative node dimensions are indicated, these alternative node dimensions are discussed below. It is observed that the assumed node dimensions differ from the numerical node dimensions. The node is analytically calculated based on the strut angle (to obtain equal stresses), this indicates that the node height decreases where the strut angle increases. However, from the contour plots it can be observed that an increasing strut angle (and depth) results in an increasing node height.

It is clearly observed from both the contour plots and the stress graphs, that the assumption of the hydrostatic node deviates from the numerical results significantly. In literature an expression was found for the height of this node based on the reinforcement ratio and the effective height of the cross section [11], this expression is given in formula 6.1.

$$h_{node} = (\sqrt{(n\rho)^2 + n\rho} - n\rho)d \quad (6.1)$$

This results in a smaller node height for model A and larger node heights for model B and C. Resulting node heights are presented in Table 6.1.1. When comparing the node heights and compare this with the numerically computed stresses, it is observed that the node heights using the alternative formula give a better approximation of reality. In figure 6.1.8 it is observed that the assumed node height is chosen too large as at the point where the node ends, the stresses are already close to zero. With the alternative node height, calculated using formula 6.1, the node ends at the point where the stresses are larger. The highest stresses are covered within the node and this node height provides a better approximation than the hydrostatic node assumption. For the nodes of model B and C it is the other way around, the hydrostatic node ends at a point where the stresses are still relatively large. The node following equation 6.1 ends where the stresses are smaller and gives again a better approximation for the node height.

Table 6.1.1: Node heights for CCC nodes of pile caps

Pile cap Model	node height following equation 6.1 [mm]	Hydrostatic node height [mm]
A	113	200
B	150	115
C	163	93

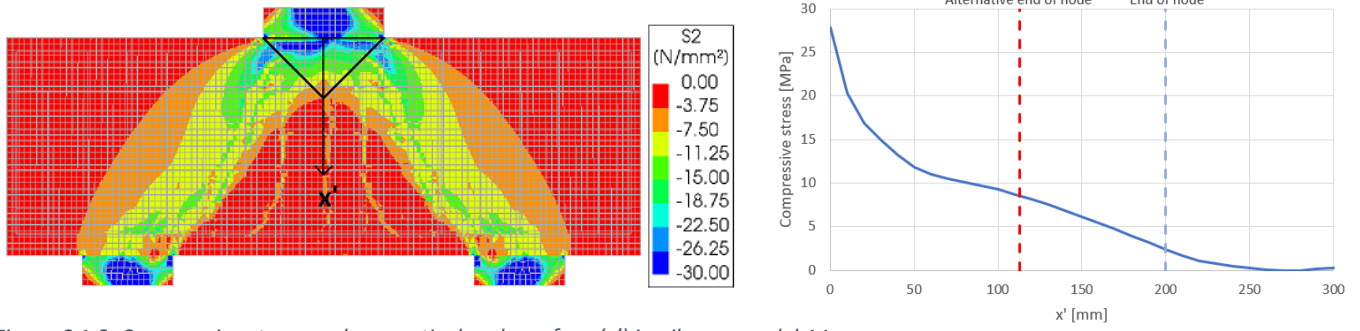


Figure 6.1.8: Compressive stresses along vertical node surface (x') in pile cap model A1

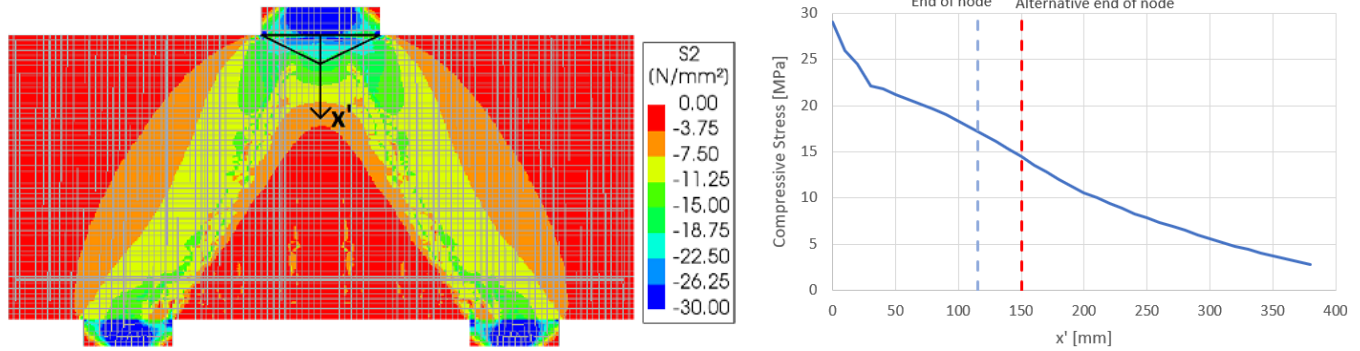


Figure 6.1.9: Compressive stresses along vertical node surface (x') in pile cap model B1

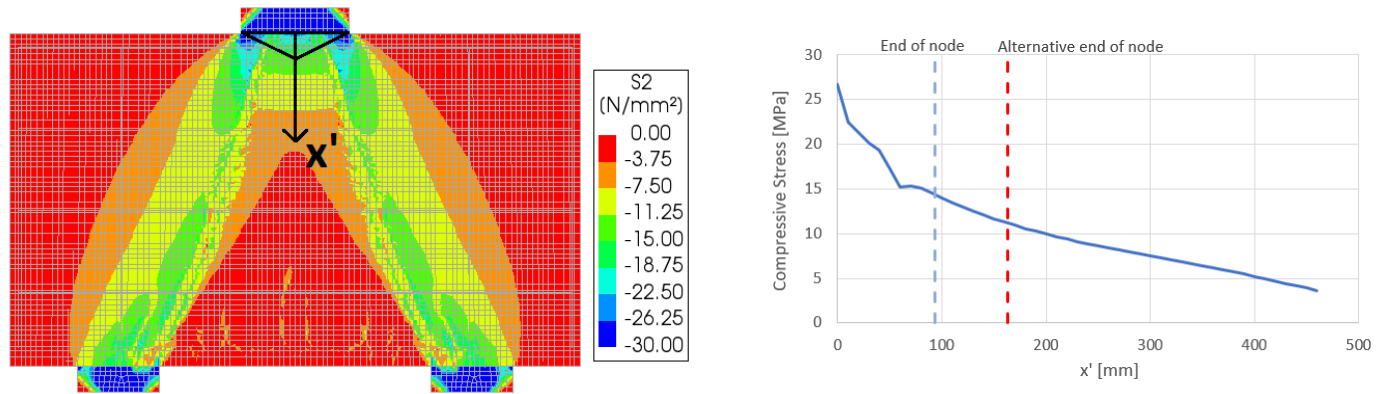


Figure 6.1.10: Compressive stresses along vertical node surface (x') in pile cap model C2

6.2 Web reinforcement of the pile caps

To study the influence of the web reinforcement in the pile caps, for each model two designs are made. The first design contains a web reinforcement ratio that is based on the minimum amount of web reinforcement for deep beams. The second design contains a web reinforcement ratio that is based on the stresses in the pile cap.

As already mentioned in chapter 5.3, it is remarkable that the final Load on model C2 is higher than model C1, despite the higher web reinforcement ratio for model C1. The web reinforcement is applied to prevent the pile cap from diagonal splitting. The initiation of the diagonal splitting cracks is clearly observed in the Load-deflection curves of the pile caps, as discussed in chapter 4. For model A1 and A2 the decrease in load in the Load path represents the initiation of flexural shear cracks. These cracks differ from the diagonal cracks that run from the support to the column. The flexural shear cracks are initiated at mid span and mid depth and run vertical. After this point, the diagonal cracks in model A1 and A2 are also initiated. The difference can be observed in Figure 6.2.4.

Relevant results for this chapter, of the results that were already presented in Table 4.3.5, are again presented in Table 6.2.1. From the table it is observed that the cracking load is higher for the models that have more web reinforcement, this is as expected. However, the cracking loads are relatively close to each other, despite a significant difference in amount of web reinforcement. For pile cap models B1, B2, C1 and C2 the diagonal cracking loads can assumed to be the failure loads, with diagonal splitting as the failure mechanism.

In the Load-deflection curves or in the Load-strain curves that are presented below, it is observed that the load decreases significantly for these models when the diagonal cracking load is reached. A decrease in load of 15, 26, 19 and 28 % is observed after diagonal cracking for model B1, B2, C1 and C2 respectively. Also, the cracks for models B and C are significantly larger than for models A1 and A2. In Figure 6.2.1, 6.2.2 and 6.2.3 the maximum web reinforcement strain is plotted against the Load for pile cap models A, B and C respectively. The maximum strain in the web reinforcement is located in the horizontal bars that run through the middle of the diagonal crack (part with the largest crack width). For model B2 and C2, rupture of this reinforcement bar takes place. It is observed that this does not directly lead to failure and the load can still be increased. However, rupture of the reinforcement is obviously not preferred, besides that it results in large diagonal cracks compared to model B1 and C1. Rupture does take place at load levels that are significantly higher than the EC 2 loads that the models were designed for, for both model B2 and C2.

Table 6.2.1: Diagonal cracking loads for pile cap models (*Flexural shear cracks, see Figure 6.2.4)

Model	Diagonal cracking load [kN]	Failure Load [kN]	EC2 Load [kN]	Failure mechanism
A1	1491*	2351.5	1950	Crushing under column
A2	1403*	2218.6	1950	Crushing under column
B1	2708	2708	2450	Diagonal Splitting
B2	2639	2639	2450	Diagonal Splitting
C1	3391	3391	2600	Diagonal Splitting
C2	3378	3378	2600	Diagonal Splitting

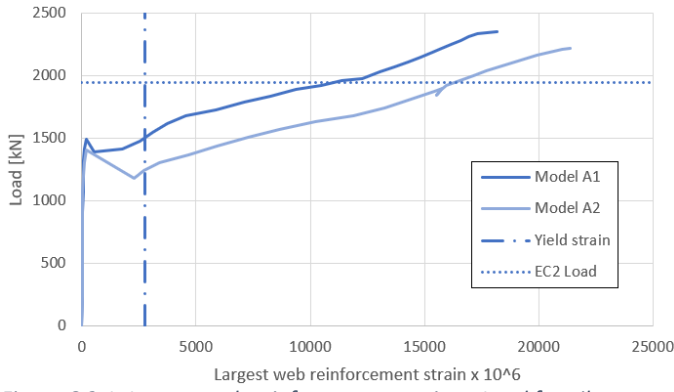


Figure 6.2.1: Largest web reinforcement strain vs Load for pile cap models A

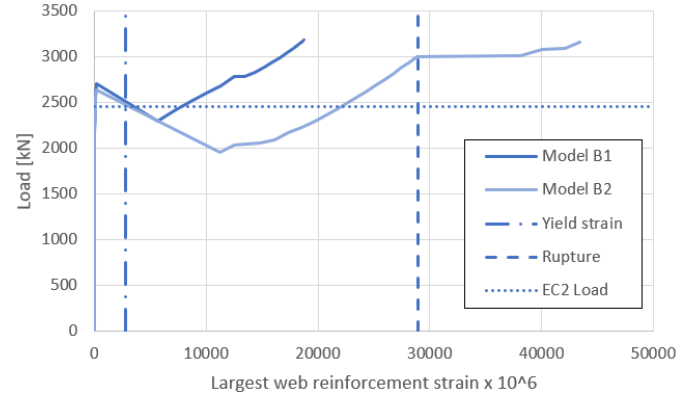


Figure 6.2.2: Largest web reinforcement strain vs Load for pile cap models B

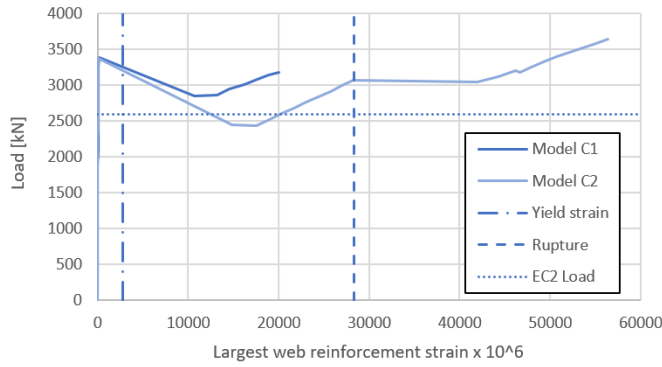
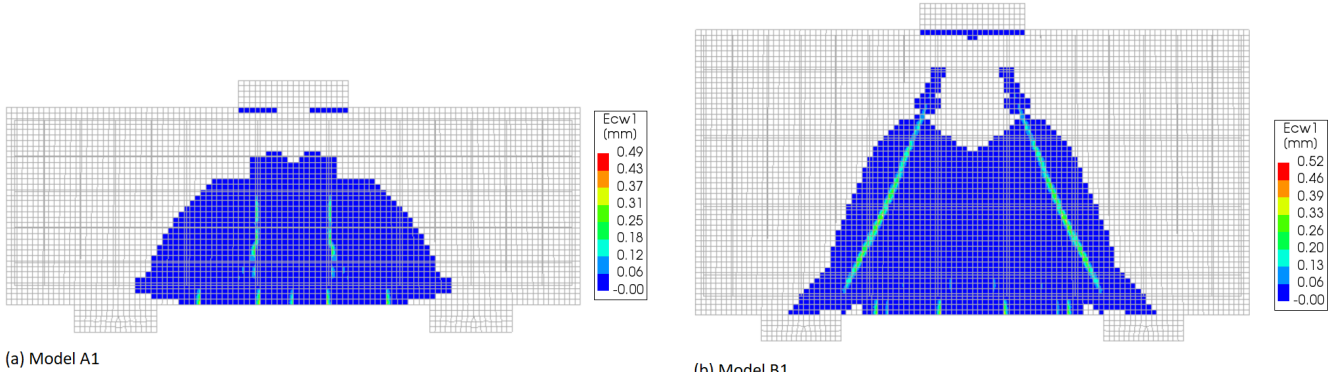


Figure 6.2.3: Largest web reinforcement strain vs Load for pile cap models C



(a) Model A1

(b) Model B1

Figure 6.2.4: Flexural shear crack of model A1 (a) and Diagonal splitting crack of model B1 (b)

6.3 Crack width control

For pile cap models B and C the governing verification for the longitudinal reinforcement is the verification for crack width control. Although a SLS load is assumed based on the ULS load and the fact that this could deviate significantly in reality, this verification can be analysed and discussed based on the steel stress. The Eurocode suggests that a crack width calculation can be based on an elastic calculation using the following lever arm:

$$z = 0.2 l + 0.4 h \leq 0.6 l$$

The Eurocode however also states that the strut-and-tie-model can be used to calculate the steel stress, provided that the compatibility of the strut-and-tie model is assured. In the verification of the pile caps the formula given above is used to calculate the steel stress.

The strain of the longitudinal reinforcement at midspan is plotted against the applied load for pile cap models B and C in Figure 6.3.1 and 6.3.2 respectively. The yield strain and the SLS load are indicated in the graphs.

The numerical midspan reinforcement strain and stress at the SLS load for the four models is presented in Table 6.3.1. The analytically calculated steel stress is also presented in the table. It is expected that the analytical steel stress is higher than the numerical steel stress, as the strut-and-tie method provides an upper bound solution. However, the difference between the numerical and analytical steel stress is significant in this case. It can be concluded that the method used to calculate the steel stress is very conservative. When calculating the steel stress using the strut-and-tie model that is also used for ULS verifications, the analytical steel stress reduces. The values are presented in Table 6.3.2. Although the steel stress is significantly lower using the strut-and-tie model, the difference between this value and the numerical steel stress is still large. However, in the verification (chapter 3.4) it was observed that the linear part of the curve is longer for the numerical results compared to experimental results (due to later cracking in numerical calculations). In the experimental results the 'kink' in the load-strain curve was obtained at a lower load, resulting in an underestimation of the strain after this point. This is illustrated in Figure 6.3.3 by the red arrow. In this case the SLS load is just after the 'kink' (Model B) and just before the 'kink' (Model C). Therefore, the strain at SLS load, and therefore the stress, might be underestimated.

It can be concluded that the steel stress at SLS load that follows from DIANA cannot be used in drawing conclusions as it is not representative.

However, in the EC2 it is stated that the strut-and-tie model may be used for the crack width calculation "if approximate compatibility for strut-and-tie models is ensured (in particular the position and direction of important struts should be oriented according to linear elasticity theory)". From Figure 6.1.2 and 6.1.3 it was observed that the direction and position of the struts appeared the same as was assumed in the strut-and-tie model for the pile caps.

In Figure 6.3.4, 6.3.5 and 6.3.6 the horizontal stresses over the midspan cross-section are plotted at the SLS load for model A1, B1 and C1 respectively. This is done to see if the internal lever arm for deep beams can be recognized. From the plots it is obvious that the cross section is not loaded in pure bending. It must be mentioned that nodal averaging is used.

The internal lever arm is determined by the distance from the reinforcement level to the centre of the compressive zone. For model A this corresponds with the lever arm for deep beams that is proposed by the Eurocode. From the Eurocode a lever arm of 548 mm is calculated and from the stresses a lever arm of 550 mm is observed. For pile cap model B1

and C1 the lever arm is underestimated by the Eurocode. The Eurocode lever arms are 692 and 780 mm while from the plots the lever arms are 870 mm and 1070 mm for model B1 and C1 respectively. It is observed that the compressive zones of model B1 and C1 are very small and does not look like a cross-section in bending at all.

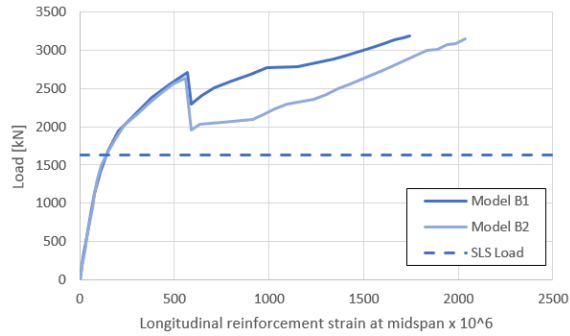


Figure 6.3.1: Longitudinal reinforcement strain at midspan for pile cap models B1 and B2 (ultimate strain = 2750×10^{-6})

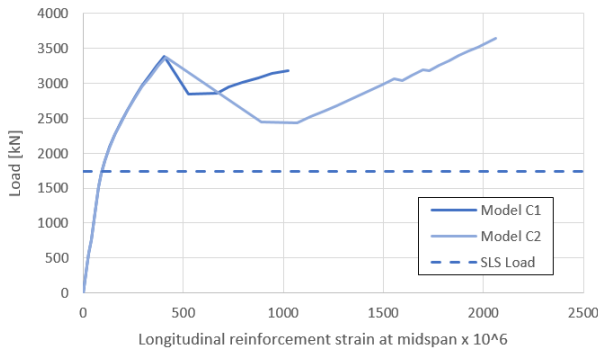


Figure 6.3.2: Longitudinal reinforcement strain at midspan for pile cap models C1 and C2 (ultimate strain = 2750×10^{-6})

Table 6.3.1: Reinforcement strains and stresses at midspan for pile cap models B and C (at SLS Load)

Model	Numerical Reinforcement strain [-]	Numerical Reinforcement stress [MPa]	Analytical Reinforcement stress [MPa]
B1	0.00015	30	295.1
B2	0.00015	30	295.1
C1	0.00011	22	277.8
C2	0.00011	22	277.8

Table 6.3.2: SLS Steel stress using strut-and-tie model

Model	Analytical Reinforcement stress [MPa]
B1	214.4
B2	214.4
C1	183.1
C2	183.1

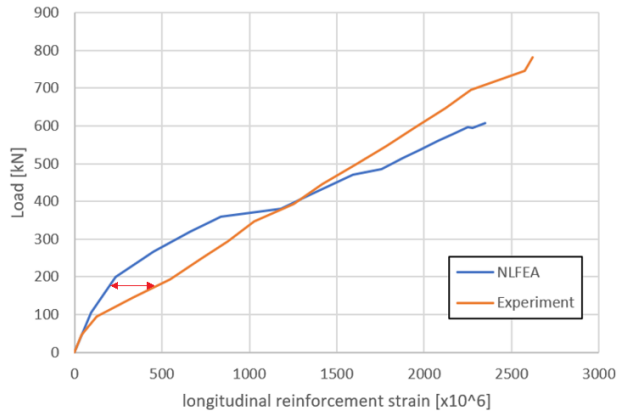


Figure 6.3.3: Load-strain curve of test specimen MDB-3 (chapter 3.4)

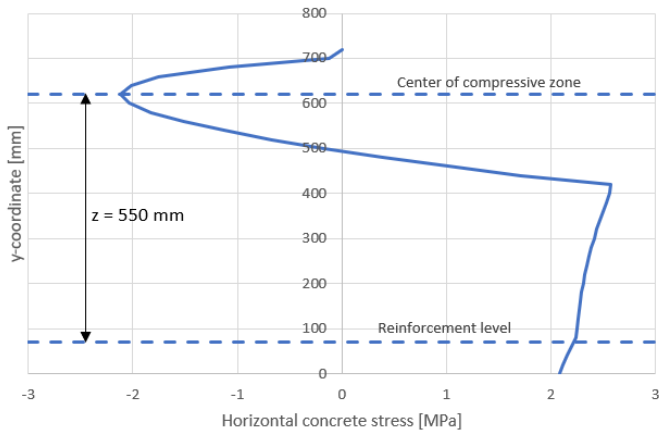


Figure 6.3.4: Horizontal Stresses over the height at midspan for model A1

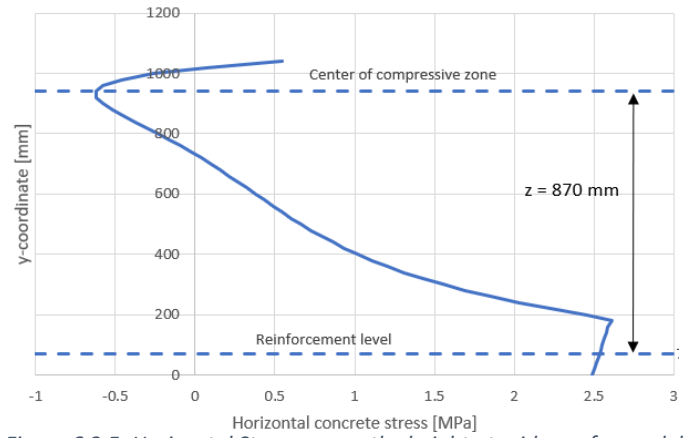


Figure 6.3.5: Horizontal Stresses over the height at midspan for model B1

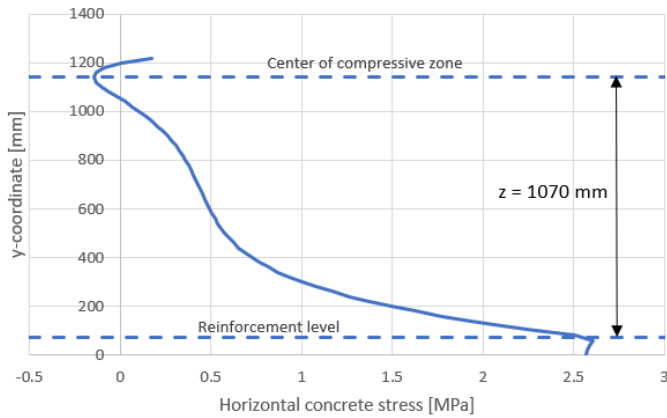


Figure 6.3.6: Horizontal Stresses over the height at midspan for model C1

6.4 Reinforcement above the supports of a wall girder

To study the influence of additional local reinforcement above the supports, model D2 and E2 contain additional reinforcement above the supports with respect to model D1 and E1 respectively. As was discussed in chapter 5, the web reinforcement was applied twice as much above the supports.

Two different failure mechanisms were observed for model D and model E respectively. Model D failed due to shearing off of the section above the support, this can be observed in the crack pattern that is presented in figure 6.4.1. Large cracks are formed at the edges of the support. The failure for model E is different than the failure for model D. The failure for model E is similar to the failure mechanism that was observed for the pile caps, the concrete stresses at the support become too large and the concrete starts crushing. Difference between the failure modes of the two walls can be prescribed to the difference of the height. As model E contains a larger height, it is less loaded in bending and the load is transferred more directly to the supports with respect to model D. This can also be concluded from the differences in crack patterns. The crack pattern of model E is similar to the crack pattern of the pile caps, the diagonal cracks can clearly be observed. The crack pattern of model D contains more flexural shear cracks.

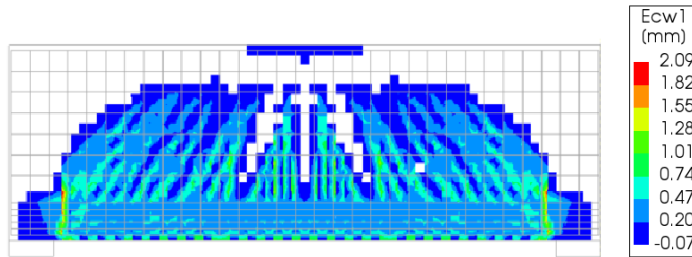


Figure 6.4.1: Crack pattern at final load step before failure for model D1

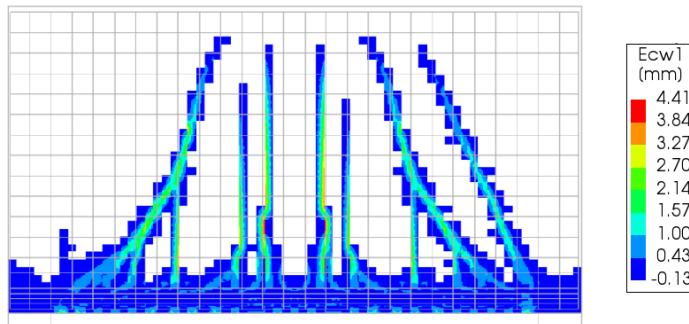


Figure 6.4.2: Crack pattern at final load step before failure for model E1

To gain more insight in the effectiveness of the additional reinforcement, the reinforcement stresses above the support are presented in a contour plot in Figure 6.4.3 up till 6.4.6. It is noticed that the reinforcement that is located above the support of model contains large compressive stresses, this induces that the load is transferred to the support directly. These large compressive stresses are indicated in Figure 6.4.5 by the red circle. These large compressive stresses can also be found in the additional vertical reinforcement that is applied in model E2. In model D, these large compressive stresses are not found above the supports. This induces that for model E, the capacity can be increased by applying additional vertical reinforcement above the support. As the strut was observed to be approximately

vertical, a simple hand calculation can be made to predict the increase in support capacity. The area of the increased amount of vertical reinforcement above the support is known, this can be multiplied by: $(f_y - f_{cd})$ to obtain the expected increase of support capacity. This is done for model E, the result is presented in Table 6.4.1. It is observed that this expected value is higher than the numerical increase in support capacity. For model D, the stresses in the reinforcement are significantly lower compared to model E. It is known that a vertical crack is formed next to the support. However, no large tensile stresses are observed in the reinforcement at this location. Large tensile stresses might occur in this model as no bond model is used, in reality this is not possible as this is near the end of the reinforcement bars and the bars would slip. The additional reinforcement does lead to a higher capacity. The maximum load increases from 568.5 kN/m for model D1 to 579.5 kN/m for model D2. This means that the support capacity increases 55 kN. It is observed in the stress plot that at the position of the red circle in Figure 6.4.4, which is located at the position of the vertical crack, the stress is increased with respect to model D1. Due to the additional reinforcement, the stresses of the reinforcement appear to be able to be higher at the location of the crack, which provides the additional capacity.

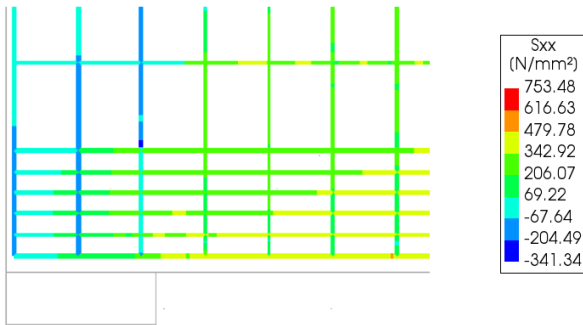


Figure 6.4.3: Reinforcement stresses above the support of model D1

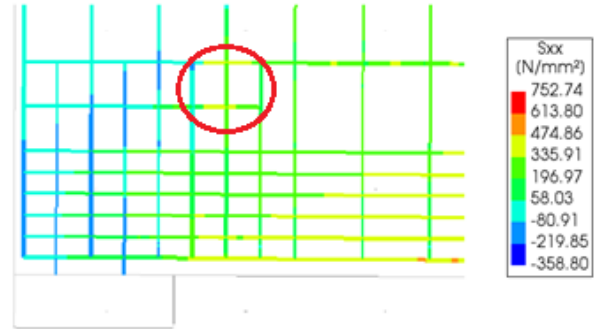


Figure 6.4.4: Reinforcement stresses above the support of model D2

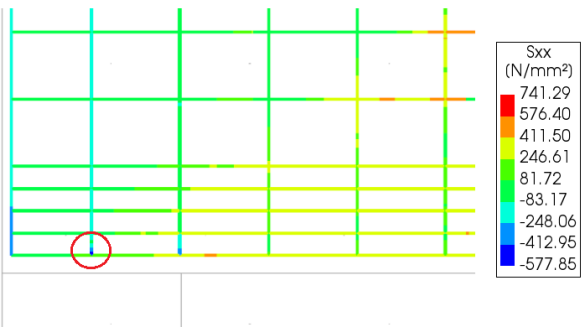


Figure 6.4.5: Reinforcement stresses above the support of model E1

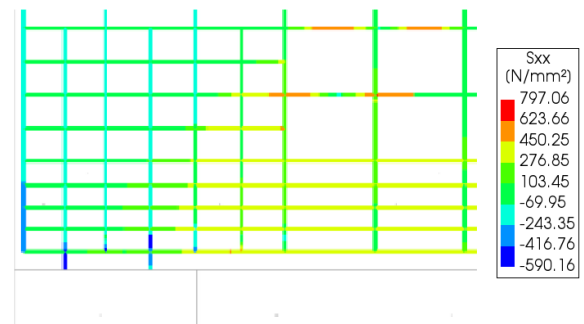


Figure 6.4.6: Reinforcement stresses above the support of model E2

Table 6.4.1: Difference in support capacity between model E1 and E2 and between model D1 and D2

Model	Support Load model 1 [kN]	Support Load model 2 [kN]	Additional vertical reinforcement above support surface [mm ²]	Difference in Support Loads [kN]	Expected difference in Support Loads [kN]
D	2842.5	2897.7	201.06	55.1	-
E	3590.6	3748	201.06	157.4	187.7

6.5 Strut-and-tie model continuous wall girder

The strut-and-tie model that is assumed in the calculation for the continuous wall girder (chapter 5.2) suggests that half of the total load is carried by the intermediate support. The other half of the load is carried by the outer supports, both supports carry a quarter of the total load each. As is already mentioned before in this report, the strut-and-tie method is just a simplification of reality and the assumption of this distribution of the support reactions might not be valid. The numerical ratio between the intermediate support reaction and the outer support reaction is plotted against the applied load, this is presented in Figure 6.5.1. From the graph it can be observed that a higher support reaction is present at the intermediate support than was suggested by the strut-and-tie model. Both for model F1 and F2 the ratio remains constant for the most part. Only when approaching failure, the ratio becomes somewhat higher. The constant value that is observed is equal to 2.27, this value seems to be independent of the reinforcement design as it is the same for both model F1 and F2.

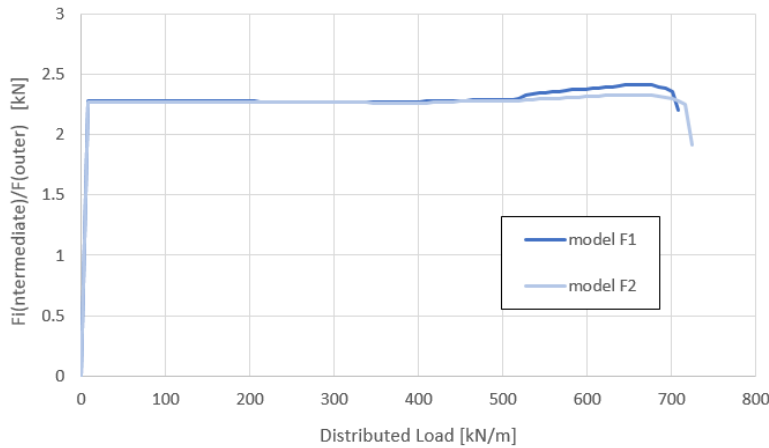


Figure 6.5.1: Distribution of the support reactions

In Figure 6.5.2, the longitudinal reinforcement strain at midspan is plotted against the applied load. From the graph it can be observed that the longitudinal reinforcement is overdesigned. The reinforcement was designed such that it should analytically yield at the ULS load. From the curves it is observed that the reinforcement is not even close to yielding at failure. The yield strain of the reinforcing steel is equal to 2392.5×10^{-6} . This suggests that the strut-and-tie model that is used for the continuous walls does not represent reality good enough as it is way too conservative regarding the main reinforcement. Also the upper tensile tie is overdesigned.

In the strut-and-tie model that is used in the calculation it is assumed that the struts have an angle of 45° from the supports. From the concrete stresses that are presented in Figure 6.5.3 it is however observed that the struts run from approximately midspan (top side) to the supports directly. This results in a higher strut angle, what will subsequently result in less main reinforcement. It is also observed that the strut that runs from the outer support is steeper than the strut that runs from the intermediate support.

From the differences between the results and the assumed strut-and-tie model that are discussed here, it can be concluded that a different strut-and-tie model that gives a better approximation of reality should be used. This strut-and-tie model should satisfy the following conditions:

- It should result in (approximately) the ratio of support reactions that is discussed here.
- The struts should run such as is observed in Figure 6.5.3.
- The longitudinal reinforcement that results from the model must not be 'too conservative'.

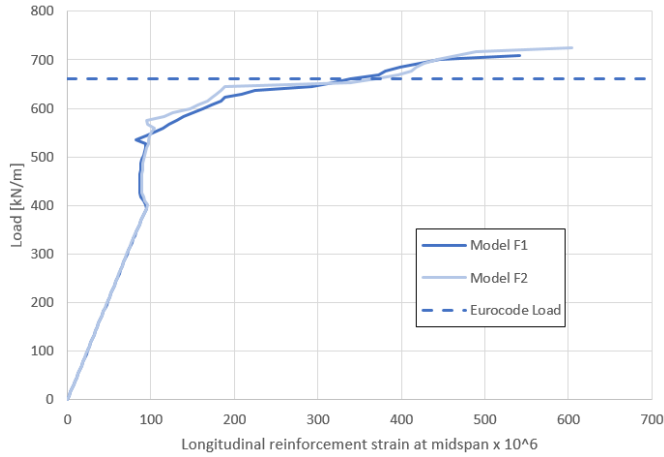


Figure 6.5.2: Longitudinal reinforcement strain of model F1 and F2 (yield strain = 2392.5×10^{-6})

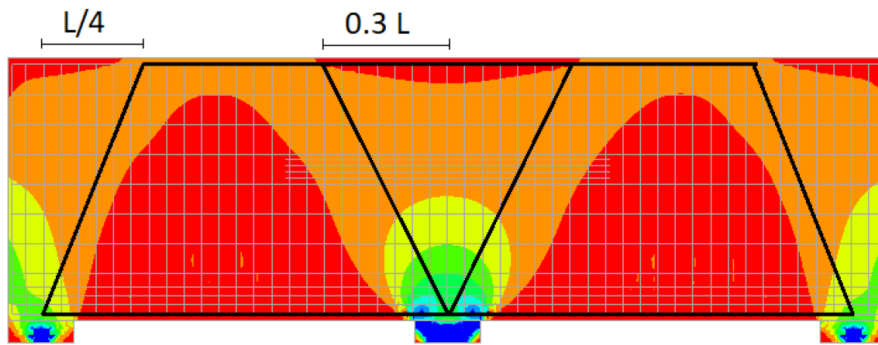


Figure 6.5.3: Concrete compressive stresses (S_2) at last load step before failure for wall model F1

In order to fulfill the conditions above, a new strut-and-tie model is introduced. This strut-and-tie model is based on the ratio between the support reaction of the intermediate and the outer support. As is observed in Figure 6.5.1, this ratio is constant for most of the load steps and independent of the reinforcement design (Same value for model F1 and F2). A numerical analysis is done for the same wall without any reinforcement, the ratio between the support reaction turned out to be the same as was computed with model F1 and F2. Subsequently this analysis is performed for multiple spans, where the height of the wall is kept constant. The ratio between the intermediate support reaction and the outer support reaction is defined as parameter a . The parameters a for the various models (with different h/l ratio) are presented in Table 6.5.1. These parameters are subsequently plotted against the h/l ratio, a trendline is made of which the formula is used to compute the a value. This is presented in Figure 6.5.5.

The strut-and-tie model that is used is presented in Figure 6.5.4. The angles of the struts are based on the compressive stresses contour plot that is presented in Figure 6.5.3. The analytical and numerical calculation using this alternative strut-and-tie model are presented in Appendix D.

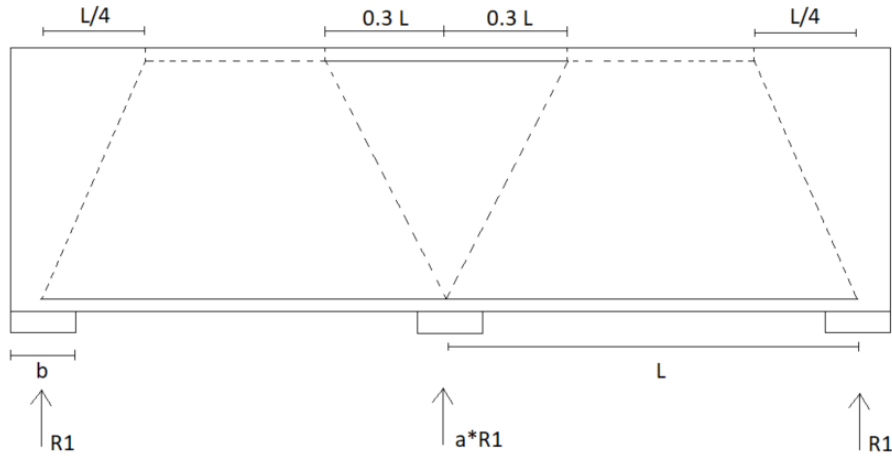


Figure 6.5.4: Alternative strut-and-tie model continuous wall

Table 6.5.1: Ratio between intermediate and outer support reaction

h/l	a
0.6	2.3967
0.65	2.3115
0.7	2.1380
0.8	2.0734
0.89	1.9506
1	1.8324
1.1	1.7341
1.2	1.6625
1.3	1.6043
1.41	1.5428

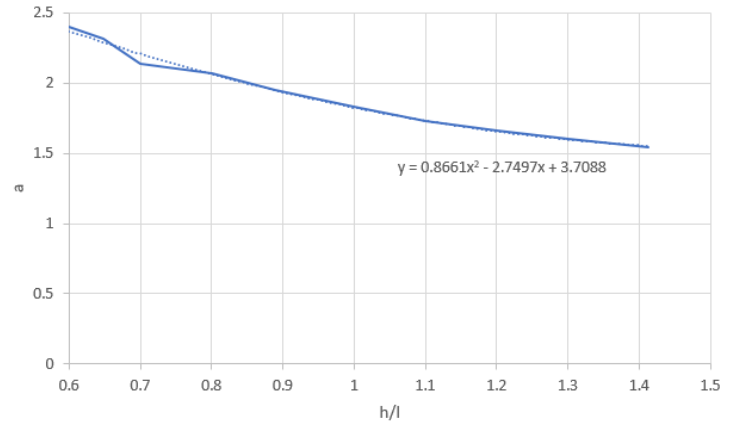


Figure 6.5.5: Ratio between intermediate and outer support reaction

In Figure 6.5.6, the Load-deflection curve for the numerical model F1 and the model that is designed using the new strut-and-tie model is presented. It is observed that the capacity of the new model is lower than model F1. However, the amount of main reinforcement and top reinforcement is significantly lower for the new model. Besides that, the numerical capacity is still significantly higher than the analytical load. The load-deflection curve shows that the new model behaves more ductile than model F1. This is preferred for a structural element, as the element now gives a 'warning' before failure through deflections.

The longitudinal reinforcement strain is plotted against the load for model F1 and the new model in Figure 6.5.7. It can be concluded from the graph that regarding the main reinforcement, the new model provides a better design. The strains of the main reinforcement are significantly higher, and the bars yield before failure.

Besides the two benefits of the new model that are described above, it also gives a better distribution of the support reactions (as the model is based on this distribution). This makes sure that the nodes above the supports are designed properly, using the correct stresses on the nodes.

The numerical capacity of the new model is 20 % higher than the analytical capacity. The main reinforcement ratio reduces from 0.52 % for model F1 to 0.115 % for the new model.

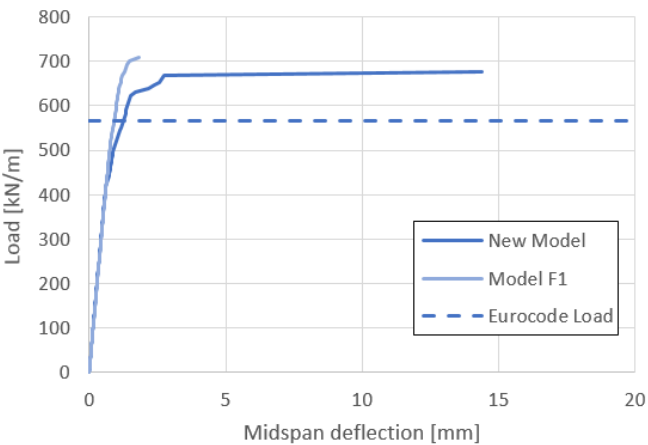


Figure 6.5.6: Load-Deflection curve of the new model and model F1

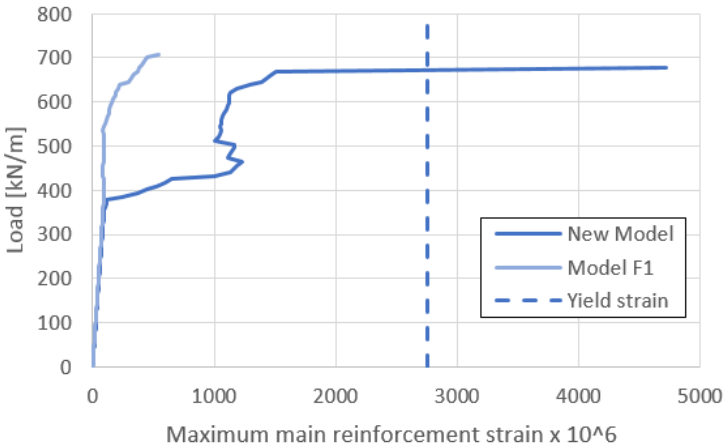


Figure 6.5.7: Load-Strain curve of the new model and model F1

7 Conclusions and recommendations

7.1 Conclusions

To achieve the goals that were set for this research, a literature review is done on the strut-and-tie method and the Eurocode verifications that are applicable for this method, the finite element method and previous researches that are relevant for this report. From the literature review it was concluded that the Eurocode lacks clarity for some of the strut-and-tie verifications (web reinforcement, crack width and nodes). Based on the information that was found in the literature review, the constitutive models for finite element modelling are composed and the model is verified using previous researches. Subsequently six pile caps models with a span of 1300 mm are analysed with both the strut-and-tie model and a finite element analysis. It contains pile cap models A, B and C with depths of 720, 1080 and 1300 mm respectively. Of each of these three models, two web reinforcement designs are analysed. One based on the requirement of the Eurocode for deep beams and one based on the forces in the struts. Six wall girder models are analysed with a length of 10 m each, of which 2 continuous (model F) and four simply supported. Two simply supported models represent a wall for a single floor with a height of 3 m (model D) and two models contain a height of 6 m (model E). Besides the height, model D and E are identical. Two different reinforcement designs are analysed for each wall. The geometry of pile cap model A and wall girder models D and F are presented in Figure 7.1.1, 7.1.2 and 7.1.3 respectively

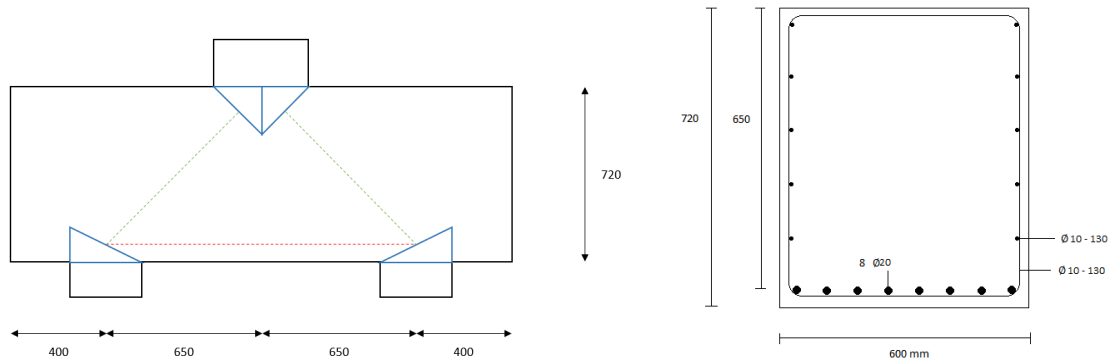


Figure 7.1.1: Geometry of pile cap model A1 (Model A2 contains less web reinforcement)

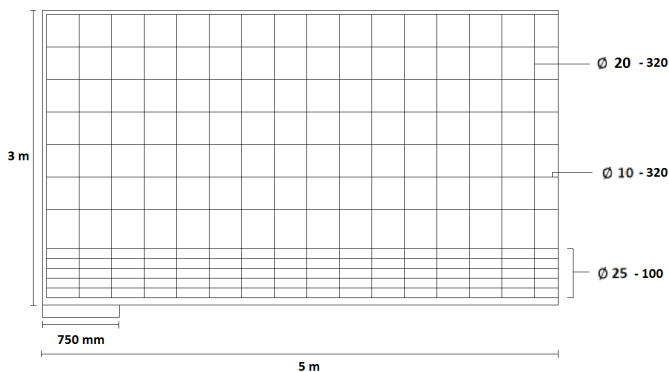


Figure 7.1.2: Geometry and reinforcement of half of wall girder model D1 (For model D2 additional reinforcement is applied above the supports)

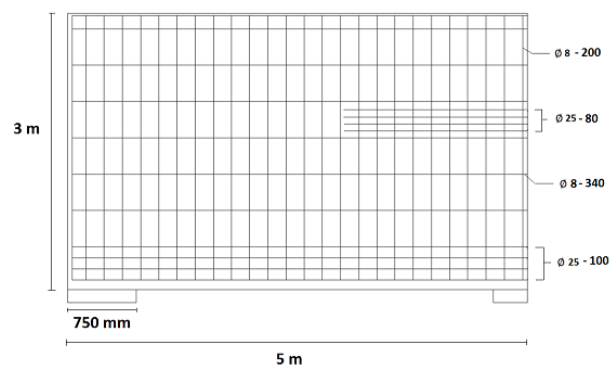


Figure 7.1.3: Geometry and reinforcement of half of wall girder model F1 (Model F2 contains no upper tensile tie, this reinforcement is spread out over the web reinforcement)

Referring to the goals that were set for this research, it can be concluded that the reinforcement design of the structural elements can be optimized. For the pile cap it is observed that the crack width verification is often the determining criterion for the main reinforcement. It is concluded that the steel stress calculation for crack width using the strut-and-tie model is preferred for the pile caps as the position and direction of the struts is assumed correctly, which is the requirement that is given in the Eurocode for the application of the method. On the contrary, the internal lever arm for the elastic approach underestimates the numerically found lever arm when the pile cap becomes 'deeper' and the stresses in the cross-section that were found numerically do not represent a cross-section in bending. This appears to reduce the steel stress more when the pile cap becomes 'deeper'. For model B and C a decrease in steel stress of 27 % and 34 % respectively were found, for model A the steel stress appeared to be equal for both methods (e.g. strut-and-tie model and sectional approach).

Using only the numerical results, the conclusion would be that the web reinforcement can be based on the force in the strut and therefore reduced compared to the deep beam requirement for the web reinforcement by the Eurocode. The diagonal cracks that lead to failure for model B and C are namely initiated at a load level that is 10 % and 30 % above the analytical capacity respectively. The decrease in capacity is limited, 2.6 % and 0.4 % for a decrease in horizontal web reinforcement amount from 0.19 % to 0.10 % and 0.18 % to 0.08 % for model B and C respectively. However, the diagonal cracks that are formed are significant. Therefore, the additional web reinforcement requirement might be useful to prevent this from happening. Further experimental research should reveal if this web reinforcement requirement is actually necessary for pile caps.

For the continuous wall girder, a strut-and-tie model is composed in this research (by making use of nonlinear finite element results) that shows an optimized design compared to the strut-and-tie model that was found in literature and was initially used in the calculation. The new strut-and-tie model results in an optimized design in terms of amount of longitudinal reinforcement (a reduction from 0.52 % to 0.115 %) and behaviour of the wall before failure, the failure is more ductile and provides a 'warning' before failure. A deflection of 14 mm before failure is observed for the new model, compared to 2 mm for the initial model. The numerical capacity of this new model is 20 % higher than the analytical capacity.

A secondary goal was to create calculation sheets that can be used in practice. In the analyses the analytical calculations were made by making use of Microsoft Excel. These sheets are presented in the appendices. As is mentioned in this report, a few challenges are present when performing a strut-and-tie model calculation. For example, the node dimensioning of the CCC node. A suitable equation for this node dimensioning is derived in this report. Using this, including the other conclusions that are drawn in this report, calculation sheets for the regarding structural elements are successfully created that can be used in practice.

7.2 Recommendations

This paragraph contains recommendations for further research and development related to this thesis.

7.2.1 Adding an experimental research to the numerical research on the diagonal cracking behaviour of reinforced concrete pile caps.

In this thesis it was found that diagonal cracking is the most common failure mode for two pile caps, especially when the pile cap becomes 'deeper'. The Eurocode provides a calculation for the tension force that originate perpendicular to the strut (diagonal splitting forces). On top of this, the Eurocode also provides a minimum amount of web reinforcement that is applicable for deep beams. In case of the pile caps, the latter requirement appears to be decisive in many cases. If this additional reinforcement, compared to the reinforcement that follows from a calculation of the actual forces, is necessary would be interesting to examine. This is not only applicable for pile caps, but for deep beams in general.

7.2.2 Further research on the behaviour of reinforced concrete wall girders or deep beams on three supports.

In this report it was not the main goal to investigate the behaviour of reinforced concrete wall girders on three supports. However, in finding an appropriate strut-and-tie model a few challenges were found. The distribution of the support reactions and the angle of the struts that determine the longitudinal reinforcement in the wall girder are crucial in composing an appropriate strut-and-tie model. A good model is composed in this research for the dimensions that are used in this report. It would however be interesting to further investigate the behaviour of continuous wall girders and considering a wider range of dimensions.

References

- [1] Abdul-Hameed, S. D. "Experimental and analytical investigation for strength prediction of reinforced concrete pile caps using strut-and-tie model", PhD Thesis, University of Al-Nahrain, Baghdad, Iraq, 2015.
- [2] Abdul-Razzaq, K. S., & Farhood, M. A. Design-Oriented Testing and Modeling of Reinforced Concrete Pile Caps. *KSCE Journal of Civil Engineering*, 23(8), pp 3509–3524, 2019. <https://doi.org/10.1007/s12205-019-1650-5>
- [3] Adebar, P., Kuchma, D. and Micheal P. Collins, "strut-and-tie Models for the design of pile caps: an experimental study", *ACI Structural Journal*, Vol. 87, No. 1, pp 81-92, 1990.
- [4] Adebar, P. and Zhou, L. "Design of Deep Pile Caps by Strut-and-Tie Models", *ACI Structural Journal*, Vol. 93, No. 4, pp 1-11, 1996.
- [5] Alfrink, L.J. "Geavanceerde staafwerkmodellen", Master Thesis, Eindhoven University of Technology, 2015
- [6] Bhattarai, S. "Reliability Analysis and safety assessments of structural wall with nonlinear finite element analyses", Master Thesis, Delft University of Technology, 2017.
- [7] Blauwendraad, J. "Wandliggers op 3 steunpunten". *Cement*, 2012/7, pp 64-67, 2012.
- [8] Deutsch, G. P. and Walker, D. N. O. "Pile Caps", Civil Engineering Research Project, University of Melbourne, 1963.
- [9] *fib* Model Code 2010. *fib* Bulletins 65 and 66, International Federation for Structural Concrete (*fib*), 2012.
- [10] Hendriks, M. A. N. and Roosen, M. A. (editors), "Guidelines for Nonlinear Finite Element Analysis of Concrete Structures", Rijkswaterstaat Centre for Infrastructure, Report RTD:1016-1:2019, 2019.
- [11] Ismail, K. S., Guadagnini, M. and Pilakoutas, K. "Strut-and-Tie Modeling of Reinforced Concrete Deep Beams", *Journal of Structural Engineering*, Vol. 144, No. 2, 04017216, 2017.
- [12] Mörsch, E. "Der Eisenbetonbau, seine Theorie und Anwendung (Reinforced Concrete, Theory and Application)", Konrad Wittwer, 3th edition, Stuttgart, 1908.
- [13] NEN-EN 1922-1-1 (Eurocode 2: Design of concrete structures – Part 1-1: General rules and rules for buildings), 2011.
- [14] NEN 6720 Regulations for concrete- structural requirements and calculation methods (VBC 1995), 1995.
- [15] Nirmalsingh, R.S.J.L. "FEM Analysis of the cracking behaviour of a beam subjected to bending: A discrete crack width calculation using DIANA", Master Thesis, Delft University of Technology, 2016.
- [16] Ritter, K. W. "Die Bauweise Hennebique (The Hennebique System), vl.33. Schweiz Bauzeitung", Stuttgart: Verlag Konrad Wittwer, 1899.

- [17] Schlaich, J. and Schläfer, K. "Design and detailing of structural concrete using strut-and-tie models", 1991.
- [18] Schalich, J., Schläfer, K. and Jennewein, M. "Toward a Consistent Design of Structural Concrete", *PCI Journal*, Vol. 32, No. 3, pp 74-150, 1987.
- [19] Structural Engineering Department, TKT4222 Concrete Structures 3 Compendium, Norwegian University of Science and Technology, 2014.
- [20] Subedi, N.K., Vardy, A. E. and Kuboa, N. "Reinforced concrete deep beams- some test results", *Magazine of Concrete Research*, Vol. 38, No. 137, 1986.
- [21] Sugianto, A. "Evaluating strut-and-tie models for concrete elements by nonlinear finite element analysis", Master Thesis, Delft University of Technology, 2019.
- [22] Tjhin, T. N. & Kuchma, D. A. (2002). Computer-based tools for design by strut-and-tie method: Advances and challenges. *ACI Structural Journal*, 99(5), pp 586-594.
- [23] VB 1974/1984, 1984.
- [24] Yang, K. H. and Ashour, A. F. "Load Capacity of Reinforced Concrete Continuous Deep Beams", *Journal of Structural Engineering*, Vol. 134, No. 6, pp 919-929, June 2008.

Appendix A1: Excel sheet of Eurocode calculation pile cap model A

Hoogte van de poer	720	mm	Kolom vorm		Rechthoekig	Paal vorm		Rechthoekig	Eigenschappen Beton	
Breedte van de poer	600	mm	Kolom breedte	400	mm	Paal afmeting	300	mm	sterkteklasse	C30/37
overspanning van de poer	1300	mm	equivalente breedte	400	mm	fck	30	MPa		
overspanning van de poer met paalmisstand	1300	mm	Kolom diepte	450	mm	fcd	20,0	MPa		
afstand van paal tot zijkant van de poer	400	mm				fctm	2,9	MPa		
afstand van paal tot zijkant van de poer met totale lengte van de poer	2100	mm				Ectm	32800	MPa		
afstand van paal tot het midden van de poer	650	mm				fctk;0.05	2,0	MPa		

Belasting	
UGT	1950 kN
BGT	1300 kN

Duurzaamheid	
Ontwerplevensduur	50 jaar
Milieuklasse	XC2/XC3
Constructieve classificatie	S4
c _{min,dur}	25 mm
minimale dekking	35 mm
toegepaste dekking onder	50 mm
toegepaste dekking boven	40 mm
toegepaste dekking zijkant	25 mm
mazimale scheurvrijde	0,3 mm

Wapening						
Aantal lagen onderwapening	1					
Afstand tussen laag 1 en 2	0 mm					
nuttige hoogte	650 mm					
	n	s	d	Betonstaal	fyk	fjd
Hooftwapening laag 1	8	20	72,3	B500	500	435
Hooftwapening laag 2	0	0	0	B500	500	435
Flankwapening horizontaal (-	10	130	B500	500	435
Flankwapening verticaal (be	-	10	130	B500	500	435

Unity checks	
Wapening	
Hooftwapening	0,89
scheurvrijde	0,82
horizontale flankwapening	0,99
verticale flankwapening	0,99
Knopen	
Drukvak kolom	0,62
Drukvak paal	0,72
Drukvak paal diagonaal	0,99

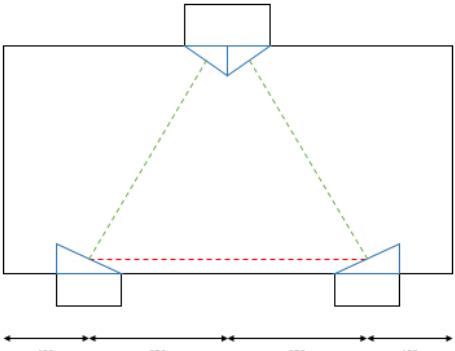
Paalknoop		Kolomknoop	
a1	300 mm	0,5*a1	200 mm
u	140 mm	a0	200 mm
a2	311,1 mm	a2	283 mm
k2	0,85	v'	0,88
sigma,max	15,0 MPa	k1	1
sigma1	10,8 MPa	sigma,max	17,6 MPa
sigma2	14,8 MPa	sigma	10,8 MPa

Hoofdwapening		Flankwapening	
As	2513,3 mm ²	As,hor	604,1524 mm ² /m per zijde
Fs	975,0 kN	As,ver	604,1524 mm ² /m per zijde
sigmas	387,9 MPa	H	2074,25 mm
		h	1037,12 mm

Scheurvrijde			
z	548 mm	a	282,84 mm
sigmas	253,6 MPa	b,eff	1220,97 mm
kt	0,4	alpha	45,0 graden
ho,eff	175 mm	F	1378,9 kN
Ac,eff	105000 mm ²	T	278,9 kN
rho,eff	0,02394	Thor	197,2 kN
d/g	6,098	Tver	197,2 kN
epsilon _{sm} - epsilon _{cm}	0,00102	As,min	600 mm ² /m per zijde
k1	0,8	As,min,hor	600 mm ² /m per zijde
k2	0,5	As,min,ver	600 mm ² /m per zijde
k3	3,4		
k4	0,425		
o	60 mm		
sr,max	346,05 mm		
wk	0,35 mm		
ks	1,43		
wmax	0,43 mm		

Appendix A2: Excel sheet of Eurocode calculation pile cap model B

Hoogte van de poer	1080	mm	Kolom vorm	Rechthoekig	Paal vorm	Rechthoekig	Eigenschappen Beton	
Breedte van de poer	600	mm	Kolom breedte	400	mm	Paal afmeting	300	mm
overspanning van de poer	1300	mm	equivalente breedte	400	mm	Paal diepte	300	mm
afstand van paal tot zijkant van de poer met paalmisstand	400	mm	Kolom diepte	450	mm	Paalmisstand	0	%
afstand van paal tot zijkant van de poer met	400	mm						
totale lengte van de poer	2100	mm						
afstand van paal tot het midden van de poer	650	mm						



1080

400 650 650 400

Belasting	
UGT	2450 kN
BGT	1633 kN

Duurzaamheid	
Ontwerplevensduur	50 jaar
Milieuklasse	XC2/MC3
Constructieve classificatie	S4
emin,dur	25 mm
minimale dekking	35 mm
toegepaste dekking onder	50 mm
toegepaste dekking boven	40 mm
toegepaste dekking zijkant	25 mm
maximale scheurwijdte	0,3 mm

Wapening	
Aantal lagen onderwapening	1
Afstand tussen laag 1 en 2	0
nuttige hoogte	1010

n	Ø	s	Betonstaal	f _{yk}	f _{yd}
7	20	85	B500	500	435
0	0	0	B500	500	435
-	10	130	B500	500	435
-	10	130	B500	500	435

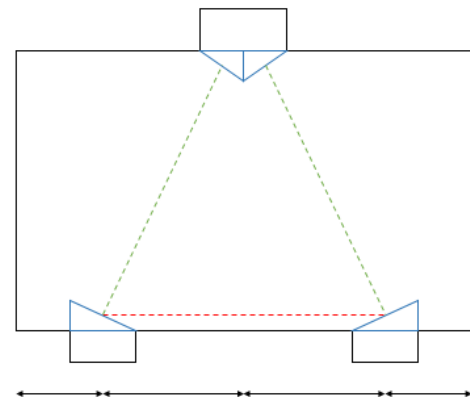
Unity checks	
Wapening	
Hoofdwapening	0,74
scheurwijdte	0,99
horizontale flankwapening	0,99
verticale flankwapening	0,99
Knopen	
Drukvak kolom	0,77
Drukvak paal	0,91
Drukvak paal diagonaal	0,96

Paalknoop		Kolomknop	
a1	300 mm	0,5*a1	200 mm
u	140 mm	a0	116 mm
a2	329,8 mm	a2	231 mm
k2	0,85	v'	0,88
sigma,max	15,0 MPa	k1	1
sigma1	13,6 MPa	sigma,max	17,6 MPa
sigma2	14,3 MPa	sigma	13,6 MPa

Hoofdwapening		Flankwapening	
A _s	2193,1 mm ²	A _{s,hor}	604,1524 mm ² m per zijde
F _s	707,5 kN	A _{s,ver}	604,1524 mm ² m per zijde
sigma _s	321,7 MPa	H	2216,12 mm
Scheurwijdte		h	1107,56 mm
z	632 mm	a	230,96 mm
sigma _s	295,1 MPa	b,eff	1257,69 mm
kt	0,4	alfa	60,0 graden
h _{c,eff}	175 mm	F	1414,7 kN
A _{c,eff}	105000 mm ²	T	302,0 kN
ρ _{eff}	0,02034	Thor	261,5 kN
α _g	6,098	Tver	151,1 kN
ε _{sm} - ε _{cm}	0,00116	A _{s,min}	600 mm ² m per zijde
k1	0,8	A _{s,min,hor}	600 mm ² m per zijde
k2	0,5	A _{s,min,ver}	600 mm ² m per zijde
k3	3,4		
k4	0,425		
c	60 mm		
st,max	366,34 mm		
w _k	0,43 mm		
k _s	1,43		
w _{max}	0,43 mm		

Appendix A3: Excel sheet of Eurocode calculation pile cap model C

Hoogte van de poer		1300	mm	Kolom vorm	Rechthoekig	Paal vorm	Rechteoekig	Eigenschappen Beton	sterkteklasse	C30/37
Breedte van de poer		600	mm	Kolom breedte	400	mm	Paal afmeting	300	mm	30
overspanning van de poer		1300	mm	equivalente breedte	400	mm	equivalente breedte	300	mm	MPa
overspanning van de poer met paalstand		1300	mm	Kolom diepte	450	mm	Paal diepte	300	mm	20,0
afstand van paal tot zijkant van de poer		400	mm				Paalstand	0	%	2,9
afstand van paal tot zijkant van de poer met		400	mm							32800
totale lengte van de poer		2100	mm							2,0
afstand van paal tot het midden van de poer		650	mm							MPa



1300

650

650

400

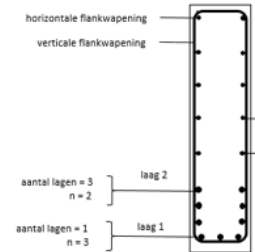
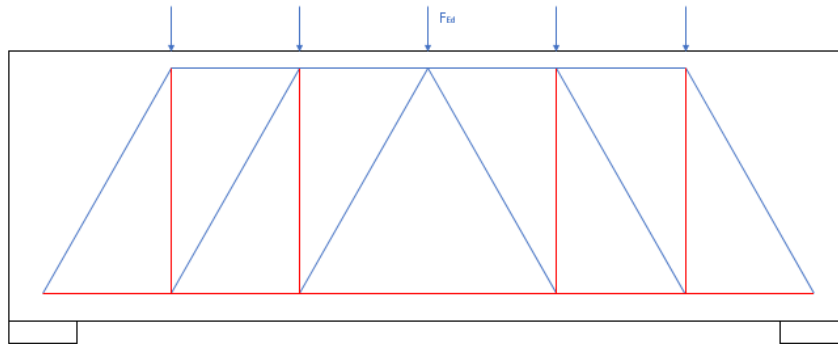
400

Duurzaamheid		Wapening	
Ontwerplevensduur	50 jaar	Aantal lagen onderwapening	1
Milieuklasse	XC2/MC3	Afstand tussen laag 1 en 2	0
Constructieve classificatie	S4	nuttige hoogte	1230
c _{min,dur}	25 mm		
minimale dekking	35 mm		
toegepaste dekking onder	50 mm		
toegepaste dekking boven	40 mm		
toegepaste dekking zijkant	25 mm		
maximale scheurwijde	0,3 mm		

Wapening		Scheurwijde	
z	780 mm	σ _s	277,8 MPa
σ _s	277,8 MPa	κ _t	0,4
κ _t	0,4	h _{o,eff}	175 mm
h _{o,eff}	175 mm	A _{c,eff}	105000 mm ²
A _{c,eff}	105000 mm ²	ρ _{eff}	0,02094
ρ _{eff}	0,02094	α _{lg}	6,098
α _{lg}	6,098	ε _{cm} - ε _{cm}	0,00108
ε _{cm} - ε _{cm}	0,00108	k ₁	0,8
k ₁	0,8	k ₂	0,5
k ₂	0,5	k ₃	3,4
k ₃	3,4	k ₄	0,425
k ₄	0,425	c	60 mm
c	60 mm	s _{r,max}	366,34 mm
s _{r,max}	366,34 mm	vk	0,33 mm
vk	0,33 mm	k _z	143
k _z	143	w _{max}	0,43 mm
w _{max}	0,43 mm		

Unity checks	
Wapening	
Hoofdwapening	0,63
scheurwijde	0,32
horizontale flankwapening	0,39
verticale flankwapening	0,39
Knopen	
Drukvlak kolom	0,82
Drukvlak paal	0,97
Drukvlak paal diagonaal	0,96

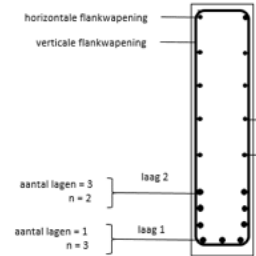
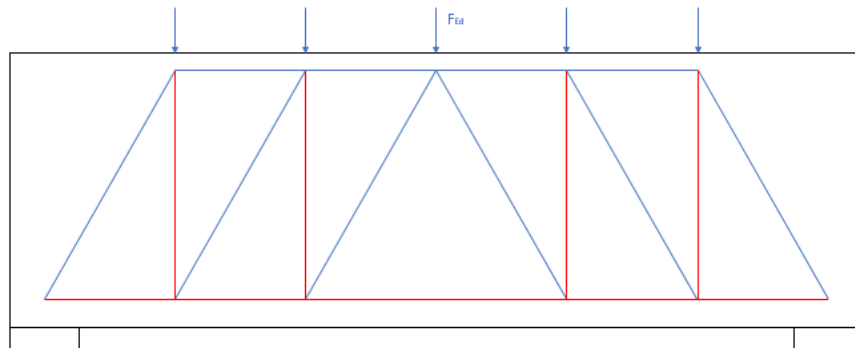
Appendix A4: Excel sheet of Eurocode calculation wall girder model D



Voorbeeld staafwerkmodel en wapening in doorsnede

Staadwerkmodel			Hoofdwapening ULS			Unity checks			Belasting			Eigenschappen Beton		
maximale hoek drukdiagonalen	68	graden	A _s	6381,4	mm ²	Knoop boven oplegging links	0,98		UGT	550,0	kN/m	Sterkteklasse	C30/37	
minimale hoek drukdiagonalen	45	graden	F _s (ULS)	2724,6	kN	Knoop boven oplegging rechts	0,98		BGT	366,7	kN/m	f _{ck}	30	MPa
Afstand tussen onder- en bovenwapening	2667,5	mm	sigmas	427,0	MPa	Hoofdwapening ULS	0,98					f _{td}	20,0	MPa
minimale afstand trekstaven	1078	mm				Scheurwijde	0,75					f _{ctm}	2,9	MPa
aantal diagonalen per halve wand	4					Flankwapening horizontaal	0,99					E _{ctm}	32800	MPa
hoek drukdiagonalen	66,6	graden	Scheurwijde			Flankwapening verticaal	0,99							
F _{ed}	786,7	kN	z	2667,5	mm									
Kracht in middelste drukdiagonalen	428	kN (druk)	F _s (SLS)	1470,3	kN									
Kracht in buitenste drukdiagonalen	2397,2	kN (druk)	sigmas	230,4	MPa									
Horizontale component drukdiagonalen	170	kN	kt	0,4										
Grootste kracht in onderwapening	2725	kN (trek)	h _{o,eff}	668,8	mm									
Kracht in middelste verticale trekstaven	392,3	kN (trek)	A _{o,eff}	167188	mm ²									
Som van krachten in alle verticale trekstaven	7071,4	kN (trek)	rho _{eff}	0,038										
Som van krachten in alle drukdiagonalen	13701,6	kN (druk)	alfaE	6,098										
			ε _{cm} - ε _{cm}	0,001233										

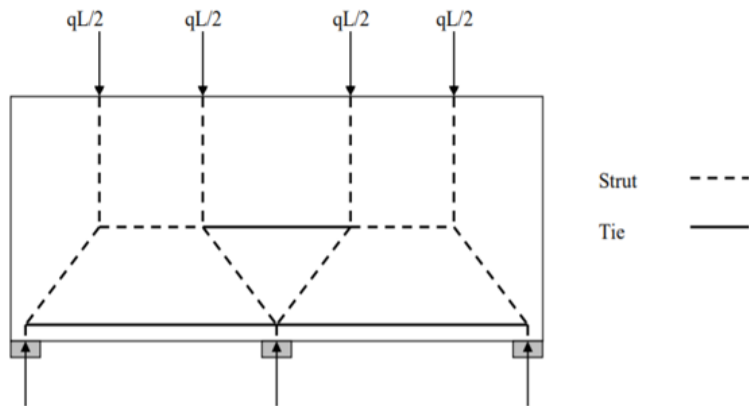
Appendix A5: Excel sheet of Eurocode calculation wall girder model E



Voorbeeld staafwerkmodel en wapening in doorsnede

Staaftwerkmodel				Hoofdwapening ULS				Unity checks				Belasting				Eigenschappen Beton			
maximale hoek drukdiagonalen	68	graden		As	3455,8	mm ²		Knoop boven oplegging links	0,98			UGT	550,0	kN/m		Sterkteklasse	C30/37		
minimale hoek drukdiagonalen	45	graden		Fs (ULS)	1483,4	kN		Knoop boven oplegging rechts	0,98			BGT	366,7	kN/m		fok	30	MPa	
Afstand tussen onder- en bovenwapening	5716	mm		sigmas	429,3	MPa		Hoofdwapening ULS	0,99							fod	20,0	MPa	
minimale afstand trekstaven	2309	mm						Scheurwijdte	0,66							fotm	2,9	MPa	
aantal diagonalen per halve wand	2							Flankwapening horizontaal	0,99							Eotm	32800	MPa	
hoek drukdiagonalen	68,0	graden						Flankwapening verticaal	0,99										
Fed	1833,3	kN		z	4250	mm													
Kracht in middelste drukdiagonalen	989	kN	(druk)	Fs (SLS)	922,8	kN													
Kracht in buitenste drukdiagonalen	2968,5	kN	(druk)	sigmas	267,0	MPa													
Horizontale component drukdiagonalen	371	kN		kt	0,4														
Grootste kracht in onderwapening	1483	kN	(trek)	ho,eff	570,0	mm													
kracht in middelste verticale trekstaven	916,7	kN	(trek)	Ac,eff	142500	mm ²													
Som van krachten in alle verticale trekstaven	1833,3	kN	(trek)	rho,eff	0,024														
Som van krachten in alle drukdiagonalen	7910,7	kN	(druk)	alfaE	6,098														
				ε _{ym} = ε _{cm}	0,001258														

Appendix A6: Excel sheet of Eurocode calculation model F



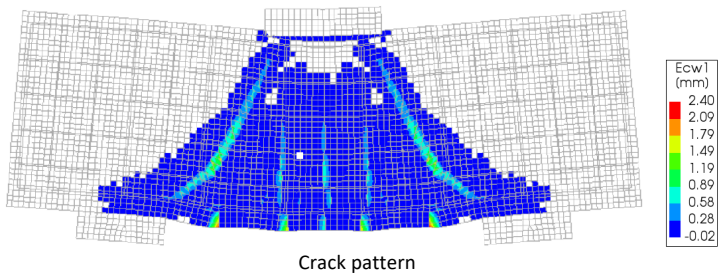
Staafwerkmodel				Hoofdwapening ULS				Unity checks			
qL/2	Links 1526	Rechts 1526	kN	As	3927,0	mm ²		Knoop boven oplegging links	0,74		
Hoogte bovenste trekband	1721		mm	Fs (ULS)	1526,3	kN		Knoop boven oplegging rechts	0,74		
Hoek diagonalen	45	45	graden	sigmas	388,7	MPa		Knoop tussen steunpunt	0,99		
Kracht in drukdiagonalen	2158	2158	kN	Scheurwijdte				Hoofdwapening ULS	0,89		
Kracht in onderste trekband	1526	1526	kN	Fs (SLS)	1017,5	kN		Scheurwijdte	0,76		
Kracht in bovenste trekband	1526		kN	sigmas	259,1	MPa		Flankw apening horizontaal	0,99		
				kt	0,4			Flankw apening verticaal	0,99		
Knoop boven buitenste oplegging				ho,eff	448,8	mm		Wapening bovenste trekband	0,89		
a1	Links 750	Rechts 750	mm	Ac,eff	112188	mm ²					
u	359	359	mm	rho,eff	0,035						
a2	784,2	784,2	mm	alfaE	6,098						
k2		0,85		ε _{cm} - ε _{cm}	0,001371						
v'		0,88		k1	0,8						
sigma,max	15,0		MPa	k2	0,5						
sigma1	8,1	8,1	MPa	k3	3,4						
sigma2	11,0	11,0	MPa	k4	0,425						
				c	58	mm					

Afmetingen				Duurzaamheid			
Lengte van de wand	10	m		Ontwerplevensduur	50 jaar		
hoogte	3	m		Milieuklasse	XC1		
Lengte van het tussensteunpunt	750	mm		Constructieve classificatie	S4		
Lengte van het linker steunpunt	750	mm		o _{min,dur}	15	mm	
Lengte van het rechter steunpunt	750	mm		minimale dekking	35	mm	
Wand dikte	250	mm		toegepaste dekking onder	50	mm	
Linker overspanning	4,625	m		toegepaste dekking boven	45	mm	
Rechter overspanning	4,625	m		toegepaste dekking zijkant	40	mm	
Verschuif in steunpuntszetting	0	mm		maximale scheurwijdte	0,4	mm	

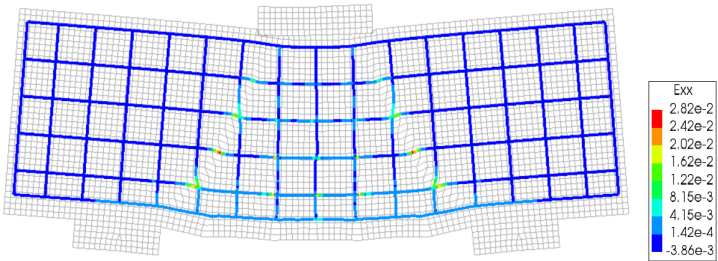
Wapening				Belasting			
Aantal lagen onderw apening	4			UGT	Links 660	Rechts 660	kN/m
Verticale afstand tussen lagen trekbandw apening	100		mm	BGT	440	440	kN/m
Nuttige hoogte	2820,5		mm	Eigenschappen Beton			
hoogte onderste trekband	370,5	mm	≤	Sterkteklasse	C30/37		
	Aantal lagen	n	Ø	f _{ck}	30	MPa	
Trekbandw apening onder laag 1	4	2	25	f _{cd}	20,0	MPa	
Trekbandw apening onder laag 2	0	2	25	f _{ctm}	2,9	MPa	
Flankw apening verticaal	-	-	8	E _{ctm}	32800	MPa	
Flankw apening horizontaal	-	-	8				
Bovenste trekband	4	2	25				

Appendix B: DIANA plots pile cap models

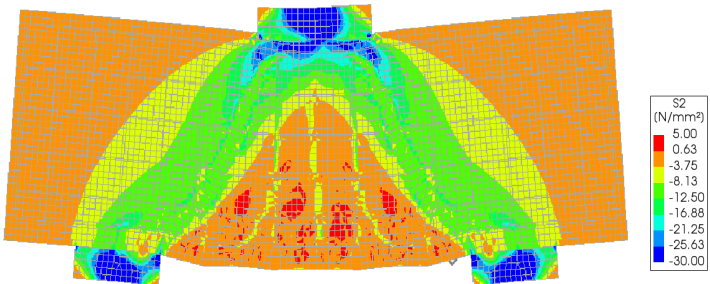
Model A1



Crack pattern

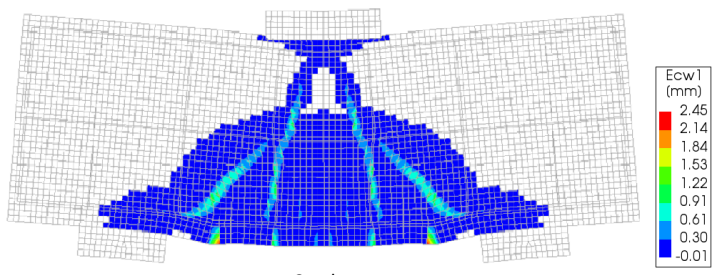


Reinforcement strains at last load step before failure

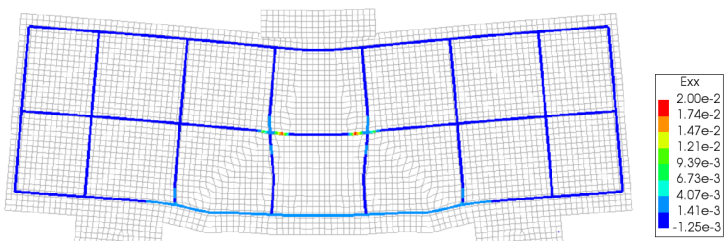


Concrete compressive stresses at last load step before failure

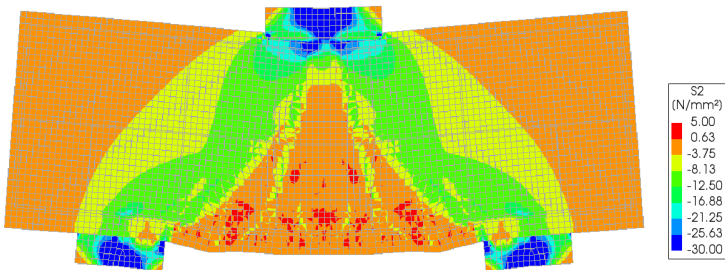
Model A2



Crack pattern

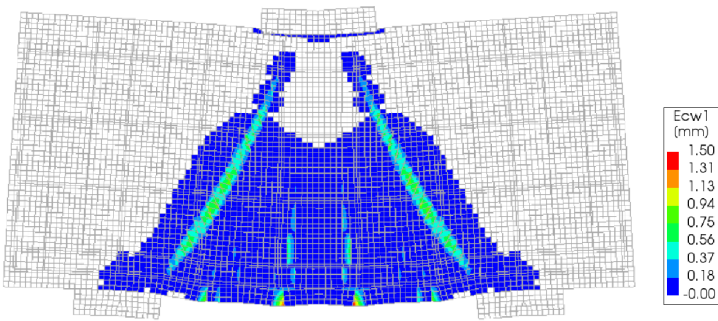


Reinforcement strains at last load step before failure

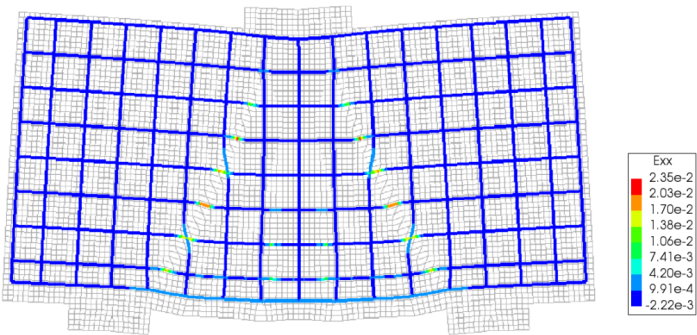


Concrete compressive stresses at last load step before failure

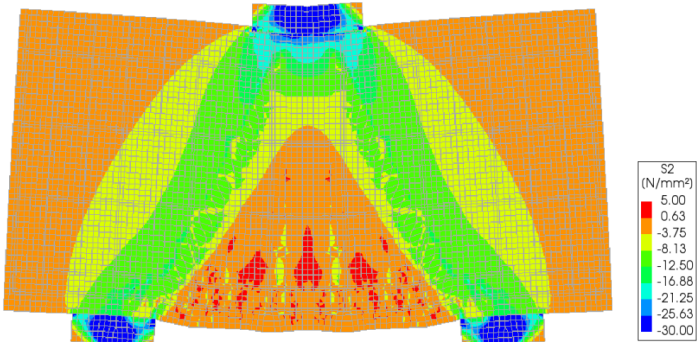
Model B1



Crack pattern

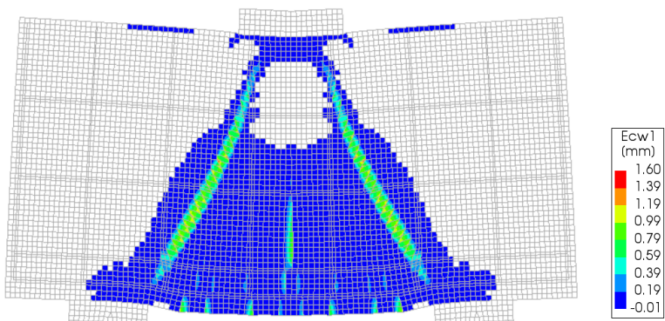


Reinforcement strains at last load step before failure

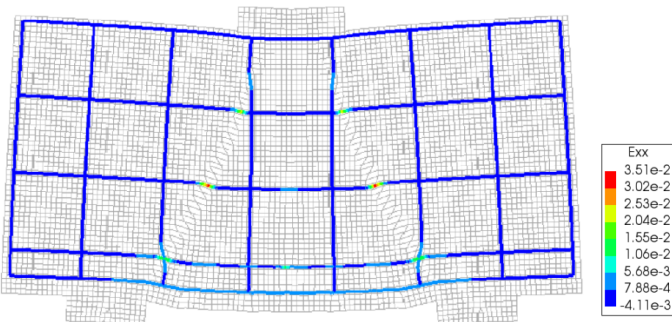


Principal concrete compressive stresses at last load step before failure

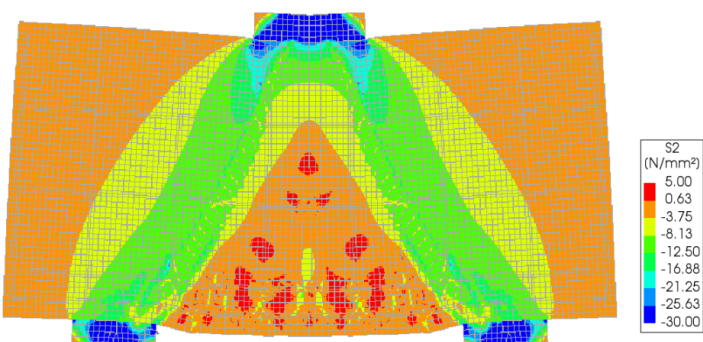
Model B2



Crack pattern



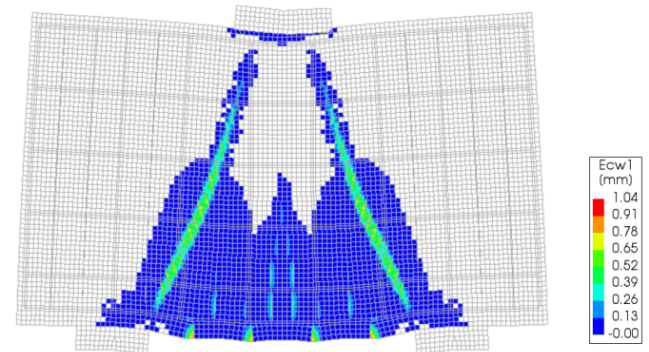
Reinforcement strains at last load step before failure



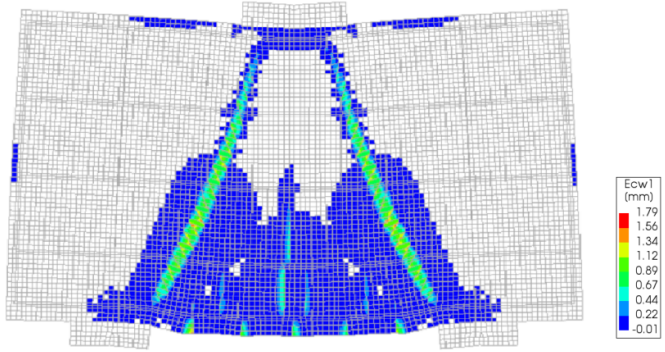
Principal concrete compressive stresses at last load step before failure

Model C1

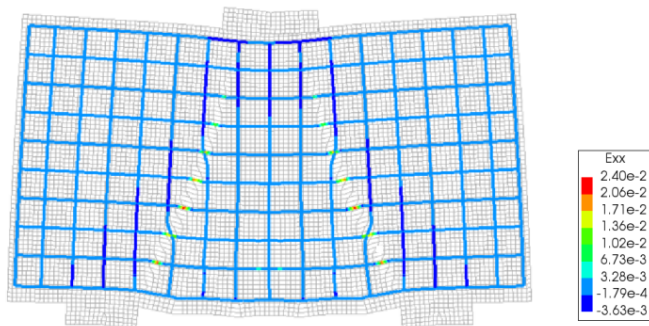
Model C2



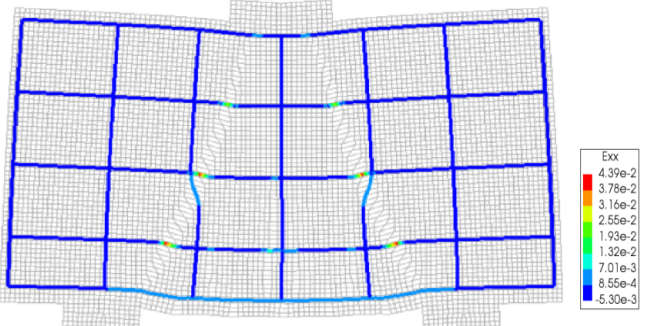
Crack pattern



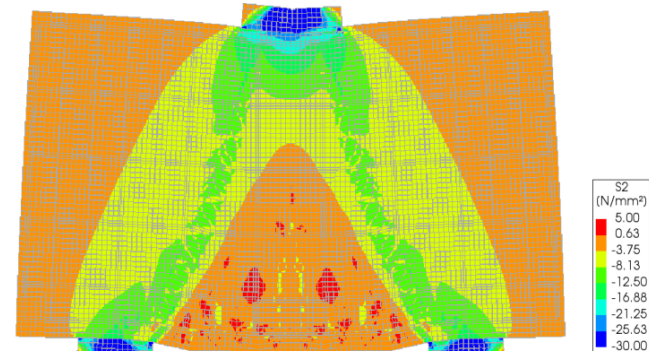
Crack pattern



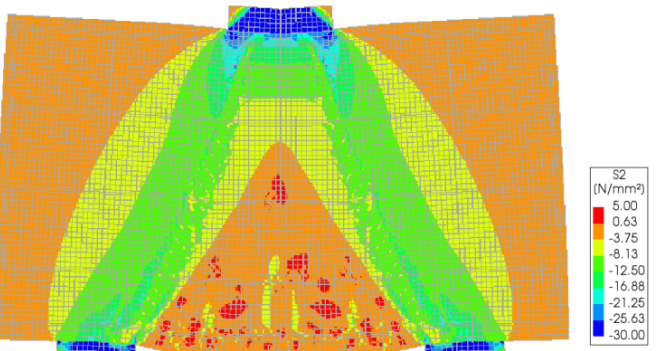
Reinforcement strains at last load step before failure



Reinforcement strains at last load step before failure



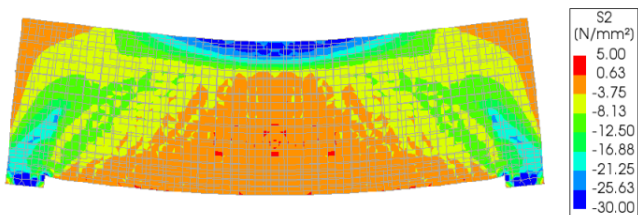
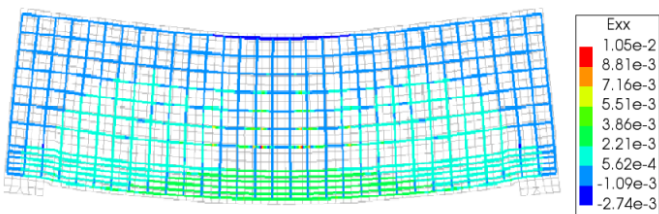
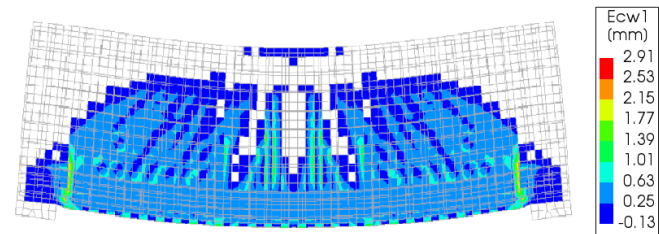
Principal concrete compressive stresses at last load step before failure



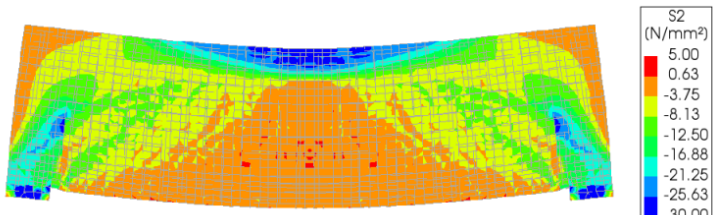
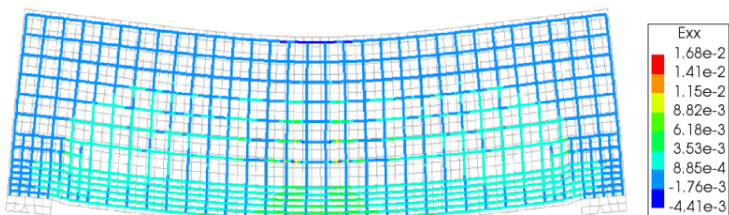
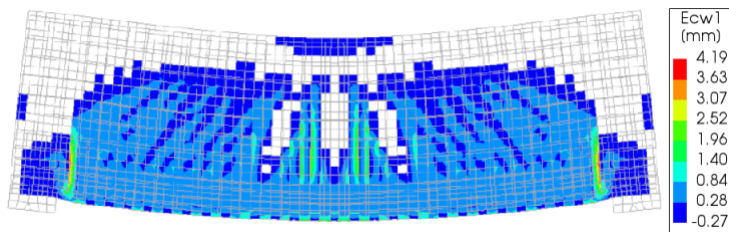
Principal concrete compressive stresses at last load step before failure

Appendix C: DIANA plots wall girder models

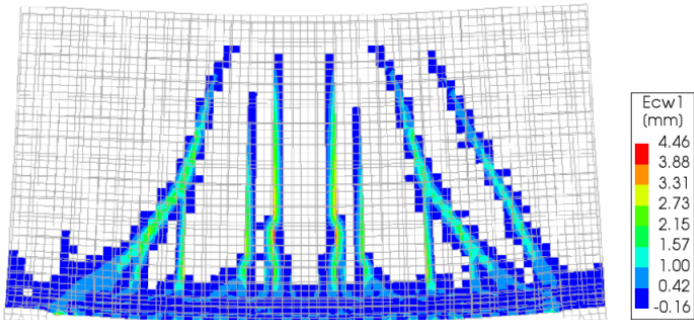
Model D1



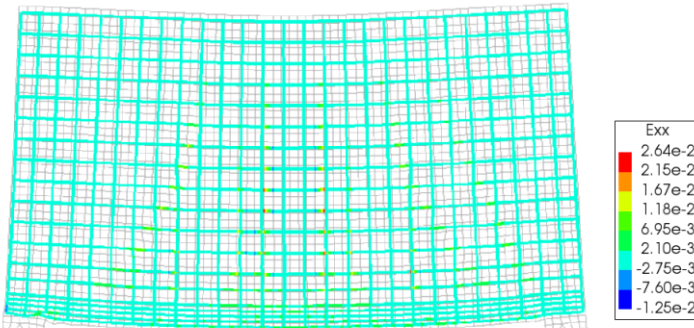
Model D2



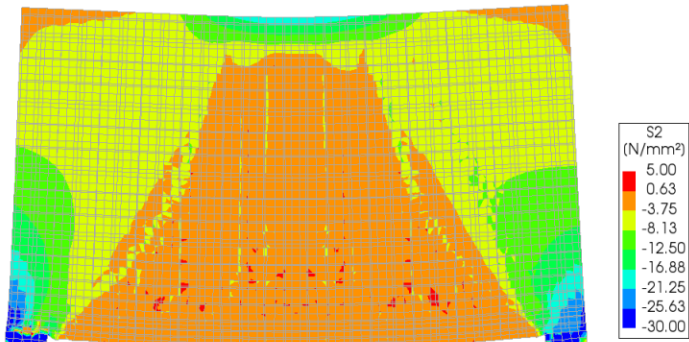
Model E1



Crack pattern

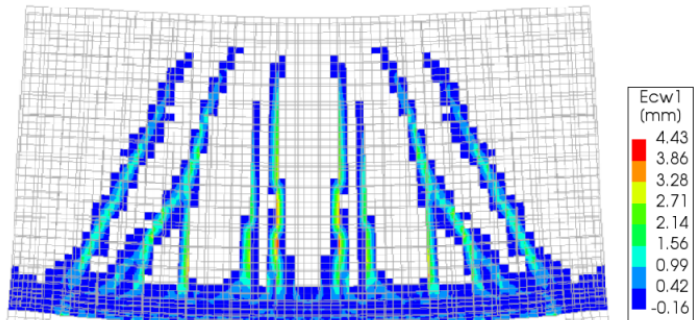


Reinforcement strains at last load step before failure

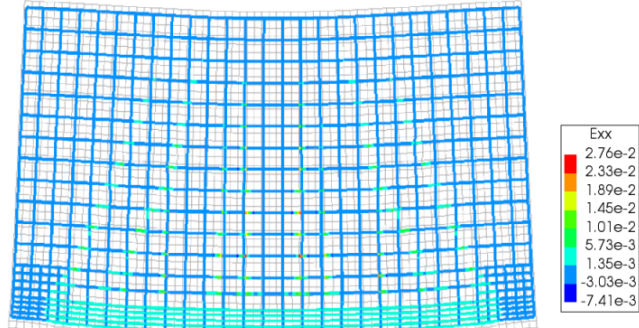


Principal concrete compressive stresses at last load step before failure

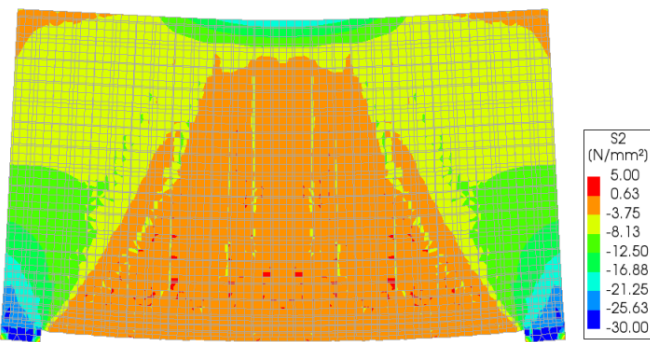
Model E2



Crack pattern

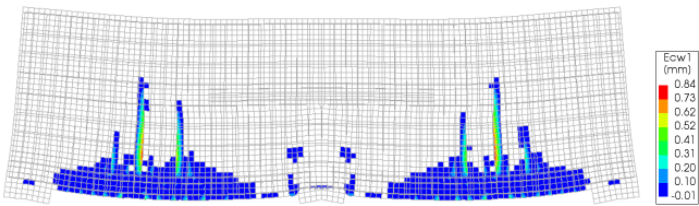


Reinforcement strains at last load step before failure

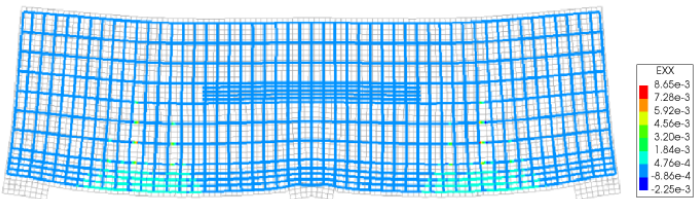


Principal concrete compressive stresses at last load step before failure

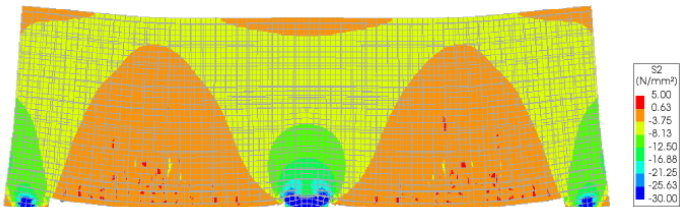
Model F1



Crack pattern

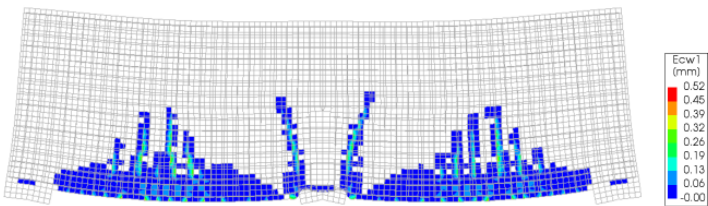


Reinforcement strains at last load step before failure

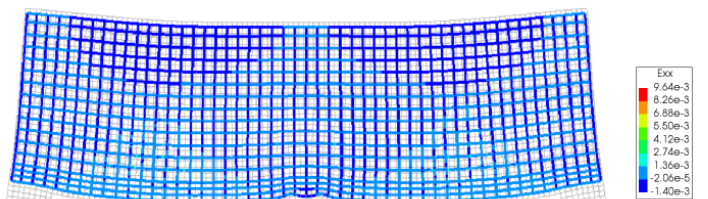


Principal concrete compressive stresses at last load step before failure

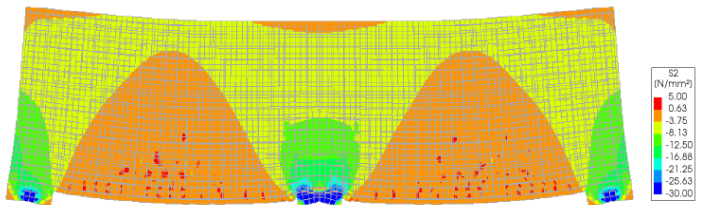
Model F2



Crack pattern



Reinforcement strains at last load step before failure

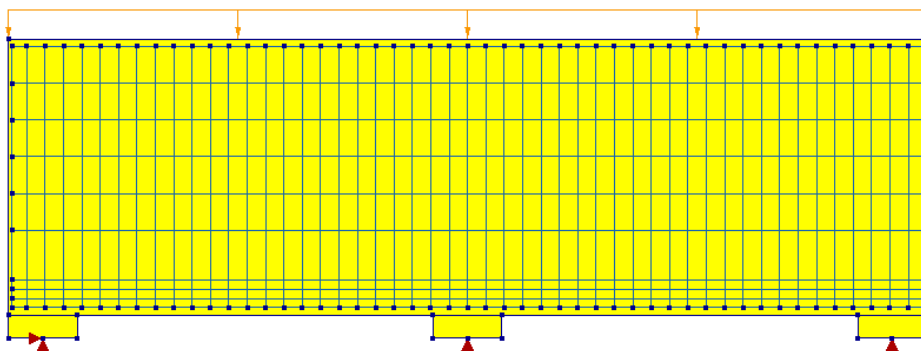
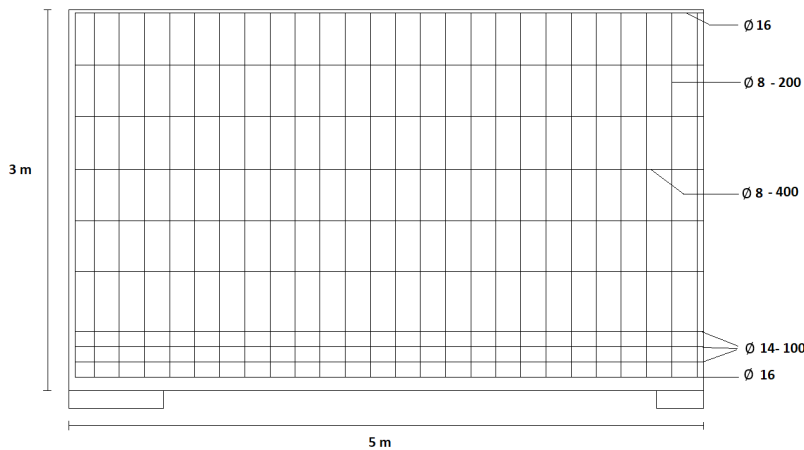


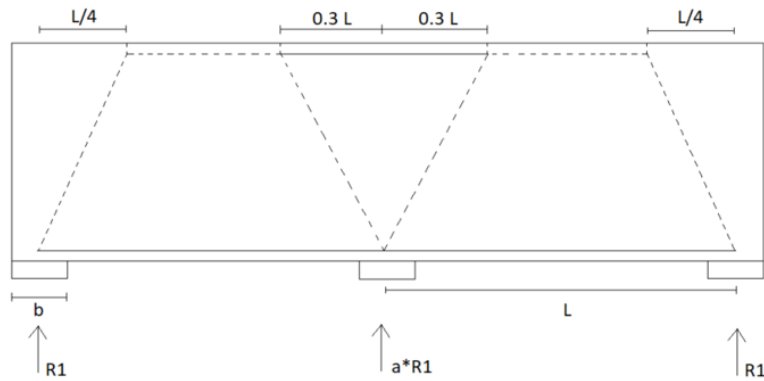
Principal concrete compressive stresses at last load step before failure

Appendix D: Continuous wall girder calculation using new strut-and-tie model

The continuous wall girder reinforcement is designed using the new strut-and-tie model, as proposed in chapter 6.5. The calculation is done in Microsoft Excel, this is presented on page 117. The reinforcement design that resulted from this calculation is presented in the table and the figures below.

New Model			
q (ULS)	565 kN/m	q (SLS)	377 kN/m
n		s	
Bottom reinforcement	3 layers 2 x Ø14 1 layer 2 x Ø16	100 mm	
Vertical web reinforcement	Ø8	200 mm	
Horizontal web reinforcement	Ø8	400 mm	
Top reinforcement	1 layer 2 x Ø16	-	





Staaftermodel			
	Links	Rechts	
h/L	0.649	0.649	
a	2.290	2.290	
Oplegreactie midden	1508	1508	kN
totale oplegreactie tussensteunpunt	3016		kN
Oplegreactie buiten	1317	1317	kN
L/4	1.16	1.16	m
Alfa	67.7	67.7	graden
Beta	63.8	63.8	graden
Kracht in drukdiagonaal naar buitenste steunpunt	1423.80	1423.80	kN
Kracht in drukdiagonaal naar tussensteunpunt	1680.91	1680.91	kN
Kracht in onderwaping	540.72	540.72	kN
Kracht in bovenwaping	202.11	202.11	kN

Hoofdwaping ULS			
As	1325.8	mm ²	
Fs (ULS)	540.7	kN	
sigmas	407.9	MPa	

Scheurwijdte			
Fs (SL)	360.8	kN	
sigmas	272.1	MPa	
kt	0.4		
hc,eff	458.8	mm	
Ac,eff	114688	mm ²	
rho,eff	0.012		
alfaE	6.098		
$\epsilon_{cm} - \epsilon_{cm}$	0.000920		
k1	0.8		
k2	0.5		
k3	3.4		
k4	0.425		
c	58	mm	
equivalente diameter	14.6	mm	
sr,max	411.2	mm	
wk	0.38	mm	

Unity checks	
Knoop boven oplegging links	0.54
Knoop boven oplegging rechts	0.54
Knoop boven tussen steunpunt	0.98
Hoofdwaping ULS	0.94
Scheurwijdte	0.47
Flankwaping horizontaal	0.99
Flankwaping verticaal	0.99
Bovenwaping	0.84

Afmetingen			
Lengte van de wand	10	m	
hoogte	3	m	
Lengte van het tussensteunpunt	750	mm	
Lengte van het linker steunpunt	750	mm	
Lengte van het rechter steunpunt	750	mm	
Wand dikte	250	mm	
Linker overspanning	4.625	m	
Rechter overspanning	4.625	m	
Verschil in steunpuntszetting	0	mm	

Duurzaamheid			
Ontwerplevensduur	50 jaar		
Milieuklasse	XC1		
Constructieve classificatie	S4		
c _{min,dur}	15	mm	
minimale dekking	25	mm	
toegepaste dekking onder	50	mm	
toegepaste dekking boven	45	mm	
toegepaste dekking zijkant	40	mm	
maximale scheurwijdte	0.4	mm	

Wapening									
Aantal lagen onderwaping	4								
Verticale afstand tussen lagen trekbandwapening	100								
Nuttige hoogte	2816.5								
hoogte onderste trekband	365	mm	≤	600	mm				
	Aantal lagen	n	Ø	s	betonstaal	f _{yk}	f _{yd}		
Trekbandwapening onder laag 1	3	2	14	140	B500	500	435		
Trekbandwapening onder laag 2	1	2	16	138	B500	500	435		
Flankwaping verticaal	-	-	8	200	B500	500	435	s	≤ 400
Flankwaping horizontaal	-	-	8	400	B500	500	435	s	≤ 400
Bovenwaping	1	2	16	140	B500	500	435		

Belasting			
	Links	Rechts	
UGT	565	565	kN/m
BGT	377	377	kN/m

Eigenschappen Beton			
Sterkteklasse	C30/37		
f _{ck}	30	MPa	
f _{cd}	20.0	MPa	
f _{ctm}	2.9	MPa	
E _{ctm}	32800	MPa	